# New devices for noise control and acoustic cloaking

VÍCTOR MANUEL GARCÍA CHOANO

EDITORIAL
UNIVERSITAT POLITÈCNICA DE VALÈNCIA


UNIVERSITAT POLITÈCNICA DE VALÈNCIA

Departamento de Ingeniería Electrónica

# New devices for noise control and acoustic cloaking

Por Víctor Manuel García Chocano

---

Dirigida por
José Sánchez-Dehesa Moreno-Cid

September 7, 2015

*Collection Doctoral Thesis*


Telf.: 963 877 012 / www.lalibreria.upv.es

ISBN: 978-84-9048-388-6 (printed version)

Este manuscrito de tesis ha sido valorado y calificado Excelente por el siguiente tribunal de evaluación:

1. Dr. Theodore P. Martin
   Research Physicist
   Acoustics Division
   Naval Research Laboratory - USA

2. Dr. Michael R. Haberman
   Research Scientist
   Applied Research Laboratories
   University of Texas at Austin - USA

3. Dr. Xiaoming Zhou
   Associate professor
   School of Aerospace Engineering
   Beijing Institute of Technology - China

En Valencia, a 8 de Mayo de 2015

Esta tesis ha sido valorada y calificada Cum Laude por el siguiente tribunal de defensa:

1. Dr. Mats Åbom
   Full Professor
   Department of Aeronautical and Vehicle Engineering
   Royal Institute of Technology - Stockholm

2. Dr. Francisco J. Meseguer Rico
   Full Professor
   Instituto de Ciencia de Materiales
   Centro Superior de Investigaciones Científicas - Spain

3. Dr. Antonio Arnau Vives
   Full Professor
   Departamento de Ingeniería Electrónica
   Universidad Politéctica de Valencia - Spain

En Valencia, a 26 de Junio de 2015

I would like to acknowledge the financial support provided by the U.S.A Office of Naval Research under Contracts No. N000141210216 and No. N000141210216.


I also acknowledge the support of the Spanish MICINN under Contract No. TEC2007-67239 and the Spanish MINECO under Contract No. TEC 2010-19751.

# Agradecimientos

En primer lugar agradezco al profesor José Sánchez-Dehesa su dedicación a lo largo de todos estos años. Su experiencia y motivación han sabido conducir mis esfuerzos hacia el presente trabajo. Doy gracias a mis compañeros Alfonso, Rogelio, Ana, Dani, Edgar, Matthew, Weiwei, Paco, Suitberto y Jorge por los buenos momentos que hemos pasado en el laboratorio y también fuera de él. Sin duda su colaboración ha sido un ingrediente fundamental en el desarrollo de este manuscrito. También incluyo a Héctor, antiguo director y desde entonces amigo sin el cual no habría llegado hasta aquí. No me olvido de mi maestro Ezequiel Redondo, que por encima de ser buenos estudiantes nos enseñó a muchos a ser mejores personas.

Agradezco su presencia a todas aquellas personas que me he encontrado durante mi estancia en el Grupo de Fenómenos Ondulatorios. A Tomás por tantas charlas tan largas como interesantes. A Julien por su singular habilidad para combinar buenos momentos en laboratorio y montaña. Y finalmente a Arkadii, Lorenzo y Johan, con quienes he tenido el placer de trabajar y publicar artículos de notable impacto.

Doy gracias a mi padre, incansable ingeniero de quién aprendí el rigor con el que desempeño mi trabajo, y a mi madre, que quizás sin darse cuenta me enseñó a compaginar el rigor con la creatividad. A los dos les debo lo que soy. A Oliver, a quien por suerte la vida puso a mi lado por hermano, y a Marita, sin duda mi cuñada favorita. Extiendo mi gratitud a toda mi familia, con la que he compartido y seguiré compartiendo momentos entrañables.

Agradezco a Rubén, Carlos, Ángel A., Toni, Isra, Héctor y Ángel G., selecto club de ingenieros electrónicos donde los haya, todos estos años llenos de cenas, discusiones y algunos proyectos. Y por supuesto esta sección no puede acabar (bajo pena de golpe de remo) sin hacer mención a mis amigos de toda la vida: Jairo, Adrián, Laura M., Pedro, Andrea, Mª Elena, Edu, Héctor, Marta, Manolo, Cristina, Susana, Laura G., Lourdes, José ángel, Mario, Dani y Olga. Siempre estuvieron allí, y siempre estarán. No me olvido de Vicente y Víctor M. JR, con quienes tantas galaxias de bolicas he compartido en la oscuridad de la montaña. Y también incluyo a Erik, por las innumerables contiendas de nochevieja que hemos pasado y por las que nos quedan.

Gracias a mi ángel, Susi, por darme ánimos, por compartir conmigo momentos tan felices y por apoyarme en los momentos duros. No hay mal que sobreviva una sonrisa suya. También doy gracias a su familia por acogerme y hacerme sentir uno más desde el principio.

A mis padres,
y a Susi.

Resumen de la tesis doctoral

# Nuevos dispositivos para el control de ruido y mantos de invisibilidad acústica

de

**D. Víctor Manuel García Chocano**
Doctor en Ciencias por el Departamento de Ingeniería Electrónica
Universitat Politècnica de València, Valencia, Marzo 2015

El objetivo de este trabajo es el diseño de nuevos dispositivos acústicos basados en disposiciones de centros de dispersión. En primer lugar, el uso de cristales sónicos como barreras acústicas para el control de ruido de tráfico es analizado en detalle. Debido a las limitaciones que presentan las estructuras convencionales basadas en centros de dispersión rígidos, se propone la inclusión de elementos absorbentes en los mismos. Se han considerado dos tipos distintos de absorbente: materiales porosos y placas microperforadas. En el primer caso se analizan las propiedades atenuadoras de barreras formadas por cilindros que contienen granza de caucho. La segunda solución se basa en la construcción de coronas microperforadas. En ambos casos se han desarrollado modelos analíticos que permiten determinar el comportamiento de las barreras. Dichos modelos muestran un acuerdo satisfactorio con las correspondientes realizaciones experimentales. Finalmente se ha realizado un proceso de optimización con objeto de obtener barreras eficientes para la atenuación de ruido de tráfico.

Otra aplicación considerada en este trabajo es el desarrollo de dispositivos de invisibilidad acústica. Concretamente se pretenden diseñar mantos constituidos con elementos rígidos para ondas acústicas en aire. La primera propuesta consiste en un manto que utiliza la temperatura del medio externo para controlar sus propiedades efectivas. Además se han desarrollado mantos en dos y tres dimensiones a través de la técnica de cancelación de la dispersión. Los diseños han sido realizados por medio de un proceso de optimización y su funcionamiento ha sido demostrado experimentalmente.

Resum de la tesi doctoral

# Nous dispositius per al control de soroll i mantells d'invisibilitat acústica

de

**D. Víctor Manuel García Chocano**
Doctor en Ciències pel Departament d'Enginyeria Electrònica
Universitat Politècnica de València, Març 2015

L'objectiu d'aquest treball és el disseny de nous dispositius acústics basats en disposicions de centres de dispersió. En primer lloc, l'ús de vidres sònics com barreres acústiques per al control de soroll de trànsit és analitzat en detall. A causa de les limitacions que presenten les estructures convencionals basades en centres de dispersió rígids, es proposa la inclusió d'elements absorbents en els mateixos. S'han considerat dos tipus diferents de absorbent: materials porosos i plaques microperforades. En el primer cas s'analitzen les propietats atenuadores de barreres formades per cilindres que contenen gransa de cautxú. La segona solució es basa en la construcció de corones microperforades. En tots dos casos s'han desenvolupat models analítics que permeten determinar el comportament de les barreres. Aquests models mostren un acord satisfactori amb les corresponents realitzacions experimentals. Finalment s'ha realitzat un procés d'optimització per tal d'obtenir barreres eficients per l'atenuació de soroll de trànsit.

Una altra aplicació considerada en aquest treball és el desenvolupament de dispositius d'invisibilitat acústica. Concretament es pretenen dissenyar mantells constituts amb elements rígids per ones acústiques en aire. La primera proposta consisteix en un mantell que utilitza la temperatura del medi extern per controlar les seves propietats efectives. A més s'han desenvolupat mantells en dues i tres dimensions a través de la tcnica de cancellació de la dispersió. Els dissenys han estat realitzats per mitjà d'un procés d'optimització i el seu funcionament ha estat demostrat experimentalment.

Abstract of the doctor thesis

# New devices for noise control and acoustic cloaking

by

**D. Víctor Manuel García Chocano**
Doctor of Science in the Ingeniería Electrónica department
Universitat Politècnica de València, Valencia, March 2015

The aim of this work is to design new acoustic devices based on arrangements of scattering units. First, the use of sonic crystals as noise barriers for traffic noise control is comprehensively analyzed. Due to the limitations of the conventional structures based on rigid scatterers, the inclusion of absorbing elements is proposed. Two different types of absorbers are here considered: porous materials and microperforated plates. In the first case, the attenuation characteristics of barriers made with cylinders containing rubber crumb is analyzed. The second proposal is based on the construction of cylindrical microperforated shells. Analytical approaches modelling the behavior of the barriers have been developed in both cases. These models show a satisfactory agreement with the corresponding experimental realizations. Finally, an optimization process is performed in order to obtain efficient sound barriers intended to attenuate traffic noise.

Another application considered in this work is the construction of cloaks to render objects acoustically invisible. In particular, cloaks made with rigid inclusions are designed to operate with airborne sound. The first proposal consists of a cloak that utilizes the temperature of the background to control the properties of the effective medium. In addition, two and three-dimensional cloaks have been developed through the scattering cancellation technique. These devices have been designed by means of an optimization procedure and their performance has been experimentally demonstrated.

# Contents

# List of Figures

# List of Tables

# Part I

# Noise barriers based on rubber crumb cylinders

# Chapter 1

# Introduction

## 1.1 Traffic noise pollution

In the last decades the number of road vehicles increased drastically, in such a manner that traffic noise became a major environmental problem, especially in urban areas or places located near transport infrastructures. Road traffic is considered the main source of noise in industrialized countries, followed by neighbourhood and aircraft noise, and therefore it became an issue of immediate concern to many authorities. The European Union (EU) estimates that about 125 million people could be exposed to levels of road traffic noise above 55 dB $L_{den}$[1] , 37 million of them suffering more than 65 dB $L_{den}$ [Eur14]. These values exceed the limits recommended by the World Health Organization, who reported adverse health effects for exposures to noise levels at night above 40 dB [Wor09]. It is recognized that, apart from obvious annoyance, a continuous exposure to noise results in harmful effects such as sleep disturbance, psychological reactions, hearing loss or cardiovascular problems [Wor11].

In general, a noise problem involves a system of three basic elements: a sound source, a transmission path and a receiver. Source control has provided a considerable reduction in the noise levels emitted by the vehicles, the electric car perhaps being the best example. However this solution only affects urban environments where low velocity profiles make engine noise dominant over aerodynamic and rolling noise. At high velocities, noise generation is

[1] Weighted average during the day, evening and night [MV04].

reduced by improving the vehicle aerodynamics, the tire design and choosing low noise paving materials. Other contributions are given by improvements in the muffler design or the shielding of the noisy components of the engine. Nevertheless the usual way of dealing with traffic noise consists of making changes in the propagation path of the sound. In this context urban planning and the use of noise barriers have proved to be effective solutions.

Noise barriers are basically thought as obstacles that intercepts the line of sight from the source to the receiver. The noise at the receiver is reduced to a small fraction of that generated, which usually arrives via diffraction along the barrier edges or reflections in surrounding buildings. Because of their importance noise barriers have been widely studied, especially since the sixties. A review of the work reported before 1974 was given by Kurze, where the case of simple barriers based on flat screens is analysed [Kur74]. Later, more complex and efficient structures were designed, concluding that geometries such as the T-shaped barrier improves the shielding effectiveness by reducing the diffracted field in the shadow zone [MO80,HCWH91]. Multiple-edge barriers also proved to be good isolators [CHCW95]. A general review of the more recent advances has been performed by Ekici and Bougdah [EB03]. However traditional approaches are not able to find complex structures whose geometry optimizes the barrier efficiency, so in this way some authors proposed the use of optimization algorithms. Duhamel used genetic algorithms in order to optimize the shape of a rigid barrier, showing that T-shaped barriers were far from optimal designs [Duh06]. Baulac et al. also applied genetic algorithms to the search of optimal T-shaped barriers [BDJ08] and genetic algorithms coupled with the Nelder-Mead method for optimal multiple edge barriers [BDJ07].

## 1.2 Rubber crumb as acoustic absorbent

Along with the increase of traffic noise, the growth of the automobile industry has led to new problems among which waste generation is one of the most important. With this regard, used tires are the major and most problematic source of waste due to the large volume produced and their durability. This fact resulted in a massive storage in landfills and the consequent environmental risks. Fortunately, governments became aware of this problem and

significant progress has been made in the last decade. The EU was a pioneer in the organisation of the collection and processing of used tires as a result of legislation and uniform guidelines that apply to all member states. The European Tyre Recycling Association (ETRA) estimated in 2012 that 3.3 million tonnes of used tires are produced annually in the EU countries [Eur13]. Of this amount, almost 40% is intended to energy recovery as alternative fuel in electric power stations and other industries like cement kilns or foundries. Other 40% of the used tires are employed in several applications as recycled material, 10% is retreaded and the remaining part is reused as second hand tires in countries with less restrictive policies or stored in landfills. When recycled, the whole tire is usable in some situations such as coastal protection projects (erosion barriers, artificial reefs and off-coast breakwaters). However, during the recycling process scrap tires are often cut into shreds or chips allowing its use in many other applications. Some of them are rubberized asphalt (safer and quieter than the conventional), protective flooring, sport tracks, footwear or speed humps. The granular form of the crushed tires is known as rubber crumb and, due to its porous nature, acoustic absorption is expected to occur within the material. This represents an alternative to the classical fibrous and foam absorbers, taking advantage of a good absorption combined with good mechanical strength and durability.

Because of this reason, rubber crumb was proposed in the late nineties as sound absorber intended for the construction of cheap and ecological noise barriers [PR99]. The authors reported a theoretical model supported by an experimental characterization where the absorption of several samples made with rubber crumb was determined. As result of these investigations, a Spanish and EU patent concerning noise barriers made with rubber crumb was presented [PSMC95].

## 1.3 Sonic crystals

Sonic Crystals (SC) are structures made of sound scatterers periodically arranged in a lattice [Dow92]. SCs forbid sound propagation for some frequency bands, named bandgaps, in a similar manner as semiconductors forbid the transmission of electronic waves in some energy bands [AM76]. The physical mechanism behind the formation of bandgaps is the same for both scalar

waves, that is, the destructive interference between waves reflected by consecutive planes of sound scatterers (for acoustic waves) or atomic planes (for electronic waves). Transmittance and reflectance measurements for sound waves impinging arrays of solid cylinders in air demonstrated that, at bandgap frequencies, a low transmittance and a high reflectance are simultaneously observed due to Bragg scattering [SPCMS$^+$98, RCSP$^+$99, SCSD$^+$01]. The existence of complete bandgaps as well as the presence of deaf modes in the acoustic bands were demonstrated in the late nineties [SPCMS$^+$98, RCSP$^+$99]. Also, it has been shown that a disordering in the SC lattice produces a bandgap enlargement [CSDR$^+$99].

Numerical algorithms have been developed to reproduce the experimental findings. They are based on different theoretical approaches like plane-wave expansion [Kus97], transfer matrix [SE96], variational methods [SPCMS$^+$98, RCSP$^+$99,CSDR$^+$99], multiple scattering [SCSD$^+$01,CY01,GY03,SHCSD03], finite differences in time domain (FFTD) [SG00] and the finite element method [LHHD95]. As will be shown in the next chapter, the multiple scattering framework has been employed in this work to characterize the properties of different SC structures.

Practical devices like, for example, acoustic filters or waveguides based on SCs have been proposed and demonstrated [MI01, KCBL04]. Taking advantage of the low acoustic impedance of SCs with low filling fractions, it is also possible to implement convergent lenses [CSSP$^+$01] and Fabry-Perot interferometers [SHCSD03]. Optimization processes have also been applied to SCs in order to improve their acoustical properties. Fist works on this topic were reported by Håkansson et al., who applied genetic algorithms to design acoustic lenses [HCSD05] and demultiplexers [HSDC06]. Another application that has received much attention is the noise control through acoustic barriers based on SC.

### 1.3.1 Sonic crystals as noise barriers

Apart from good attenuation properties, noise barriers have more features that should be assessed. Aesthetics aspects or practical issues like the wind resistance are parameters that should not be ignored in the barrier design. Since SCs improve these characteristics while showing a good sound attenu-

ation at bandgap frequencies, they were proposed as an alternative to conventional noise barriers. Sound attenuation up to 20dB [SPCMS+98] and 25dB [SPRMS+02] were obtained with two-dimensional (2D) arrangements of metallic cylinders in air, concluding that SCs can compete with mass law-based sound screens with the advantage of less volume and weight.

It was predicted that sound attenuation (in dB) of a 2D SC increases linearly with the number of rows of the slab [GMV+03], although diffraction effects associated with the finite height of barriers defines a limit to its potential attenuation. Selective noise reduction has also been reported through SC barriers based on three-dimensional (3D) scatterers [BME02]. SC barriers with embedded resonances have been proposed to attenuate efficiently the low frequency region of the audible spectrum (below 500 Hz) [HCY+03]. In addition, optimization processes based on genetic algorithms, have been applied in order to improve the noise attenuation by means of the creation of vacancies in the periodic structure [RGSPGR+09, HGNB+08].

However SC barriers made of rigid cylinders in air show only a strong attenuation of the transmitted sound at bandgap frequencies. For frequencies outside this range, the attenuation of the barrier is poor, making impossible its application for broadband noise profiles. In order to overcome this drawback, a porous covering of the cylinders has been proposed as a solution to get a more uniform attenuation spectrum [UAL06]. Umnova and coworkers reported the insertion loss spectra by barriers made of three rows of cylinders having a thin porous covering. They showed that covering the scatterers with an absorptive layer makes the insertion loss more uniform in frequency and, in addition, increases the overall levels of attenuation.

## 1.4 Objectives

The aim of the first part of this work is to design efficient noise barriers based on SCs for traffic noise control. The appearance of the proposed barriers is shown in Fig. 1.1, where an application example is recreated. In order to extend the attenuation levels and bandwidth of the resulting structures, the inclusion of rubber crumb inside the scattering units is considered. Thus, the attenuation of the barrier is based on the combination of two mechanisms: Bragg reflectance due to the periodicity of the slabs and absorption by the

porous material. It is important to analyse their relative contribution to the total insertion losses. As will be shown, some scenarios require a low level of reflectance because of the multiple reflections of waves occurring between two parallel barriers or the presence of a close reflective element.

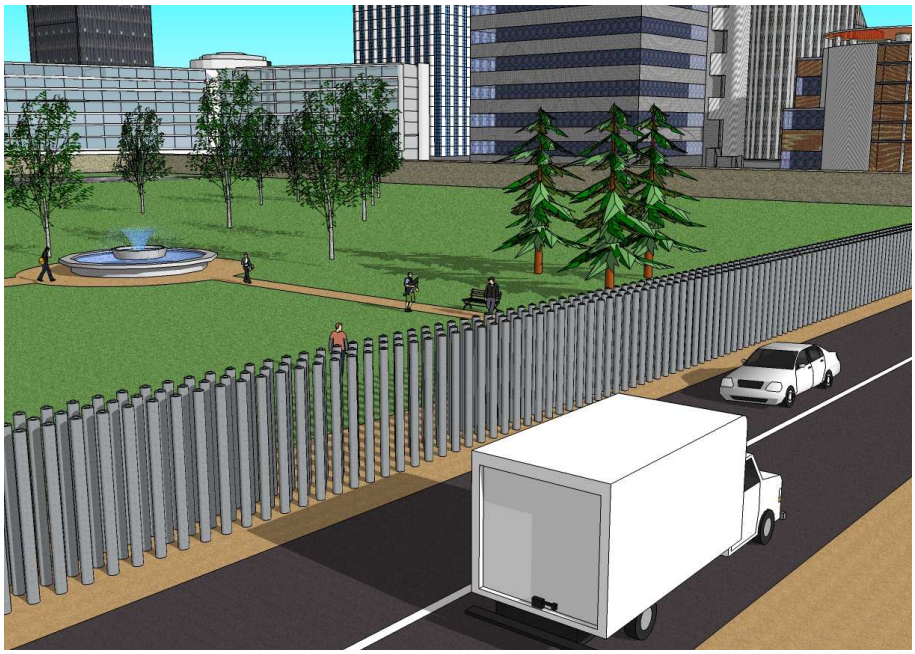

Figure 1.1: Representation of a sound barrier based on a sonic crystal and placed along a road.

It is intended to implement a numerical method to calculate the properties of SCs made with cylinders that contain rubber crumb. With this purpose, the analysis of 2D arrangements of scatterers will be performed through the multiple scattering theory. The use rubber crumb will be introduced in this framework through the study of its effective acoustic properties. Thus, the existing models that regard the porous material as an equivalent fluid will be revised. The resulting theoretical framework will be verified through an experimental characterization and, finally, a design procedure intended to obtain efficient noise barriers for the specific case of traffic noise will be provided.

# Chapter 2

# Multiple scattering theory

The multiple scattering theory is a framework intended to model the field scattered by one or more obstacles when an external wave impinges on them. From now on it will be used to calculate the acoustic properties of sonic crystals. First, a basic introduction to acoustics is given through the deduction of the wave equation. Then, the scattering by a single cylinder is analysed, leading to the concept of T matrix. From these results the case of finite and infinite arrangements of cylinders are modelled.

## 2.1 The acoustic wave equation

Consider a differential volume element of a fluid material as that shown in Fig. 2.1, where each boundary of the element is subjected to a force due to the pressure field $P(x, y, z)$. The resultant force in the $x$ direction is expressed as

$$\begin{aligned} F_x(x, y, z) - F_x(x + \Delta x, y, z) &= \frac{P(x, y, z) - P(x + \Delta x, y, z)}{dx} dxdydz \\ &= -\frac{\partial P(x, y, z)}{\partial x} dV, \end{aligned} \tag{2.1.1}$$

and similar expressions are obtained for the remaining directions. By applying the Newton's second law

$$\Sigma \vec{F} = dm \cdot \vec{a}, \tag{2.1.2}$$

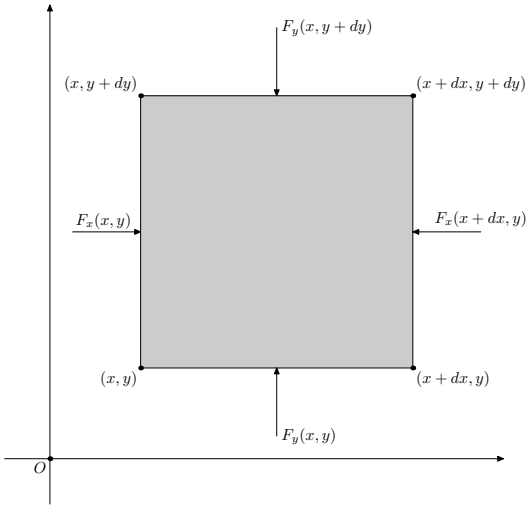


Figure 2.1: Forces acting on a differential element of a fluid. For simplicity it is represented in only two dimensions.

the above equation can be expressed in the vectorial form

$$-\nabla P = \frac{dm}{dV}\vec{a} = \rho\vec{a}, \tag{2.1.3}$$

where $\rho$ is the mass density of the fluid. Note that here the acceleration $\vec{a}$ is not simply the time derivative of the velocity field, but the material derivative

$$\vec{a} = \frac{\partial\vec{v}}{\partial t} + \vec{v}\,(\vec{v}\cdot\nabla)\,, \tag{2.1.4}$$

which takes into account both temporal and spatial variations in $\vec{v}$. Therefore Eq. (2.1.3) takes the form

$$-\nabla P = \rho\left[\frac{\partial\vec{v}}{\partial t} + \vec{v}\,(\vec{v}\cdot\nabla)\right], \tag{2.1.5}$$

which is known as the **equation of motion** and accounts for the conservation of momentum. Assuming small amplitude phenomena, second order terms can be neglected. Hence the non linear term $(\vec{v}\cdot\nabla)\,\vec{v}$ is suppressed, leading to the linearized equation of motion

$$\nabla P + \rho\frac{\partial\vec{v}}{\partial t} = 0. \tag{2.1.6}$$

Another important relation is given by the fact that the total mass of the fluid must remain constant. Thus, the temporal variations of mass in the

differential element must equal the mass flux through the boundaries of such volume:

$$\frac{\partial}{\partial t}\iiint_V \rho dV = -\iint_S \rho\vec{v}\cdot d\vec{S}. \tag{2.1.7}$$

The Gauss' theorem can be applied to the flux term

$$\frac{\partial}{\partial t}\iiint_V \rho dV = -\iiint_V \nabla\cdot(\rho\vec{v})\, dV, \tag{2.1.8}$$

thus leading to the **continuity equation**:

$$\nabla\cdot(\rho\vec{v}) + \frac{\partial\rho}{\partial t} = 0. \tag{2.1.9}$$

The last equation required to fully characterize the acoustic propagation in a fluid is related with the conservation of energy and is derived from thermodynamic principles. When assuming small disturbances of the pressure that compress the medium in an adiabatic and reversible manner, a linear relationship can be found between the pressure fluctuation and the mass density:

$$B = \rho\frac{dP}{d\rho}, \tag{2.1.10}$$

where $B$ is the bulk modulus of the fluid. From this definition it is possible to deduce the **state equation** as

$$\frac{\partial P}{\partial t}dt + d\vec{r}\cdot\nabla P = \frac{B}{\rho}\left(\frac{\partial\rho}{\partial t}dt + d\vec{r}\cdot\nabla\rho\right). \tag{2.1.11}$$

Dividing by $dt$ and inserting the temporal derivative of $\rho$ given by Eq. (2.1.9) we obtain

$$\frac{\partial P}{\partial t} + \vec{v}\cdot\nabla P = \frac{B}{\rho}\left[-\nabla\cdot(\rho\vec{v}) + \vec{v}\cdot\nabla\rho\right]. \tag{2.1.12}$$

Knowing the vectorial identity

$$\nabla\cdot(\rho\vec{v}) = (\nabla\rho)\cdot\vec{v} + \rho\,(\nabla\cdot\vec{v}), \tag{2.1.13}$$

the state equation becomes

$$\frac{\partial P}{\partial t} + \vec{v}\cdot\nabla P = -B\nabla\cdot\vec{v}. \tag{2.1.14}$$

The nonlinear term $\vec{v} \cdot \nabla P$ is neglected, in such a manner that the linearized equation is

$$\frac{\partial P}{\partial t} + B\nabla \cdot \vec{v} = 0. \tag{2.1.15}$$

Once the equations that model the acoustic parameters of a fluid are known, they can be combined in order to deduce the wave equation. Differentiating Eq. (2.1.15) with respect to time and combining the result with Eq. (2.1.6), the following expression is obtained

$$\frac{\partial^2 P}{\partial t^2} - B\nabla \cdot \left(\rho^{-1}\nabla P\right) = 0. \tag{2.1.16}$$

If a harmonic regime is supposed for small and periodic perturbations whose pressure field has the form

$$P\left(\vec{r}, t\right) = \Re\left[P\left(\vec{r}\right) e^{i\omega t}\right], \tag{2.1.17}$$

where $\Re$ denotes real part and $\omega$ is the angular frequency, then Eq. (2.1.16) can be reduced to the Helmholtz wave equation of an inhomogeneous medium

$$\left(\nabla^2 + k^2\right) P = -\rho\nabla\rho^{-1} \cdot \nabla P, \tag{2.1.18}$$

where $k$ represents the wavenumber, defined as

$$k\left(\vec{r}\right) = \omega\sqrt{\frac{\rho\left(\vec{r}\right)}{B\left(\vec{r}\right)}}. \tag{2.1.19}$$

If an isotropic fluid is considered, $B$ and $\rho$ are constant in $\vec{r}$ and therefore the wavenumber becomes constant. Thus Eq. (2.1.18) reduces to the Helmholtz wave equation

$$\nabla^2 P + k^2 P = 0, \tag{2.1.20}$$

where the sound speed of the isotropic fluid is given by

$$c = \frac{\omega}{k} = \sqrt{\frac{B}{\rho}}. \tag{2.1.21}$$

## 2.2 Scattering by a single cylinder

When a wave propagating in a particular medium reaches a region with different acoustical parameters, reflection and refraction effects occur, leading

to the phenomenon known as *scattering*. When a given field impinges on one or more obstacles, a scattered field is generated as a result. The complexity of this field will depend on the incident field, the number and location of the scatterers, their acoustic properties and their geometry. For simplicity the parameters relative to a single scatterer are discussed in this section, while interaction between several scatterers will be treated later.

In this work sound scatterers are assumed to be cylindrical units with circular section. Hence cylindrical coordinates can be adopted to describe the problem, and no effects are expected in the $z$ direction since we suppose infinitely long cylinders. Therefore the scattering problem is reduced to a 2D formulation. When solving the acoustic wave equation in cylindrical coordinates, the solutions are expressed in terms of linear combinations of Bessel and Hankel functions. On the one hand the external field can be expressed as a sum of Bessel functions

$$P^0(r,\theta) = \sum_{q=-\infty}^{+\infty} A_q^0 J_q(kr)\, e^{iq\theta}. \tag{2.2.1}$$

Coefficients $A_q^0$ are usually known since they define the excitation field applied to the scatterer. For the typical case of a plane wave with wavevector $\vec{k_0} = k_{0x}\hat{x} + k_{0y}\hat{y} = k_0(\cos\theta_0, \sin\theta_0)$ and amplitude $C_0$ with the form

$$P^0(\vec{r}) = C_0 e^{i\vec{k_0}\cdot\vec{r}}, \tag{2.2.2}$$

the coefficients are given by

$$A_q^0 = C_0 i^q e^{-iq\theta_0}. \tag{2.2.3}$$

These coefficients can be used to model more general fields provided that they can be expressed as a sum of plane waves. For the case of a Gaussian beam propagating along the $x$-axis, the coefficients describing the field around a scatterer located at cylindrical coordinates $(R_\alpha, \theta_\alpha)$ are [BAOSD03]

$$A_q^0 = k_0 i^q \int_{-\pi/2}^{\pi/2} e^{-Dk_0^2 \sin^2(\theta)} e^{ik_0 R_\alpha \cos(\theta-\theta_\alpha)} e^{-iq\theta} \cos(\theta) d\theta, \tag{2.2.4}$$

where $D$ determines the width of the beam.

On the other hand, the scattered field $P^{SC}$ is expressed in terms of Hankel functions

$$P^{SC}(r,\theta) = \sum_{q=-\infty}^{+\infty} A_q H_q(kr)\, e^{iq\theta}. \tag{2.2.5}$$

The coefficients $A_q$ are determined by the incident field and the physical nature of the scatterer. Assuming a linear regime, a general relation between $A_q$ and $A_q^0$ can be established through a transition matrix $T_{qs}$ according to

$$A_q = \sum_s T_{qs} A_s^0. \tag{2.2.6}$$

The elements of the transition matrix or T-matrix contain all the information about the scatterer. They depend on the acoustic parameters as well as the shape of the scatterer. The expression of the T matrix is obtained by applying boundary conditions at each interface between two different media, either between the external surface of the scatterer and the background fluid or between internal layers within the scatterer.

Three different sound scatterers have been here studied: metallic rods, cylinders made of rubber crumb and cylinders consisting of a shell of rubber crumb and a metallic core. Due to the high acoustic impedance of any metal compared to air, the steel employed in building the rods can be considered as a rigid material with infinite mass density. Regarding the rubber crumb, it is modelled as a fluid-like medium characterized by its porosity, complex dynamic mass density and wave number. The calculation of these parameters will be further detailed in Chapter 3. The expressions for the T matrix of each type of scatterer are deduced in the following sections.

### 2.2.1 Fluid cylinder

Consider a fluidlike cylinder of infinite length, radius $R$, mass density $\rho_a$, sound velocity $c_a$ and porosity $\Omega$. It is embedded in a background with acoustic parameters $\rho_b$ and $c_b$. The general expressions for the incident pres-

sure $P^0$ and the field scattered by the cylinder $P^{SC}$ are

$$P^0(r,\theta) = \sum_{q=-\infty}^{+\infty} A_q^0 J_q(k_b r) e^{iq\theta}, \quad (r > R), \tag{2.2.7}$$

$$P^{SC}(r,\theta) = \sum_{q=-\infty}^{+\infty} A_q H_q(k_b r) e^{iq\theta}, \quad (r > R), \tag{2.2.8}$$

where $k_b = \omega/c_b$ is the wave number outside the cylinder. Therefore the total pressure field outside the cylinder is given by

$$P^{out}(r,\theta) = \sum_{q=-\infty}^{+\infty} \left(A_q^0 J_q(k_b r) e^{iq\theta} + A_q H_q(k_b r) e^{iq\theta}\right), \quad (r > R). \tag{2.2.9}$$

The pressure field transmitted inside the cylinder is

$$P^{in}(r,\theta) = \sum_{q=-\infty}^{+\infty} B_q J_q(k_a r) e^{iq\theta}, \quad (r < R) \tag{2.2.10}$$

where $k_a = \omega/c_a$.

Coefficients $A_q^0$ are defined by the incident field, as previously introduced. Coefficients $A_q$ and $B_q$ depend on $A_q^0$ and the physical parameters of the cylinder. To obtain $A_q$, the boundary conditions at the surface of the cylinder are taken into account. These are the continuity of the pressure field and the normal component of the particle velocity. In the case of a porous material, porosity must be taken into account in the velocity field of the second condition [UAL06]:

$$P^{out}\big|_{r=R} = P^{in}\big|_{r=R}, \tag{2.2.11a}$$

$$\frac{1}{\rho_b} \left.\frac{\partial P^{out}}{\partial r}\right|_{r=R} = \frac{\Omega}{\rho_a(\omega)} \left.\frac{\partial P^{in}}{\partial r}\right|_{r=R}. \tag{2.2.11b}$$

Substituting Eqs. (2.2.9) and (2.2.10) into the above expressions we obtain

$$\sum_{q=-\infty}^{+\infty} \left(A_q^0 J_q(k_b R) e^{iq\theta} + A_q H_q(k_b R) e^{iq\theta}\right) = \sum_{q=-\infty}^{+\infty} B_q^0 J_q(k_a R) e^{iq\theta}, \tag{2.2.12a}$$

$$\frac{k_b}{\rho_b} \sum_{q=-\infty}^{+\infty} \left(A_q^0 J_q'(k_b R) e^{iq\theta} + A_q H_q'(k_b R) e^{iq\theta}\right) = \frac{\Omega k_a}{\rho_a} \sum_{q=-\infty}^{+\infty} B_q J_q'(k_a R) e^{iq\theta}, \tag{2.2.12b}$$

where $J'_q$ and $H'_q$ are the first derivatives of the q-th order Bessel and Hankel functions, respectively. Multiplying both equations by $e^{is\theta}$ and integrating from 0 to $2\pi$ the infinite sums can be obviated. Since only the terms with $s = q$ are nonzero, the above equations become

$$A_q^0 J_q(k_b R)e^{iq\theta} + A_q H_q(k_b R)e^{iq\theta} = B_q^0 J_q(k_a R)e^{iq\theta}, \tag{2.2.13a}$$

$$\frac{k_b}{\rho_b}\big(A_q^0 J_q(k_b R)e^{iq\theta} + A_q H_q(k_b R)e^{iq\theta}\big) = \frac{\Omega k_a}{\rho_a} B_q J_q(k_a R)e^{iq\theta}. \tag{2.2.13b}$$

Since $A_q$ only depends on the coefficient $A_q^0$ of the same order $q$, the T matrix of the scatterer becomes diagonal. After some operations we obtain the diagonal elements of the T matrix used to model the rubber crumb cylinders

$$T_q = \frac{A_q}{A_q^0} = -\frac{\rho_q J'_q(k_b R) - J_q(k_b R)}{\rho_q H'_q(k_b R) - H_q(k_b R)}, \tag{2.2.14}$$

where

$$\rho_q = \frac{1}{\Omega}\frac{\rho_a c_a}{\rho_b c_b}\frac{J_q(k_a R)}{J'_q(k_a R)}. \tag{2.2.15}$$

### 2.2.2 Rigid cylinder

The T matrix of a rigid cylinder can be easily deduced from the case of a fluid cylinder. Since the assumption of rigid material implies $\rho_a = \infty$, the expression (2.2.14) is simplified by taking this limit:

$$T_q = -\frac{J'_q(k_b R)}{H'_q(k_b R)}. \tag{2.2.16}$$

Note that this deduction is similar to the application of Neumann boundary conditions, where normal velocity vanishes at the surface of the cylinder. The expression obtained will be useful in order to model rods made with almost any rigid material, such as metal, wood or plastic.

### 2.2.3 Cylindrical shell

Consider now a cylinder made of a fluid-like porous shell defined by the radii $R_a$ and $R_b$ ($R_a < R_b$) and having parameters $\Omega$, $k_s$, $\rho_s$ and $c_s$. The core ($r < R_a$) is assumed to be a fluid with parameters $\rho_a$ and $c_a$. The cylinder is again embedded in a background with acoustic parameters $\rho_b$ and $c_b$.

The external pressure field outside the cylinder $P^{out}$, inside the shell $P^s$ and inside the core $P^a$ are

$$P^a(r,\theta) = \sum_{q=-\infty}^{+\infty} D_q J_q(k_a r) e^{iq\theta}, \quad (r < R_a), \tag{2.2.17}$$

$$P^s(r,\theta) = \sum_{q=-\infty}^{+\infty} B_q J_q(k_s r) e^{iq\theta} + \sum_{q=-\infty}^{+\infty} C_q H_q(k_s r) e^{iq\theta}, \quad (R_a < r < R_b), \tag{2.2.18}$$

$$P^{out}(r,\theta) = \sum_{q=-\infty}^{+\infty} A_q^0 J_q(k_b r) e^{iq\theta} + \sum_{q=-\infty}^{+\infty} A_q H_q(k_b r) e^{iq\theta}, \quad (r > R_b). \tag{2.2.19}$$

Boundary conditions at the surface $r = R_a$ become

$$B_q J_q(k_s R_a) + C_q H_q(k_s R_a) = D_q^0 J_q(k_a R_a), \tag{2.2.20a}$$

$$\frac{\Omega k_s}{\rho_s}\big(B_q J_q'(k_s R_a) + C_q H_q'(k_s R_a)\big) = \frac{k_a}{\rho_a} D_q J_q'(k_a R_a). \tag{2.2.20b}$$

An intermediate T matrix that relates $B_q$ and $C_q$ can be defined as

$$T_q^s = \frac{C_q}{B_q} = -\frac{J_q(k_s R_a) - \rho_q^s J_q'(k_s R_a)}{H_q(k_s R_a) - \rho_q^s H_q'(k_s R_a)}, \tag{2.2.21}$$

where

$$\rho_q^s = \Omega \frac{\rho_a c_a}{\rho_s c_s} \frac{J_q(k_a R_a)}{J_q'(k_a R_a)}. \tag{2.2.22}$$

Applying now boundary conditions at $r = R_b$ we obtain

$$\begin{aligned} A_q^0 J_q(k_b R_b) + A_q H_q(k_b R_b) &= B_q J_q(k_s R_b) + C_q H_q(k_s R_b) \\ &= B_q \left(J_q(k_s R_b) + T_q^s H_q(k_s R_b)\right), \end{aligned} \tag{2.2.23a}$$

$$\begin{aligned} \frac{k_b}{\rho_b}\big(A_q^0 J_q'(k_b R_b) + A_q H_q'(k_b R_b)\big) &= \frac{\Omega k_s}{\rho_s}\big(B_q J_q'(k_s R_b) + C_q H_q'(k_s R_b)\big) \\ &= \frac{\Omega k_s}{\rho_s} B_q \left(J_q'(k_s R_b) + T_q^s H_q'(k_s R_b)\right). \end{aligned} \tag{2.2.23b}$$

Operating with the above expressions, the T matrix of the whole cylinder is finally given by

$$T_q = -\frac{J_q(k_b R_b) - \rho_q J_q'(k_b R_b)}{H_q(k_b R_b) - \rho_q H_q'(k_b R_b)}, \tag{2.2.24}$$

with

$$\rho_q = \frac{1}{\Omega}\frac{\rho_s c_s}{\rho_b c_b}\frac{J_q(k_s R_b) + T_q^s H_q(k_s R_b)}{J_q'(k_s R_b) + T_q^s H_q'(k_s R_b)}. \tag{2.2.25}$$

These equations are suitable for the calculation of cylinders with a fluid core surrounded by a porous covering. Since in practice the core will be made of steel, the rigid approximation is reasonable. Under this assumption Eqs. (2.2.24) and (2.2.25) do not change, and Eq. (2.2.21) becomes

$$T_q^s = -\frac{J_q'(k_s R_a)}{H_q'(k_s R_a)}. \tag{2.2.26}$$

## 2.3 Arbitrary located scatterers

Consider a cluster of N scatterers arbitrarily located at positions $\vec{R_\alpha}$ with $\alpha = 1, 2, ..., N$. When a external field $P^0$ impinges on the cluster, the scattered field $P^{SC}$ can be expressed as

$$P^{SC}(r,\theta) = \sum_{\alpha=1}^{N}\sum_{q=-\infty}^{+\infty}(A_\alpha)_q H_q(k_b r_\alpha)e^{iq\theta_\alpha}, \tag{2.3.1}$$

where $(r_\alpha, \theta_\alpha)$ are the polar coordinates translated to the center of the $\alpha$-cylinder and $(A_\alpha)_q$ are the coefficients to be calculated.

The total field incident on the $\alpha$-cylinder is

$$P_\alpha^0(r,\theta) = \sum_{s=-\infty}^{+\infty}(B_\alpha)_s J_s(k_b r_\alpha)e^{is\theta_\alpha}. \tag{2.3.2}$$

It takes into account the contribution of the external field $P^0$ as well as the field scattered by the other cylinders. Coefficients $(B_\alpha)_s$ and $(A_\alpha)_q$ are related by

$$(A_\alpha)_q = \sum_{s=-\infty}^{+\infty}(T_\alpha)_{qs}(B_\alpha)_s, \tag{2.3.3}$$

$T_\alpha$ being the T matrix of the $\alpha$th cylinder.

The total field incident on the $\alpha$-cylinder is given by the sum of the external field and the field scattered by all the scatterers except itself. Thus, the Graft's addition theorem can be used to translate the scattered field to

the reference of this cylinder, leading to

$$P_\alpha^0(r,\theta) = \sum_q (A_\alpha^0)_q J_q(k_b r_\alpha) e^{iq\theta_\alpha} + \sum_{\beta\neq\alpha}\sum_s (A_\beta)_s H_{q-s}(k_b R_{\alpha\beta}) e^{i(s-q)\Phi_{\alpha\beta}} J_q(k_b r_\alpha) e^{iq\theta_\alpha}. \quad (2.3.4)$$

The geometric parameters employed here are detailed in Fig. 2.2. Co-

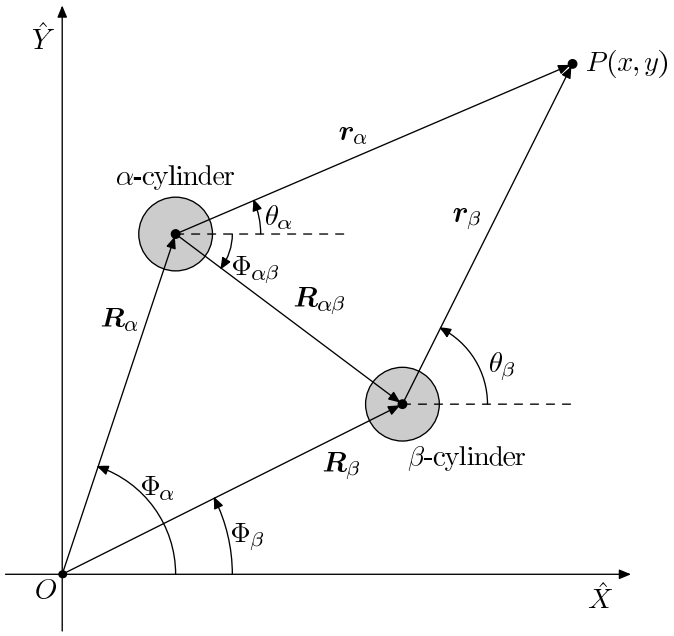


Figure 2.2: Coordinate system and geometric parameters considered in the derivation of the field scattered by an arbitrary arrangement of cylinders.

efficients $(A_\alpha^0)_q$ are the same as $A_q^0$ but translated to the position of the $\alpha$-cylinder. If we suppose the same plane wave as that expressed in Eq. (2.2.2), then

$$(A_\alpha^0)_q = C_0 i^q e^{-iq\theta_0} e^{i\vec{k_0}\cdot\vec{R_\alpha}}. \quad (2.3.5)$$

Coefficients $(B_\alpha)_s$ and $(A_\alpha)_q$ can be related by combining Eqs. (2.3.4) and (2.3.2):

$$(B_\alpha)_q = (A_\alpha^0)_q + \sum_{\beta\neq\alpha}\sum_s (A_\beta)_s H_{q-s}(k_b R_{\alpha\beta}) e^{i(s-q)\Phi_{\alpha\beta}}, \quad (2.3.6)$$

and taking into account Eq. (2.3.3) we get

$$(A_\alpha)_r - \sum_s \sum_\beta (G_{\alpha\beta})_{rs}(A_\beta)_s = \sum_q (T_\alpha)_{rq}(A^0_\alpha)_q, \tag{2.3.7}$$

where

$$(G_{\alpha\beta})_{rs} = \sum_q (1-\delta_{\alpha\beta})(T_\alpha)_{rq} H_{q-s}(k_b R_{\alpha\beta}) e^{i(s-q)\Phi_{\alpha\beta}}. \tag{2.3.8}$$

By truncating the infinite sums of these expressions, they result in a linear system of equations whose coefficients $(A_\alpha)_q$ are finally obtained as

$$(A_\alpha)_q = \sum_{\beta=1}^{N} \sum_{r=-S_{max}}^{+S_{max}} \sum_{s=-S_{max}}^{+S_{max}} (M^{-1}_{\alpha\beta})_{qr}(T_\beta)_{rs}(A^0_\beta)_s, \tag{2.3.9}$$

with

$$(M_{\alpha\beta})_{rs} = \delta_{rs}\delta_{\alpha\beta} - (G_{\alpha\beta})_{rs}. \tag{2.3.10}$$

Once $(A_\alpha)_q$ is known, the total pressure at any point is calculated by adding the external field $P^0$ to the scattered field $P^{SC}$ which is obtained through Eq. (2.3.1). Note that this method allows dealing with cylinders having different acoustic parameters and being located at arbitrary positions.

## 2.4 Periodic arrays of scatterers

The analysis of infinite arrays of scatterers is interesting since it leads to the calculation of the reflectance and transmittance of a periodic slab. In addition it is a useful approach to obtain the pressure field for a large structure at points close to its center where diffraction by the edges is negligible. Consider a slab with $\ell$ rows, each row consisting of a linear and infinite distribution of cylinders. The cylinders of each row are identical and they are separated by a distance $a$, also known as lattice constant. If the central cylinder of the $\ell$th row is located at $\vec{R}_\ell$, then the position of each cylinder in that row is given by (see Fig. 2.3)

$$\vec{R}_\alpha = \vec{R}_\ell + \vec{R}^\ell_\alpha = x_\ell \hat{x} + (y_\ell + \alpha a)\hat{y}. \tag{2.4.1}$$

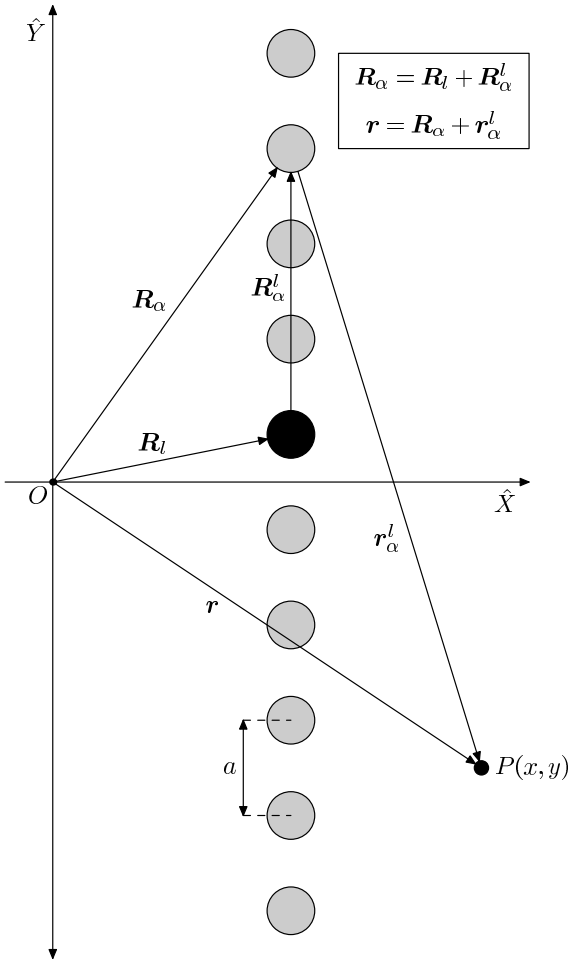


Figure 2.3: Coordinate system and geometry of an infinite line of scatterers.

According to the previous section, the scattered field can be expressed as a linear combination of Hankel functions, which in this case has the form

$$P^{SC}(r,\theta) = \sum_q \sum_\alpha \sum_\ell (A_\alpha^\ell)_q H_q(k_b r_\alpha^\ell) e^{iq\theta_\alpha^\ell}. \tag{2.4.2}$$

The superscript $\ell$ indicates the row number, in such a manner that coefficients $(A_\alpha^\ell)_q$ correspond to the $\alpha$-cylinder of the $\ell$-row. By analogy with the previous section, a relation similar to Eq. (2.3.7) can be derived:

$$(A_\alpha^\ell)_r - \sum_s \sum_m \sum_\beta (G_{\alpha\beta}^{\ell m})_{rs} (A_\beta^m)_s = \sum_s (T_\ell)_{rs} (A_\alpha^{0,\ell})_s. \tag{2.4.3}$$

If the plane wave of Eq. (2.2.2) (with $C_0$ =1) is considered as external

excitation field, then

$$(A_\alpha^{0,\ell})_s = i^s e^{-is\theta_0} e^{i\vec{k_0}\cdot\vec{R_\alpha}} = i^s e^{-is\theta_0} e^{i\vec{k_0}\cdot\vec{R_\ell}} e^{i\vec{k_0}\cdot\vec{R_\alpha^\ell}}. \tag{2.4.4}$$

The application of this field simplifies the problem because the coefficients of the same row vary only in a phase factor with respect to the central cylinder. By defining

$$(A_\ell)_r = e^{-i\alpha ka\sin\theta_0}(A_\alpha^\ell)_r, \tag{2.4.5}$$

it is easy to reduce Eq. (2.4.3) to

$$(A_\ell)_r - \sum_s \sum_m (G_{\ell m})_{rs}(A_m)_s = \sum_s (T_\ell)_{rs} i^s e^{-is\theta_0} e^{i\vec{k_0}\cdot\vec{R_\ell}}, \tag{2.4.6}$$

where

$$(G_{\ell m})_{rs} = \sum_{\beta=-\infty}^{+\infty} (G_{0\beta}^{\ell m})_{rs} e^{i\beta ka\sin\theta_0}. \tag{2.4.7}$$

It is shown that only the coefficients of the central cylinders need to be calculated in each row. Due to the similarity between Eqs. (2.4.6) and (2.3.7) it is concluded that the coefficients $(A_\ell)_r$ can be obtained by solving a linear system of equations like that shown in Eq. (2.3.9).

The scattered field can now be expressed as

$$P^{SC}(r,\theta) = \sum_q \sum_\alpha \sum_\ell (A_\ell) H_q(k_b r_\alpha^\ell) e^{iq\theta_\alpha^\ell} e^{i\alpha ka\sin\theta_0}. \tag{2.4.8}$$

It can be shown that

$$\sum_{\alpha=-\infty}^{+\infty} e^{i\alpha ka\sin\theta_0} H_q(k_b r_\alpha^\ell) e^{iq\theta_\alpha^\ell} = \sum_{\nu=-\infty}^{+\infty} C_{\nu q}^{\pm} e^{i\vec{k}_\nu^{\pm}\cdot(\vec{r}-\vec{R_\ell})}, \tag{2.4.9}$$

where

$$C_{\nu q}^{\pm} = \frac{2i^{-q}}{k_b a}\frac{e^{iq\theta_\nu}}{|\cos\theta_\nu|}, \tag{2.4.10}$$

$$\vec{k}_\nu^{\pm} = k_b(\cos\theta_\nu \hat{x} + \sin\theta_\nu \hat{y}). \tag{2.4.11}$$

The parameter $\theta_\nu$ is defined by the relations

$$\sin\theta_\nu = \sin\theta_0 + \frac{2\pi\nu}{k_b a}, \quad \nu = 0, \pm1, \pm2, ..., \tag{2.4.12a}$$

$$\cos\theta_\nu = \pm\sqrt{1-\sin^2\theta_\nu}, \tag{2.4.12b}$$

and the sign $\pm$ corresponds to the sign of $(x - x_\ell)$. Taking these formulas into account, the scattered field is

$$P^{SC}(r,\theta) = \sum_q \sum_\ell \sum_\nu (A_\ell)_q C^{\pm}_{\nu q} e^{i\vec{k}^{\pm}_\nu \cdot (\vec{r} - \vec{R}_\ell)}, \tag{2.4.13}$$

which can be cast in the form

$$P^{SC}(r,\theta) = \sum_{\nu=-\infty}^{+\infty} C^{\pm}_\nu e^{i\vec{k}^{\pm}_\nu \cdot \vec{r}}, \tag{2.4.14}$$

where

$$C^{\pm}_\nu = \sum_q \sum_\ell (A_\ell)_q C^{\pm}_{\nu q} e^{-i\vec{k}^{\pm}_\nu \cdot \vec{R}_\ell}. \tag{2.4.15}$$

Equation (2.4.14) is an important result that expresses the scattered field as a sum of plane waves with wave vectors $\vec{k}^{\pm}_\nu$. Depending on the real or complex value of $\cos\theta_\nu$, each $\nu$-mode can be propagating or evanescent. Only propagating modes transport energy and $\theta_\nu$ defines the angle of the propagating direction. Regarding Eq. (2.4.12a) it is shown that only the fundamental mode $\nu = 0$ propagates in the low frequency limit, while more modes appear as frequency increases. The frequency where the first mode with $\nu \neq 0$ begins to propagate is known as *diffraction limit*. As will be shown in Chapter 4, this concept is fundamental from an experimental point of view.

The total pressure field, taking into account the incident wave, is

$$P(r,\theta) = e^{i\vec{k_0}\cdot\vec{r}} + \sum_{\nu=-\infty}^{+\infty} C^{\pm}_\nu e^{i\vec{k}^{\pm}_\nu \cdot \vec{r}}. \tag{2.4.16}$$

In order to obtain the reflectance and transmittance of the slab, the energy flux in a unitary cell must be calculated. This is performed by integrating the acoustic intensity $\vec{I}$ in the vertical segment $(y_0, y_0 + a)$. Thus,

$$\Phi = \int_{y_0}^{y_0+a} I_x dy, \tag{2.4.17}$$

where

$$\vec{I} = \frac{1}{2}\Re(P\vec{v^*}) = \frac{1}{2\omega\rho_b}\Re(iP\nabla P^*). \tag{2.4.18}$$

The symbol $\Re$ denotes the real part and $*$ the complex conjugate. By applying Eq. (2.4.16) to these formulas and after some operations we obtain

$$\Phi = \frac{k_b a}{2\omega\rho_b}\left[\cos\theta_0 + \Re(C_0^{\pm} \pm C_0^{*\pm})\cos\theta_0 \pm \sum_{\cos\theta_\nu\in\Re} |\cos\theta_\nu|\left|C_\nu^{\pm}\right|^2\right]. \quad (2.4.19)$$

The first term of this sum corresponds to the incident flow:

$$\Phi_0 = \frac{k_b a\cos\theta_0}{2\omega\rho_b}. \quad (2.4.20)$$

By dividing the total flow $\Phi$ by the incident $\Phi_0$ on the left hand side of the SC we have

$$\frac{\Phi^-}{\Phi_0} = 1 - \sum_{\cos\theta_\nu\in\Re} \frac{|\cos\theta_\nu|}{\cos\theta_0}|C_\nu^-|^2, \quad (2.4.21)$$

where the reflectance can be identified as

$$\mathcal{R} = \sum_{\cos\theta_\nu\in\Re} \frac{|\cos\theta_\nu|}{\cos\theta_0}|C_\nu^-|^2. \quad (2.4.22)$$

Performing the same process in the right hand side we obtain

$$\frac{\Phi^+}{\Phi_0} = 1 + 2\Re|C_0^+| + \sum_{\cos\theta_\nu\in\Re} \frac{|\cos\theta_\nu|}{\cos\theta_0}|C_\nu^+|^2, \quad (2.4.23)$$

being this term equal to the transmittance, i.e.,

$$\mathcal{T} = 1 + 2\Re|C_0^+| + \sum_{\cos\theta_\nu\in\Re} \frac{|\cos\theta_\nu|}{\cos\theta_0}|C_\nu^+|^2. \quad (2.4.24)$$

# Chapter 3

# Rubber crumb modelling

In this chapter the propagation of acoustic waves in porous media is studied. The aim is to provide a model for the calculation of the effective parameters of rubber crumb. These parameters are required to compute the T matrix derived in the previous chapter for cylinders made with this material. First, a brief review of the existing models is introduced. Then, the specific model employed in this work is detailed. Finally, the properties characterizing the rubber crumb used in the experiments are determined.

## 3.1 Introduction

Wave propagation in porous materials is a topic which has received a great deal of attention, especially in the second half of the 20th century. Many of the works reported in this period are related to geophysics, where soil characterization or mineral prospecting were fields that arouse great interest. The sound propagation in porous materials was first developed in those works. Several approaches to the problem were proposed, they being roughly classified in empirical and theoretical models. In addition, theoretical models are usually divided into microstructural and phenomenological models, depending on the degree of detail with which the internal open-cell structure of the material is studied. Most of these models assume that a porous medium behaves as a homogeneous and isotropic fluid where sound absorption occurs primarily due to viscous losses and thermoelastic damping.

### 3.1.1 Empirical models

The best known empirical model used for the prediction of the behaviour of porous materials was proposed by Delany and Bazley [DB70]. By performing measurements on fibrous materials, they deduced empirical laws relating the acoustic properties of the material with its flow resistivity. The flow resistivity is defined as the pressure required for generating a given flow through the material per unit thickness. Due to its simplicity and relative accuracy, these laws were used in many applications until the appearance of more sophisticated models. However, the expressions are limited to a reduced range of frequencies and flow resistivities. Since they do not take into account the structure of the material, the model is only suitable for fibrous materials similar to those measured by the authors. Similar laws were proposed to extend the approach for porous materials [Mik90]. In any case these models have no theoretical basis and their use is reduced due to the development of more accurate and general approaches.

### 3.1.2 Phenomenological models

Phenomenological models consider the porous material from a macroscopic point of view, regardless its internal structure. Since it is supposed that the material is a compressible fluid, the acoustic equations of state, continuity and motion for this kind of media are applied. Some modifications are set in order to take into account the presence of solid particles immersed in the background fluid. The most representative phenomenological model was given by Morse and Ingard [MI68]. This model assumes a material composed of rigid, motionless and incompressible solid particles that form pores interconnected in a random but isotropic way. The classical acoustic equations are modified by several factors related with the macroscopic properties of the medium. These parameters are the porosity, defined as the fraction of fluid filling the pores with respect to the total volume, the effective resistivity which considers viscous effects and the effective stiffness of air which is associated with thermal effects. Finally a structure factor is introduced to distinguish between mass density and inertial mass density, taking into account the increased inertia because of the friction at the pore walls and the deviation of the air motion from the driving force due to the microstruc-

ture. It is noticeable that the last three parameters are frequency dependent and they cannot be determined by physical and mechanical procedures but only through acoustic measurements. This fact complicates the practical application of these models.

### 3.1.3 Microstructural models

The microstructural approach is based on the detailed description of the sound field inside a single cell with a simple geometry. Exact solutions for propagation in pores with constant and usually circular cross-section are calculated and more complex geometries are then modelled from this theory by tuning some adjustment parameters. Microstructural models present more complicated expressions with respect to other approaches and require the specification of three to five parameters, although in some cases none of them are required to be frequency dependent. It has been shown that microstructural predictions are quite accurate for a broad range of frequencies and material types.

The first microstructural model were originally developed by Kirchhoff [Kir68] and Rayleigh [Ray45], who studied a material based on parallel and cylindrical pores oriented in the wave direction. The solid part of the material, also called skeleton, was supposed to be rigid. This assumption is generally valid in conventional acoustic applications where pores are filled with air, leading to the term of rigid frame models. Later, Zwikker and Kosten [ZK49] introduced a simpler and approximate treatment of these theories and extends them to take into account changes in the orientation of the pores and variations of their cross section. The effects of viscosity and thermal conductivity are analyzed separately in terms of the complex density and bulk modulus, respectively. The material is characterized by its porosity and flow resistivity, which are obtained through non acoustical means. Also a structure factor is required, although it can only be determined by comparing acoustic measurements with theoretical data.

In 1983 Attenborough developed a model that describes the acoustic characteristics of rigid fibrous absorbents as well as granular materials [Att83]. It is based on the analysis of the pore structure rather than the particles in the solid frame and is a synthesis of the previous works of Rayleigh [Ray45],

Zwikker and Kosten [ZK49] and other authors [KJ57, SG72]. Starting from the theory of Zwikker and Kosten, Attenborough first studied the sound propagation in a single cylindrical or slit shaped pore. Then he derived expressions for the dynamic mass density and compressibility of an extended bulk medium. The model is based on five parameters: Porosity, flow resistivity, tortuosity, steady flow shape factor and dynamic shape factor. The tortuosity is a parameter that accounts the changing pore orientation and is related to the structure factor given by Zwikker and Kosten. This parameter, along with the flow resistivity and the porosity, is independently obtainable through simple experimental procedures. However the two remaining shape factors must be measured through acoustic means when complex geometries are considered. Moreover, both factors show significant frequency dependence, hence being an important drawback of the Attenborough's theory.

Biot proposed a theory of wave propagation in poroelastic materials [Bio56a, Bio56b]. By assuming a porous elastic solid saturated by a viscous fluid, the averaged motions of both elements are accounted for separately and both frames are then coupled by considering elastic and inertial effects between the two interpenetrating media. This represents a very general and complete theory, although expressions derived are quite complex compared to less general approaches. Allard revised the Biot's theory and made simplifications for the case in which the skeleton motion is negligible, thus creating a rigid frame theory known as the Biot-Allard model [ADN$^+$90]. It uses the expression of mass density given by Biot and the bulk modulus from the Zwikker and Kosten theory. Again tortuosity, flow resistivity and porosity need to be specified, as well as a frequency dependent shape factor.

Stinson and Champoux also contributed significantly to the study of acoustic propagation in porous media. In 1992 they reported a study where materials containing air-filled pores with uniform cross section were studied [SC92]. They obtained exact expressions for pores with circular, rectangular and triangular shape, supporting its theory with experimental measures. They also reported an expression that relates the complex compressibility and the dynamic mass density. In addition, by revising the existing theories, Stinson and Champoux proposed a model with a single frequency independent shape factor. However this approach was only valid for uniform cross sectional pores. In the same year they published another work reporting

measures of a sample with large variations in the cross sectional area of the pores [CS92]. Attenborough and Biot-Allard models proved to be unable to describe the acoustical properties of such sample. Therefore it was proposed a revised theory that treats each pore as a series of uniform tube sections of arbitrary shape and area, showing a good agreement with the experimental data. Nevertheless this approach was impractical since the detailed geometry of the real pores must be known. Faced with this problem, Champoux and Stinson proposed in the same work a generalized model. The resulting theory was similar to the Biot-Allard model although employs two shape factors in order to describe separately the dynamic mass density and bulk modulus.

The application of these theories to the specific case of rubber crumb was reported by Pfretzschner and Rodríguez, who considered a microstructural approach [PR99]. They made use of the Biot-Allard model where some simplifications based on the proposal of Johnson were assumed [JKD87]. The approach requires the knowledge of five parameters, two of them being frequency-independent shape factors that are determined through acoustic measurements. The other parameters, flow resistivity, porosity and tortuosity, were characterized through different procedures in order to provide appropriate inputs to the model. Measurements of the sound absorption of several samples with different grain sizes were reported, showing a good agreement between experiments and theory.

## 3.2 Acoustic model of rubber crumb

The multiple scattering formulation presented in the last chapter requires that rubber crumb be treated as an isotropic fluid. The parameters defining this effective fluid are the dynamic mass density $\rho(\omega)$ and the bulk modulus $B(\omega)$. The expressions employed to calculate them will be provided in the next sections. From these parameters, the complex wave number $k_c$ and the characteristic impedance $Z_c$ can be obtained through the expressions:

$$k_c(\omega) = \omega\sqrt{\frac{\rho(\omega)}{B(\omega)}}, \tag{3.2.1}$$

$$Z_c(\omega) = \frac{1}{\Omega}\sqrt{\rho(\omega)B(\omega)}, \tag{3.2.2}$$

where $\Omega$ is the porosity.

### 3.2.1 Dynamic mass density

When waves propagate inside the pores, the viscous friction between the moving air and the solid skeleton results in energy losses. As Zwikker and Kosten shown, these viscous losses are modelled through the complex dynamic mass density. The Biot-Allard model proposes a dynamic mass density with the form [AA93]

$$\rho(\omega) = \rho_0\tau - i\frac{\sigma\Omega}{\omega}F(\lambda), \tag{3.2.3}$$

where $\rho_0$ represents the density of the fluid that fills the pores, $\tau$ the tortuosity, $\sigma$ the flow resistivity and $\Omega$ the porosity. $F(\lambda)$ is a complex function given by

$$F(\lambda) = -\frac{1}{4}\frac{\lambda\sqrt{-i}T(\lambda\sqrt{-i})}{1-2\frac{T(\lambda\sqrt{-i})}{\lambda\sqrt{-i}}}, \tag{3.2.4}$$

where

$$\lambda = s\sqrt{\frac{8\tau\rho_0\omega}{\sigma\Omega}}, \tag{3.2.5}$$

$$T(x) = \frac{J_1(x)}{J_0(x)}, \tag{3.2.6}$$

and $s$ is a shape factor. Johnson and co-workers reported an accurate simplification of $F(\lambda)$ and reduced the above expression to [JKD87]

$$\rho(\omega) = \rho_0\tau\left[1 + \frac{\sigma\Omega}{i\omega\rho_0\tau}G(\omega)\right], \tag{3.2.7}$$

with

$$G(\omega) = \left[1 + i\frac{4\tau^2\eta\rho_0\omega}{\sigma^2\Lambda^2\Omega^2}\right], \tag{3.2.8}$$

$\eta$ being the viscosity of the fluid. The parameter $\Lambda$ is known as characteristic length, and was defined as

$$\Lambda = \frac{2\int_V |v(r)|^2 dV}{\int_A |v(r)|^2 dA}. \tag{3.2.9}$$

This expression accounts for the ratio between the integral of the microscopic fluid velocity over the volume of the pores and the same integral over the surface of the walls. The characteristic length does not depend on the fluid characteristics, but only on the geometry of the pores. It is a parameter

easily obtained in simple pore geometries. For more complex shapes, it was demonstrated that the characteristic length can be calculated as [JKD87]

$$\Lambda = \frac{1}{\beta_1}\sqrt{\frac{8\eta\tau}{\sigma\Omega}}, \tag{3.2.10}$$

where $\beta_1$ is a shape factor that can only be determined through acoustic experiments. By replacing this expression in Eq. (3.2.7) we finally obtain

$$\rho(\omega) = \rho_0\tau\left[1 + \frac{A}{i}\left(1 + i\frac{\beta_1^2}{2A}\right)^{\frac{1}{2}}\right], \tag{3.2.11}$$

with

$$A = \frac{\sigma\Omega}{\omega\rho_0\tau}. \tag{3.2.12}$$

### 3.2.2 Bulk modulus

Apart from viscous effects, thermal processes inside the pores also lead to acoustic energy losses. These are due to the thermal conduction that takes place between fluid compressions and depressions as a consequence of their different temperature profiles. According to the theory of Zwikker and Kosten, this effect is taken into account through the complex bulk modulus $B(\omega)$. These authors deduced the following expression [ZK49]:

$$B(\omega) = \frac{\gamma P_0}{1 + \frac{2(\gamma-1)}{\sqrt{N_{Pr}}\lambda\sqrt{-i}}T\left(\sqrt{N_{Pr}}\lambda\sqrt{-i}\right)}, \tag{3.2.13}$$

where $\lambda$ and $T(x)$ are defined in Eqs. (3.2.5) and (3.2.6), respectively, $P_0$ is the equilibrium pressure, $N_{Pr} = 0.706$ is the Prandtl number of the saturating fluid (air in this case) and $\gamma = 1.4$ its ratio of specific heats.

Stinson [SC92] found an expression that relates the bulk modulus with the mass density

$$B(\omega) = \frac{\gamma P_0}{\gamma - \frac{\gamma-1}{F(N_{Pr}\omega))}}, \tag{3.2.14}$$

where

$$F(N_{Pr}\omega) = \frac{\rho(N_{Pr}\omega)}{\tau\rho_0}. \tag{3.2.15}$$

By applying this formula to the mass density found by Johnson, Allard and Champoux deduced the general expression [AC92]

$$B(\omega) = \frac{\gamma P_0}{\gamma - \frac{\gamma - 1}{1 + \frac{\sigma' \Omega}{i\tau\rho_0 N_{Pr}\omega}\sqrt{1 + \frac{4i\tau^2\eta\rho_0\omega N_{Pr}}{\sigma'^2\Lambda'^2\Omega^2}}}}, \tag{3.2.16}$$

where, according to the conclusions of Champoux and Stinson, an independent parameter to that used in the description of the dynamic mass density must be employed. Therefore $\Lambda$ is replaced by $\Lambda'$, which is defined as

$$\Lambda' = \frac{2\int_V dV}{\int_A dA}. \tag{3.2.17}$$

This expression is similar to Eq. (3.2.9), but now the volume and area elements are no weighted by the microscopic velocity of the particles of the fluid. It is possible to obtain a simpler formula in order to calculate this parameter

$$\Lambda' = \frac{1}{\beta_2}\sqrt{\frac{8\eta\tau}{\sigma\Omega}}, \tag{3.2.18}$$

where $\sigma' = \beta_2^2\sigma$. $\beta_2$ is a parameter that, like $\beta_1$, needs to be experimentally determined.

By replacing the above expressions the bulk modulus is finally calculated as

$$B(\omega) = \frac{\gamma P_0}{\gamma - \frac{\gamma - 1}{1 - \frac{i\beta_2^2 A}{N_{Pr}}\sqrt{1 + \frac{iN_{Pr}}{2A\beta_2^2}}}}, \tag{3.2.19}$$

where $A$ is the factor defined by Eq. (3.2.12).

## 3.3 Parameters of rubber crumb

The model has five parameters: Flow resistivity $\sigma$, tortuosity $\tau$, porosity $\Omega$ and the two shape factors $\beta_1$ and $\beta_2$. The first three parameters can be experimentally determined through non-acoustical methods, while the shape factors are obtained by fitting the model to experimental data obtained from acoustic measurements. The rubber crumb used in this work is classified as polydisperse and consists of grains with sizes in the range from 0 to 3 mm. The five parameters have been measured in the Instituto de Acústica (CSIC) in Madrid by procedures which are briefly explained in the next sections.

### 3.3.1 Flow resistivity

The flow resistivity is an important parameter that characterizes a porous material. Some basic models, like that reported by Delany and Bazley, only need this input in order to completely characterize the material. The flow resistivity is defined as the specific flow resistance per unit thickness

$$\sigma = \frac{\Delta P}{vd}, \tag{3.3.1}$$

where $d$ is the thickness of the measured sample, $\Delta P$ is the pressure drop across it and $v$ is the flow velocity that crosses the material. The measurement of flow resistivity is performed by following the European Norm EN29053:1993 [EN 94]. A steady air flow is generated by a compressor. It is measured with a flowmeter and led to the sample. The pressure drop is measured with a differential manometer, in such a manner that Eq. (3.3.1) can be computed. The value obtained for our rubber crumb is $\sigma = 3318.6$ N.s/m$^4$.

### 3.3.2 Tortuosity

The tortuosity is related with the structure of the skeleton. It takes into account the shape and orientation of the pores, as well as the interconnection between them. The experimental determination of the tortuosity is based on the procedure developed by Brown [Bro80]. According to this author, the tortuosity can be obtained as

$$\tau = \Omega \frac{\rho_p}{\rho_f}, \tag{3.3.2}$$

where $\rho_f$ is the electrical resistivity of a given conducting fluid and $\rho_p$ is the resistivity of the same fluid filling the pores of the material under test. The procedure consists of measuring the electrical resistance of the conducting fluid ($R_f$) and the porous sample filled with it ($R_p$). If both tests are performed in a recipient with the same volume, it is shown that

$$\tau = \Omega \frac{\rho_p}{\rho_f} = \Omega \frac{R_p}{R_f}. \tag{3.3.3}$$

Obviously this method is applicable to rubber crumb since it behaves as an electric insulator. The value finally obtained for the rubber crumb employed in this work is $\tau = 1.54$.

### 3.3.3 Porosity

The porosity is defined as the ratio of the fluid volume filling the pores to the total volume of the material. Since the grains of rubber crumb are water-resistant, liquid saturation proves to be a simple and effective method which is widely used in geological studies. A known volume of porous material is inserted in a recipient. Then water is added to fill the pores. By measuring the amount of water employed, the porosity can be directly calculated. In our case this value is $\Omega = 0.541$.

### 3.3.4 Shape factors

The parameters $\beta_1$ and $\beta_2$ are related with the attenuation of acoustic energy due to the viscous and thermal phenomena, respectively. They were obtained by fitting the absorption coefficient measured on a sample of rubber crumb with thickness $e$ in a impedance tube. At normal incidence, the theoretical coefficient $\alpha_{th}$ is related to the impedance $Z_s$ of the material by

$$\alpha_{th} = 1 - \left| \frac{Z_s - Z_0}{Z_s + Z_0} \right|^2, \tag{3.3.4}$$

$$Z_s = -iZ_c \cot(k_c e), \tag{3.3.5}$$

where $Z_c$ and $k_c$ are obtained by applying $B(\omega)$ and $\rho(\omega)$ to Eqs. (3.2.1) and (3.2.2).

Figure 3.1 shows the absorption coefficient $\alpha_{exp}$ measured for a sample with thickness $e = 9.5$ cm. It is compared with the curve $\alpha_{th}$ whose shape factors give the best fitting. The values obtained are $\beta_1 = 1.58$ m$^{-1}$ and $\beta_2 = 0.7$ m$^{-1}$. These values give the characteristic lengths $\Lambda = 142$ $\mu$m and $\Lambda' = 508$ $\mu$m.

### 3.3.5 Complete model

The physical parameters $Z_c(\omega)$ and $k_c(\omega)$ describing the rubber employed in this work crumb are depicted in Figs. 3.2 and 3.3. The frequency dependence of these curves follows the standard behaviour of granular porous media.

The real part of $k_c$ corresponds to the angular frequency $\omega$ divided by the phase velocity. Since this response is not linear, it is shown that rubber crumb

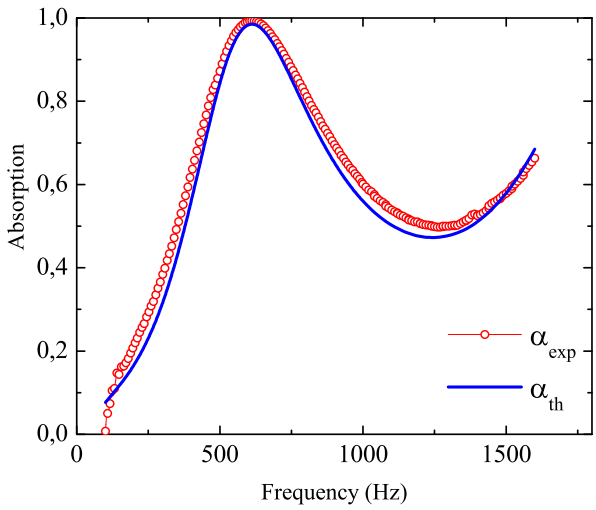


Figure 3.1: Absorption of a sample of rubber crumb with thickness $e$ = 9.5 cm measured in an impedance tube ($\alpha_{exp}$). The curve $\alpha_{th}$ is obtained from Eq. (3.3.4) with the shape factors $\beta_1 = 1.58$ m$^{-1}$ and $\beta_2 = 0.7$ m$^{-1}$ giving the best fitting.

behaves as a dispersive media whose phase velocity depends on the frequency. On the other hand, the imaginary part is related to the attenuation of waves propagating inside the material. As observed in Fig. 3.2, the attenuation increases with the frequency.

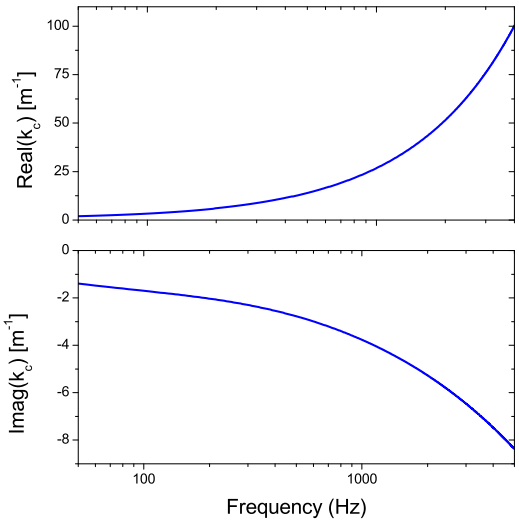


Figure 3.2: Real and imaginary parts of the complex wave number calculated through the model presented in Section 3.2.

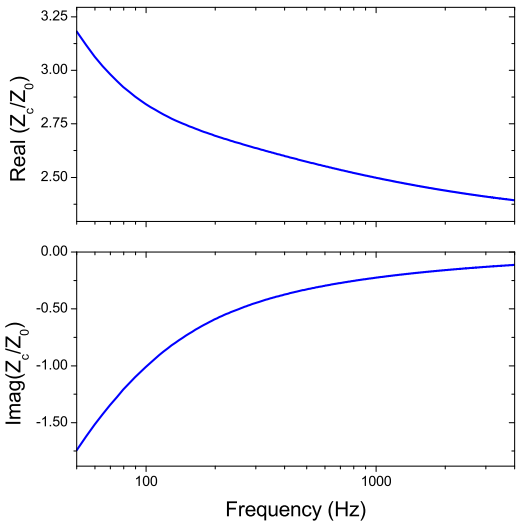


Figure 3.3: Real and imaginary parts of the characteristic impedance of rubber crumb calculated through the model presented in Section 3.2. The values are normalized by the characteristic impedance of air $Z_0 = \rho_0 c_0$.

The characteristic impedance of rubber crumb $Z_c$ of Fig. 3.3 is normalized by that of air $Z_0 = \rho_0 c_0$. It is shown that at high frequencies its imaginary part is reduced and the real part decreases towards values closer to one. Since the absorption of a semi-infinite layer of this material is given by

$$\alpha = 1 - \left| \frac{Z_c - Z_0}{Z_c + Z_0} \right|^2 , \tag{3.3.6}$$

it is shown that rubber crumb will be a better absorber at high frequencies. Note that the above formula does not depend on $k_c$. However where the sample has a finite thickness and is backed by a rigid body, the impedance $Z_c$ of the above equation becomes $-iZ_c \cot(k_c e)$, thus obtaining Eq. (3.3.4). The resulting behaviour is more complex than the case of a semi-infinite layer since now the absorption depends not only on the impedance but also on the cotangent of the wavenumber $k_c$ multiplied by the thickness $e$. This enhances the absorption at some frequencies while a lower attenuation can be found in others. Thus, the thickness of the layer of rubber crumb will be an important parameter for the design of sound absorbers.

# Chapter 4

# Experimental characterization

The theory presented in the previous chapters is supported by an experimental realization. In this chapter a set of measures is carried out on barriers made with cylinders that contain rubber crumb. The experimental setup and the measurement method are first explained. Then, measured data are shown and compared with the corresponding numerical simulations. The results are discussed and contrasted with the performance of a rigid barrier having the same dimensions than the samples.

## 4.1 Experimental setup

Experiments have been performed in an anechoic chamber of size $8\times8\times8$ m$^3$. The samples consist of 3 rows of cylindrical scatterers, each row containing 9 cylinders with a length of 1 m. They are arranged in a square configuration with lattice constant $a = 11$ cm. Figure 4.1 shows the appearance of one of the samples mounted in the anechoic chamber.

Five different samples have been measured. Their dimensions are given in Table 4.1, where the filling fraction is defined as the ratio between the cylinder volume and the total volume of the SC unit cell. For a square lattice this parameter is given by $ff = \pi R_b^2/a^2$, $R_b$ being the outer radius of the scatterers. Note that samples 1 and 2 do not contain rubber crumb, but they are made of rigid cylinders and their results will be used for comparison purposes. Samples 3, 4 and 5 are made by considering 3 different porous units. All these units consist of a porous shell with a diameter of $d_b = 8$ cm. However,

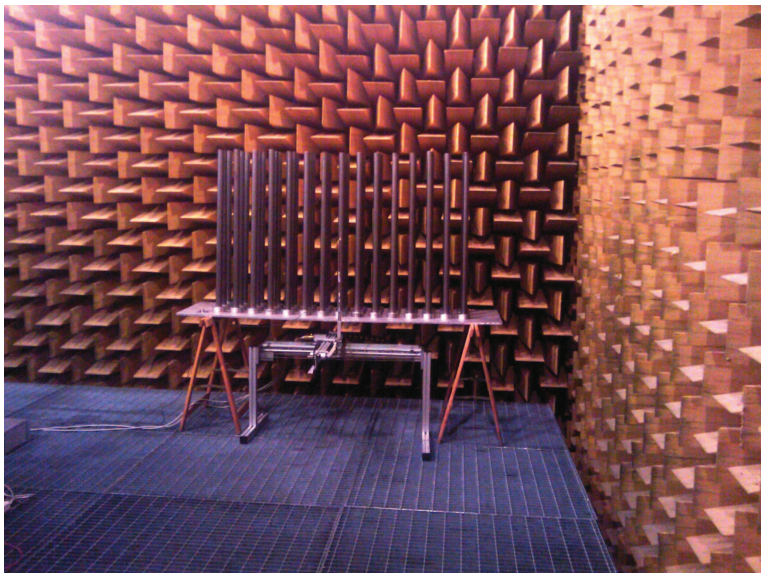

Figure 4.1: Sample mounted in the anechoic chamber. Measured samples consist of slabs with three rows of cylinders arranged in a square configuration with lattice constant $a = 11$ cm.

their inner cores (steel cylinders) have different diameters: $d_a = 4$ cm in sample 3, $d_a = 2$ cm in sample 4, and $d_a = 0$ (no core) in sample 5.

The experimental setup is illustrated in Fig. 4.2. A UDE AC-150 column speaker is used as excitation source. It is separated a distance of 4 m from the sample in order to have approximately a plane wave front at the surface of the sample. The reflection and transmission coefficients have been measured through B&K 4958 microphones placed at the equatorial plane of the samples and aligned with the central cylinder. The received signals are digitized with a NI-4551 dynamic signal analyzer for further processing.

Reflectance measurements are performed by placing both microphones between the sample and the speaker. Microphones $M1$ and $M2$ are put at distances $d$ and $\ell$ from the surface of the central cylinder, the separation between them being $\Delta d = \ell - d = 1.5$ cm. Applying white noise to the sample, the power reflection coefficient is calculated as [CB80a, CB80b]

$$R(\omega) = \left| e^{-2ik\ell} \frac{H_{12} e^{ik\Delta d} - 1}{1 - H_{12} e^{-ik\Delta d}} \right|^2 , \tag{4.1.1}$$

where $H_{12} = S_{12}/S_{11}$ is the transfer function measured between both mi-

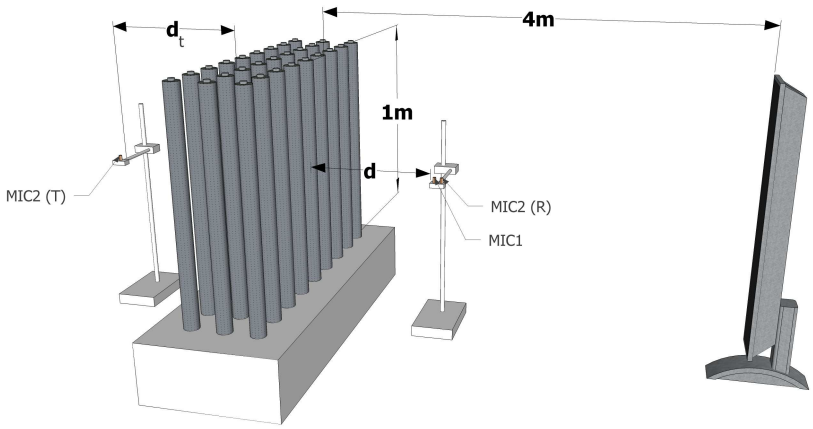


Figure 4.2: Schematic view of the experimental setup employed to characterize the samples under study. Two microphones are put in front of the barrier in order to measure reflectance. Transmittance is obtained by placing one microphone at the rear surface of the sample. A column speaker located at 4m from the sample is used as excitation source.

Table 4.1: Dimensions of the cylindrical units used in building the barrier samples studied. $d_b$ is the external diameter of the cylindrical porous shell and $d_a$ is the diameter of its inner core, which is a rigid cylinder. The column $R_b - R_a$ gives the thicknesses of the porous shells and the last column reports the filling fraction *ff* of the underlaying square lattice.

| | $d_a$(cm) | $d_b$(cm) | $R_b - R_a$ | *ff* |
|---|---|---|---|---|
| sample 1 | 4 | 4 | 0 | 0.10 |
| sample 2 | 2 | 2 | 0 | 0.03 |
| sample 3 | 4 | 8 | 2 | 0.41 |
| sample 4 | 2 | 8 | 3 | 0.41 |
| sample 5 | 0 | 8 | 4 | 0.41 |

crophones. It is calculated from the autospectrum acquired through $M1$ ($S_{11}$) and the cross-spectrum measured between both microphones ($S_{12}$). The above expression is based on a one-dimensional approach and therefore assumes that the incident, reflected and transmitted waves have plane wavefronts and travel along the direction normal to the axis of the sample. Although this model is applied to a 2D scheme, this assumption is considered valid because of the distance between the speaker and the sample and the lack of higher-order diffraction modes at frequencies below the diffraction limit of the crystalline structure. Note that the reflection coefficient from Eq. (4.1.1) cannot be determined when the distance between the microphones is an integer multiple of the half-wavelength of the sound. This fact sets an upper frequency limit that in this case is 11.3 kHz. This value is above the range of frequencies of interest and therefore it will not affect the experimental characterization. Note also that the reflection coefficient cannot be accurately obtained at very low frequencies since Eq. (4.1.1) tends to unity as the frequency goes to zero. Since such effect is limited to the low frequency range, no impact on the experimental data is expected at higher frequencies.

Transmission measurements are made with $M2$ located at the rear surface of the sample at a distance $d_t$ from the central cylinder ($M1$ is not used here). The power transmission coefficient $T$ can be estimated as the ratio between the autospectrum measured with and without sample:

$$T(\omega) = \frac{S_{22}}{S_{22}^0}. \tag{4.1.2}$$

From this measure, the insertion loss (IL) in decibels is obtained from:

$$IL(dB) = -10\log_{10}(T). \tag{4.1.3}$$

Finally, the absorption is calculated by assuming energy conservation, in such a manner that $A(\omega) = 1 - T(\omega) - R(\omega)$.

Reflectance and transmittance spectra are measured for frequencies up to 4 kHz and for three different values of $d_t$ and $d$ corresponding to 5, 10 and 20 cm. The results within that range of frequencies are consistent and repetitive for the three positions of the microphones. Hence in order to avoid the inclusion of redundant data, only spectra relative to microphones put at positions $d_t = \ell = 10$ cm will be discussed.

It is important to remark that, since we are working with periodic structures, the propagation of diffracted modes along angles $\theta_\nu$ different to the incident $\theta_0$ is possible. As shown in Chapter 2, these angles are given by:

$$\sin(\theta_\nu) = \sin(\theta_0) + \frac{2\pi\nu}{ka}, \tag{4.1.4}$$

where $\nu$ is an integer number. Taking $\theta_0$ =0, the first diffracted mode appears when $ka = 2\pi$, i.e. when $\lambda = a$ and $\theta_{\pm 1}$ becomes a real number. This condition defines the diffraction limit and gives a frequency cut-off such that, for higher frequencies, Eq. (4.1.1) is not longer valid since reflected and transmitted waves propagate with wavevectors not collinear with that of the incident wave. In other words, for wavelengths smaller than $a$ some energy is scattered to angles different to the ballistic and will cause the failure of the measurement method due to the non satisfied condition of incident, reflected and transmitted waves travelling along the same direction in the setup. Therefore, no discussion of data will be performed above the diffraction limit. Anyway, it is noted that Eq. (4.1.1) can still be used in the frequency regions corresponding to the first bandgap because it appears at frequencies bellow the diffraction limit where the transmission reduction is due to the destructive interference between waves reflected on the successive layers of cylinders and the incident wave.

In order to compare the experimental results with the theoretical model, numerical simulations have been carried out by making use of the multiple scattering theory presented in Chapter 2. The T matrices of samples 3 and 4 have been calculated through Eq. (2.2.24), while the matrix of sample 5 is computed with Eq. (2.2.14). The parameters describing the rubber crumb in these equations have been obtained through the model provided in Chapter 3. Simulations are performed by reproducing the experimental configuration. It is assumed an incident plane wave impinging on a cluster with the same dimensions and number of cylinders than the samples. The sound pressure is calculated at the points where the microphones are placed in the experiment. A frequency sweep is performed and Eq. (4.1.1) is evaluated at each frequency by taking $H_{12} = p_2/p_1$, where $p_1$ and $p_2$ are the pressure values measured at the positions of $M1$ and $M2$, respectively. The same process is performed for Eq. (4.1.2), where $S_{22}$ is replaced by $|p_2|^2$. The main difference between the theoretical approach and the experiments is that multiple

scattering calculations assume infinitely long cylinders. This assumption is reasonable for the experimental setup since the data are acquired very close to the sample surface and therefore the effects associated to the diffraction from the borders are reduced.

## 4.2 Results

### 4.2.1 Barrier made of rigid cylinders

Figures 4.3 and 4.4 show the results for SC barriers made of only rigid cylinders with diameters of 4 cm and 2 cm, corresponding to samples 1 and 2 in Table 4.1, respectively. For the sake of comparison, the band structures along the direction normal to the axis of the slabs are also shown. The acoustic bands have been calculated by the procedure described in Section II of Ref. [GY03] where it is solved the secular equation obtained by taking into account that, in a periodic system, the Bloch theorem applies to the coefficients $(A_\alpha)_q$ introduced in Chapter 2.

It is observed that, in the frequency region where the band gap is predicted (black stripes), a peak appears in the reflectance spectrum while a minimum is found in the transmission. These features are barely seen in sample 2, which is made of very thin cylinders and, therefore, has a small filling fraction. Better defined peaks and valleys can be obtained if a larger number of layers were employed in building the barrier [SPCMS$^+$98]. With regard to the absorption spectrum, it is shown that it remains around zero. This fact is in agreement with the lack of absorptive phenomena in samples made with rigid scatterers. Note that the measured data (red dots) are well reproduced by the numerical simulations based on the multiple scattering theory (continuous lines).

It is noticeable in Figs. 4.3 and 4.4 that values larger than unity appear in the reflectance or transmittance spectra for frequencies above 3 kHz. These values are unphysical and are due to the fact that expressions employed in their calculations lost their validity. As mentioned before, Eqs. (4.1.1) and (4.1.2) were obtained under the approach of a plane wavefront propagating along the direction normal to the axis of the sample. According to Eq. (4.1.4) the excitation of Bragg waves with $\nu \neq 0$ approximately starts around $\lambda = a$.

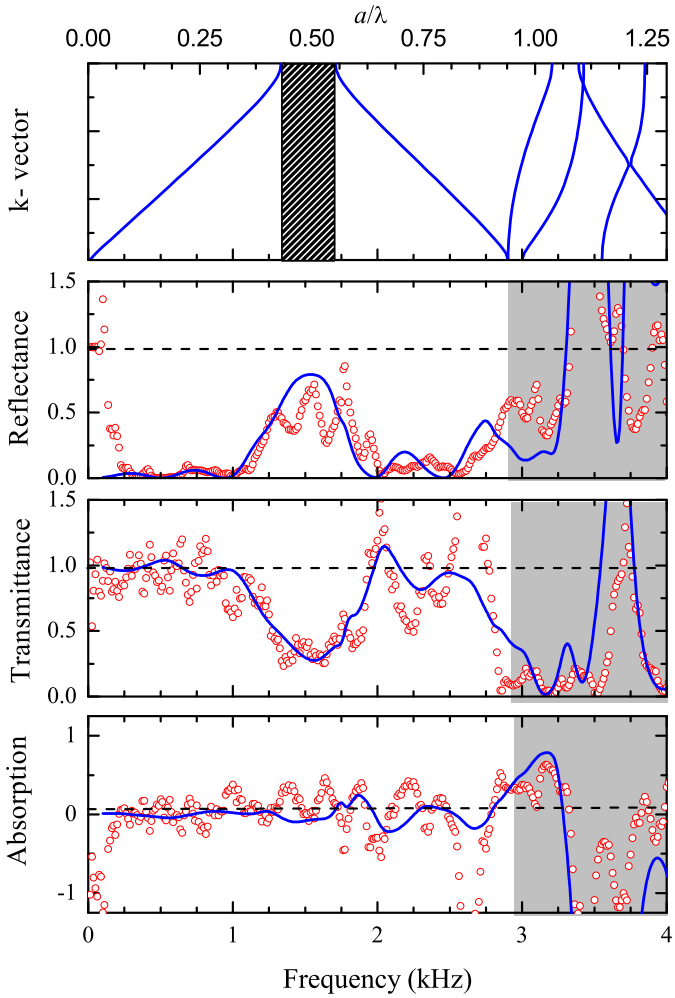


Figure 4.3: Band structure, reflectance, transmittance and absorption spectra measured (red dots) and calculated (solid blue lines) for a noise barrier made of three rows of metal cylinders with 4 cm of diameter (sample 1 in Table 4.1). The shadowed regions define the frequencies above the diffraction limit and the black stripe in the acoustic band structure (top panel) defines the bandgap of the underlaying square lattice. The horizontal dashed lines are guides for the eye.

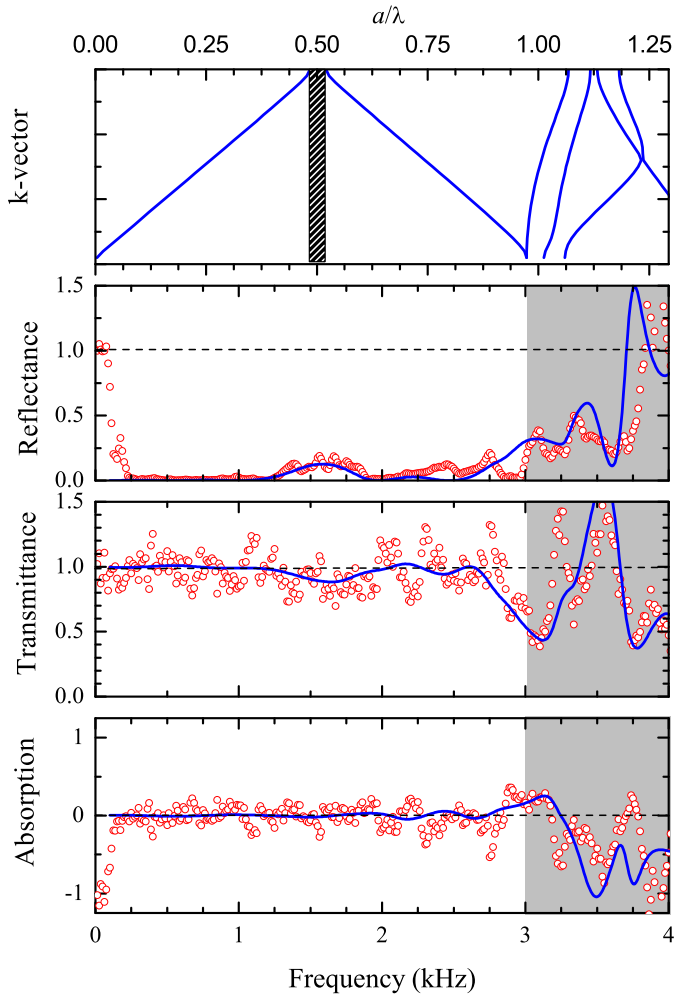


Figure 4.4: Band structure, reflectance, transmittance and absorption spectra measured (red dots) and calculated (solid blue lines) for a noise barrier made of three rows of metal cylinders with 2 cm of diameter (sample 2 in Table 4.1). The shadowed regions define the frequencies above the diffraction limit and the black stripe in the acoustic band structure (top panel) defines the bandgap of the underlaying square lattice. The horizontal dashed lines are guides for the eye.

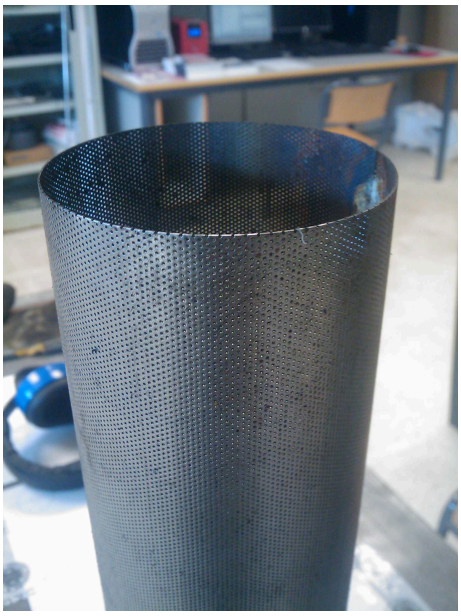

Figure 4.5: Hollow cylinder with 8 cm of diameter made from a 0.5 mm-thick perforated plate whose holes have a diameter of 0.5 mm. Due to its acoustic transparency, this shell is suitable for containing rubber crumb without modifying its properties.

An exact determination of this cutoff is obtained from the acoustic band structure, which gives about 2.8 kHz for sample 1 and 3 kHz for sample 2. Moreover, a disagreement between the measured and calculated data can be observed in the reflectance spectra at low frequencies. This discrepancy is due to the fact that Eq. (4.1.1) tends to unity in the low frequency limit, as previously stated.

### 4.2.2 Barrier made of rubber crumb cylinders

The rubber crumb cylinders are fabricated by inserting this granular material inside hollow cylinders made with perforated plates. This procedure is a practical alternative to the use of binders in order to obtain rigid structures of rubber crumb. The perforated plates here employed are made with steel and have a thickness of 0.5 mm. They are perforated with holes having a diameter of 0.5 mm and arranged in a hexagonal distribution with a separation of 1.25 mm between holes. The resulting shell is shown in Fig. 4.5. The acous-

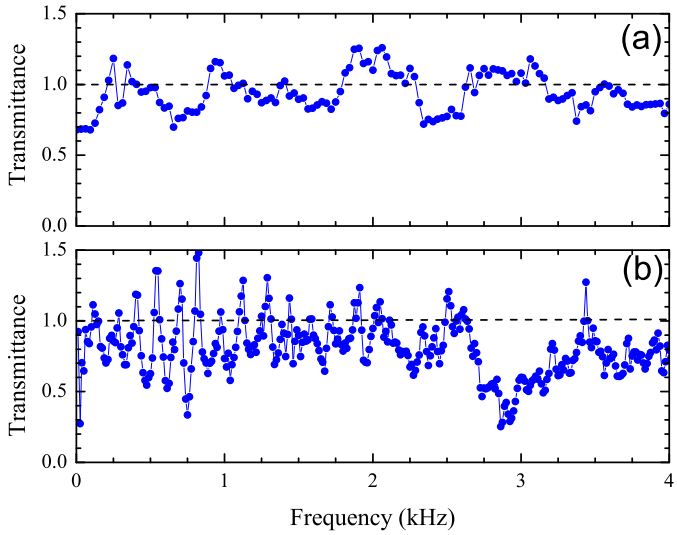


Figure 4.6: (a) Transmittance of a flat perforated plate with a thickness of 0.5 mm. The perforations are circular holes with a diameter of 0.5 mm. (b) Transmittance through a SC structure consisting of three rows of 8 cm-diameter cylinders fabricated with the perforated plates above characterized. The dashed horizontal lines are guides for the eye.

tic properties of the flat perforated plate as well as the hollow shells have been experimentally characterized. Figure 4.6(a) shows the transmission coefficient of a flat plate measured at 10 cm from its rear surface by following the same procedure as in the case of the samples under study. From this spectrum it can be concluded that the plate is almost acoustically transparent for a normally incident sound. Similar conclusions can be drawn from the measurement of a lattice of hollow perforated shells. A high transparency is observed in the transmittance spectrum depicted in Fig. 4.6(b), which corresponds to a barrier consisting of three layers of hollow cylinders with 8 cm of diameter. Note that this structure is transparent enough until 4.0 kHz and, therefore, it will be assumed that the absorption effects observed after their filling in will be associated solely to the absorptive properties of the rubber crumb.

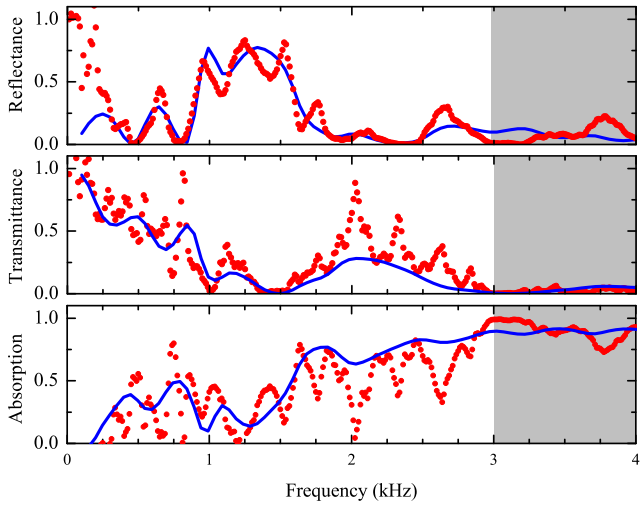


Figure 4.7: Reflectance, transmittance and absorption spectra measured (red dots) and calculated (continuous blue lines) for a noise barrier made of rubber crumb cylinders with 8 cm of diameter containing a rigid core with 4 cm of diameter (sample 3 in Table 4.1).

Figures 4.7, 4.8 and 4.9 show the spectra of samples 3, 4 and 5, respectively. As in the case of SC barriers based on rigid cylinders, it is obtained an overall good agreement between measurements (red dots) and numerical

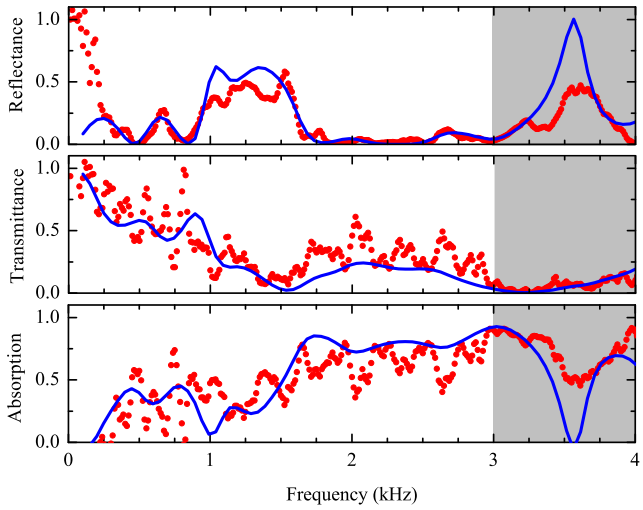


Figure 4.8: Reflectance, transmittance and absorption spectra measured (red dots) and calculated (continuous blue lines) for a noise barrier made of rubber crumb cylinders with 8 cm of diameter containing a rigid core with 2 cm of diameter (sample 4 in Table 4.1).

simulations (continuous blue lines). In comparison with the case of samples 1 and 2, there absorption spectra show significant levels because of the attenuation properties of rubber crumb. Note that the absorption increases with the frequency due to the higher imaginary part of the wave number $k_c$ of the rubber crumb and the better impedance matching with air, as shown in Chapter 3. Moreover no spurious results are observed in reflectance and transmittance spectra above the diffraction limit since the high absorption avoid their appearance. However, the data above this limit are unreliable because the measurement method cannot account for the propagation of diffracted modes, and therefore the slabs should be characterized by other means.

It is shown that absorption is similar in the three samples at frequencies below the bandgap. At the bandgap frequencies and above this range the absorption of sample 5 is in general slightly higher, which is in agreement with the larger amount of rubber crumb contained in the cylinders with no core. Regarding the reflectance, the three samples have bandgaps centered at

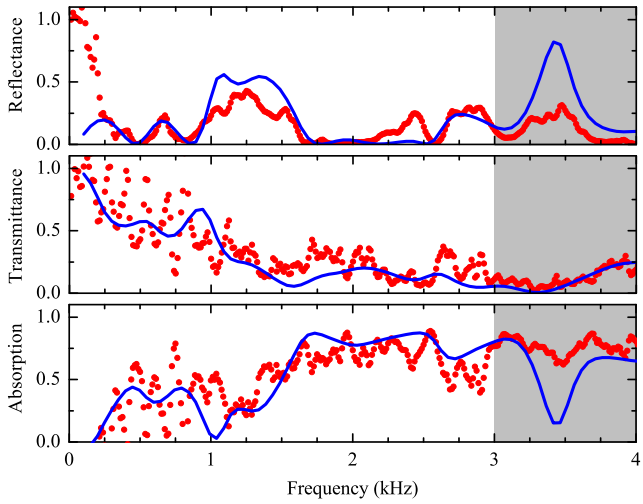


Figure 4.9: Reflectance, transmittance and absorption spectra measured (red dots) and calculated (continuous blue lines) for a noise barrier made of rubber crumb cylinders with 8 cm of diameter (sample 5 in Table 4.1).

the same frequency and with similar bandwidths. This fact is easily explainable since all the samples have the same lattice constant and filling fraction. However it is shown that the peak is stronger for the case of sample 3, made of cylinders with a thicker core, and weaker for sample 5, which is made of cylinders with no core.

## 4.3 Discussion

The measured and calculated insertion losses of the different samples are depicted in Figs. 4.10 and 4.11, respectively. The black dashed lines in these figures represent the IL calculated for a rigid wall with the same dimensions than the SC barriers, i.e., 30 cm thick and 1 m height. These values have been obtained by applying the procedure described in the norm ISO9613 [ISO96], which basically accounts for the field diffracted by the barrier edges. It is observed that the SC barriers based on three rows of rigid cylinders show very low attenuation in comparison with the rigid wall. The attenuation is strongly enhanced by using porous cylinders as building blocks and their

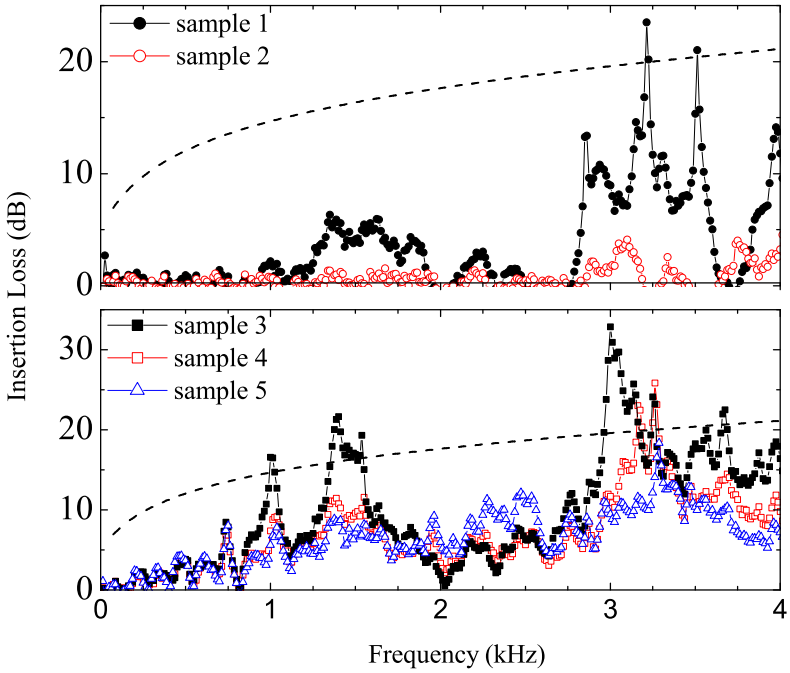


Figure 4.10: Insertion losses of the samples described in Table 4.1. The dashed lines represent the IL predicted for a rigid wall having the same external dimensions than the samples.

qualities approach the one of a rigid wall in some frequency regions. This behaviour is produced by two effects: the higher filling fraction of the SC caused by the porous overlayer and the absorptive properties of the rubber crumb. Note that the improvement of attenuation is produced in the overall range of frequencies, since rubber crumb provides a broadband absorption mechanism unlike reflection-based attenuation which only occurs at bandgap frequencies.

Moreover, it is also observed that the shell containing the thicker core presents a huge enhancement of the IL, which even overcomes the IL of the corresponding rigid wall in certain frequency regions. At these frequencies, the field transmitted through the barrier becomes comparable to that diffracted by its edges and the overall attenuation could depend on the measuring point due to an interference phenomenon. However this effect only

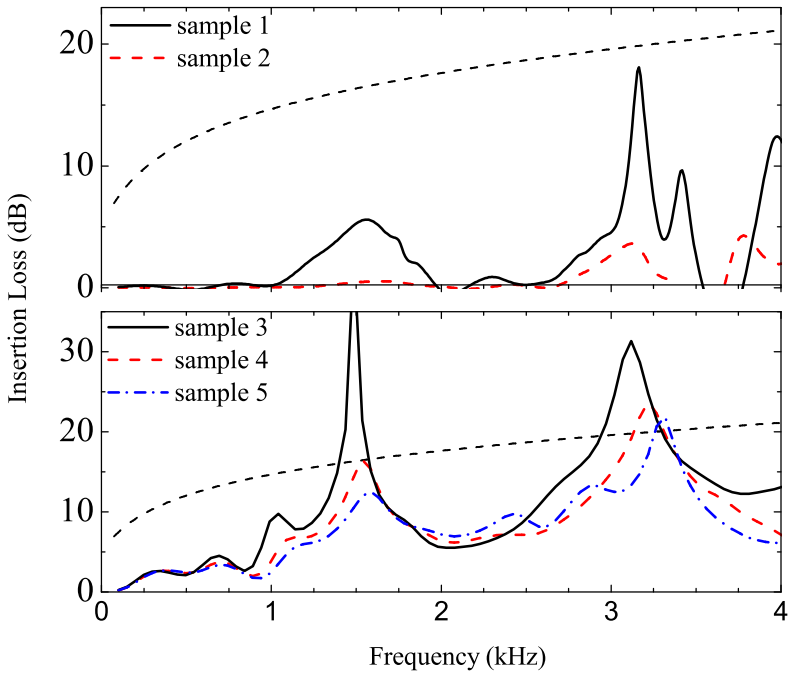


Figure 4.11: Theoretical predictions of the insertion losses of the samples described in Table 4.1. The dashed lines represent the IL predicted for a rigid wall having the same external dimensions than the samples.

takes place where the sample overcomes a rigid wall, the barrier being highly efficient in such a case. The high attenuation found in Sample 3 is confirmed by the simulations and is consistent with the remark given at the end of Chapter 3. Thus, it is concluded that the thickness of the porous layer plays a major role in the attenuation characteristics of the barrier, and its value should be properly determined in the design procedure of efficient noise barriers.

# Chapter 5

# Optimum barrier design

In the last chapters a numerical model for the calculation of noise barriers made with cylinders containing rubber crumb was developed and experimentally validated. The next step consists of designing specific barriers that efficiently attenuates a given noise profile, which in this case is traffic noise. This task has been performed through an optimization procedure that maximizes the performance of the barrier according to the criteria defined in the European normative. The theoretical model presented in the last chapters will be extended to account for the actual characteristics of traffic noise and, in addition, the presence of two parallel barriers will be considered in order to analyse a more realistic approach.

## 5.1 Introduction

As mentioned in Chapter 1, the design of optimized noise barriers leads to complex problems where purely analytic approaches are ineffective. Instead, optimization algorithms are a powerful tool which allow obtaining complex geometries and material distributions that improve the efficiency of the barrier. Several works have been reported in this topic, either based on convectional [Duh06, BDJ08, BDJ07] or SC-based barriers [RGSPGR$^+$09, RGSPGR$^+$08, HGNB$^+$08].

In the case of sonic crystals, the optimization processes reported are carried out by means of the creation of vacancies in the structure, i.e., by removing specific cylinders of the crystal. According to other optimization works

in this field [HCSD05, HSDC06], the authors used genetic algorithms since they are able to deal with discrete vacancy-based optimizations with large search spaces. High attenuations and reasonable bandwidths are achieved for noise barriers designed through this technique. For instance, an averaged attenuation of 27 dB between 2300 and 3700 Hz was reported for barriers based on rigid cylinders [HGNB$^+$08]. However these works take into account only normally incident sound waves, neglecting waves arriving to the barrier from other directions. This approach is not practical since noise is often assumed to be a diffuse field, where all directions of propagation are equally probable. Optimized designs for normal incidence, may not work as well at oblique incidence.

Moreover, neither of the cited optimization works takes into account a common scheme where noise barriers are placed on opposite sides of a road. In these circumstances multiple reflected sound between parallel barriers can cause a significant increase in noise in the screened area [Wat96, HJPR85]. This effect will be greater when distance between barriers is small and in the case of highly reflective barriers where no absorption mechanisms are included. Also multiple reflections between the barrier and vehicles, especially those large such as trucks, contribute to the reduction of isolation.

As concluded in Chapter 4, cylinders composed of a rigid core covered by an absorbent layer of rubber crumb present attenuation spectra which depends of the thickness of both the core and the porous layer. A noise barrier containing several rows made with these cylinders is a complex system, especially when considering that the cylinders of each row can be different as well as the distances between rows. This justifies the use of an optimization algorithm in order to find the best geometry of the sonic crystal that reduces the transmission of sound.

## 5.2 Multiple reflection model

By assuming an incoherent source, the problem of multiple reflections can be approached with a ray model where the total energy in a given point corresponds to the sum of the energies of the different arriving rays [Hur80]. In this context the simplified one-dimensional model shown in Fig. 5.1 has been used. Here a noise source between two parallel barriers emits a plane

wave with energy $E_0$ to one of the barriers. Each time the wave impinges on a barrier, a fraction $\mathcal{T}$ of the incident energy is transmitted to the other side, another fraction $\mathcal{R}$ is reflected and the rest $1 - \mathcal{R} - \mathcal{T}$ is absorbed. We can define an effective transmission coefficient as the fraction of energy transmitted through both barriers:

$$\mathcal{T}_{eff} = \mathcal{T} \sum_{n=0}^{+\infty} \mathcal{R}^n = \frac{\mathcal{T}}{1 - \mathcal{R}}. \tag{5.2.1}$$

This model can be modified by assuming an attenuation proportional to

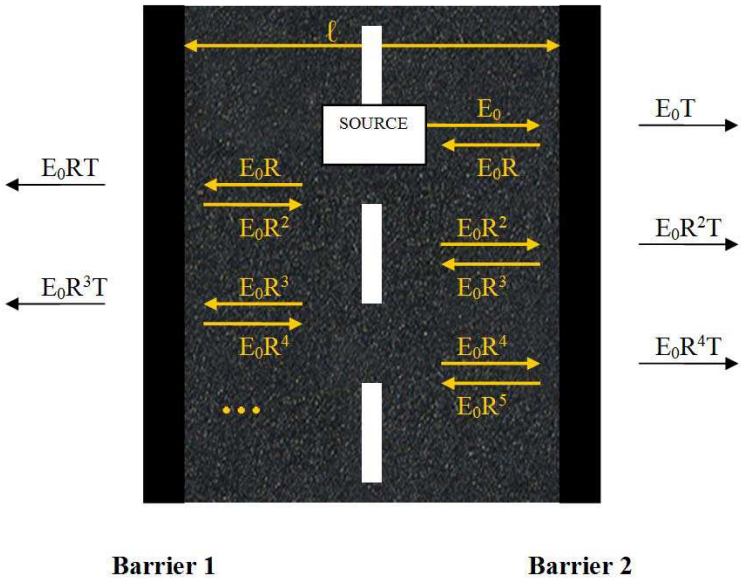


Figure 5.1: Scheme of a multiple reflection model. The power in $\mathcal{R}$ defines the number of reflections experienced by the sound wave with initial energy $E_0$

$1/r$ ($r$ being the travelled distance) due to geometrical spreading, which corresponds to a cylindrical wave front:

$$T'_{eff} = 2\frac{T}{\ell} \sum_{n=0}^{+\infty} \frac{R^n}{2n+1} = 2\frac{T}{\ell} \frac{\operatorname{arctanh}\left(\sqrt{R}\right)}{\sqrt{R}}, \tag{5.2.2}$$

where $\ell$ is the separation between barriers. Also attenuation by a factor $1/r^2$ can be considered, modelling a point source with spherical spreading:

$$T''_{eff} = 4\frac{T}{\ell^2}\sum_{n=0}^{+\infty}\frac{R^n}{(2n+1)^2}. \tag{5.2.3}$$

In a first approach a road vehicle can be regarded as a punctual source, so its sound level decreases 6 dB per doubling of distance due to spherical spreading. However when considering an infinitely long and straight road, a continuous traffic approximately behaves as a line source in such a manner that, at enough distance from the individual sources, sound levels fall 3 dB per doubling of distance as a cylindrical wavefront does [Emb96]. In fact there are numerous traffic noise models, some of them considering the noise source as incoherent punctual sources and other as a line source [Ste01]. Because of this, the three cases covered by Eqs. (5.2.1), (5.2.2) and (5.2.3) will be discussed.

## 5.3 Optimization model

The objective function to maximize is the airborne insulation index ($DL_R$), which is used in Europe as a criterion to classify the acoustic performance of traffic noise barriers. It is defined in the European normative EN 1793-2 as [EN 97]

$$DL_R = -10\log_{10}\left|\frac{\sum_{i=1}^{18}10^{-0.1R_i}10^{0.1L_i}}{\sum_{i=1}^{18}10^{0.1L_i}}\right|, \tag{5.3.1}$$

where $L_i$ is the normalized traffic spectrum, $R_i$ is the sound transmission loss and $i$ is an index indicating the 18 standard third octave bands with frequencies from 100 Hz to 5 kHz. Parameters $L_i$ take into account the human hearing response and emphasizes the frequencies where traffic noise is more undesirable, having a maximum weight into the 1 kHz band. The measurement of $R_i$ is standardized in the norm ISO10140-2 [ISO10]. The procedure consists of applying a diffuse sound field to the barrier into a transmission chamber and measuring the sound levels at both sides of the sample as well as the reverberation time. Note that the norm EN 1793 is intended to characterize the intrinsic properties of the barrier, disregarding

*in situ* conditions. Because of this, no discussion about diffraction by the top end of the cylinders or ground effects will be provided in this work.

The structure to be optimized consists of a SC with three infinite rows of cylinders where each cylinder has an inner rigid core of radius $r_{ik}$ (with $k = 1, 2, 3$) and a layer of rubber crumb between the core and an external radius $r_k$ (see Fig. 5.2). Each row has identical cylinders separated by a distance $D$ and the three rows are separated by distances $d_1$ and $d_2$. Therefore the optimization model involves nine independent parameters. Note that the cylinders are arranged in a square lattice, thus lowering the flow resistance of the barrier and making it partially transparent to light. For comparison purposes, it is also studied a barrier in which cylinders at the middle row are displaced a distance $D/2$, being placed in the dashed circles in Fig. 5.2. Since this structure forbids the light passing through, it will be called opaque barrier.

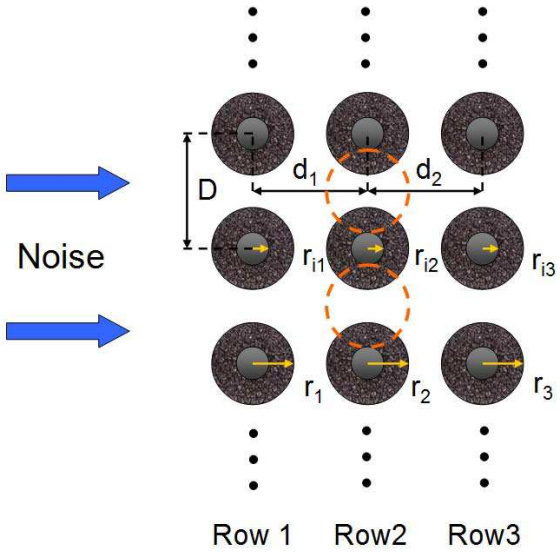


Figure 5.2: Geometric parameters employed in the optimization of a noise barrier based on a SC. The barrier consists of three rows of cylindrical scatterers containing rubber crumb. The dashed circles indicate the positions of cylinders for the opaque configuration.

The calculations of the SC parameters have been performed by applying the multiple scattering theory. As shown in Chapter 2, from this framework it

is possible to calculate the reflectance $\mathcal{R}_{SC}$ and transmittance $\mathcal{T}_{SC}$ of infinite slabs by integrating the energy flux in a unity cell, leading to the expressions

$$\mathcal{T}_{sc}(\theta_0) = 1 + 2\Re\left[C_0^+\right] + \sum_{\cos\theta_\nu \in \Re} \frac{|\cos\theta_\nu|}{\cos\theta_0} \left|C_\nu^+\right|^2, \tag{5.3.2}$$

$$\mathcal{R}_{sc}(\theta_0) = \sum_{\cos\theta_\nu \in \Re} \frac{|\cos\theta_\nu|}{\cos\theta_0} \left|C_\nu^-\right|^2, \tag{5.3.3}$$

where $\theta_0$ is the angle of propagation of the impinging plane wave with respect to normal incidence. $C_\nu^-$ and $C_\nu^+$ are the amplitudes of the reflected and transmitted $\nu$-modes which propagate at an angle $\theta_\nu$, obtained through the expression

$$\sin\theta_\nu = \sin\theta_0 + \frac{2\pi\nu}{kD}, \tag{5.3.4}$$

$k$ being the wavenumber in air and $\nu$ an integer. The absorption of the barrier is then calculated by assuming energy conservation, so $\mathcal{A}_{SC} = 1 - \mathcal{T}_{SC} - \mathcal{R}_{SC}$. The acoustic model used in describing the rubber crumb is based on the theory exposed in Chapter 3.

Multiple scattering theory works with coherent waves with well defined wave fronts, making difficult to model the diffuse sound field required by the ISO10140 norm. Since this type of field is the basis of several standardized measurements, analytical predictions have been developed in control noise research. A conventional calculation is based on the assumption that the angular distribution of incident sound field on the surface of the sample becomes fully uniform [Kut09]. Consider a surface element of the sample $dS$ and an isotropic incident sound intensity $I$. The fraction of acoustic power that arrives to $dS$ from the direction defined by the solid angle $d\Omega$ is

$$dP_i = I\cos(\theta) dS d\Omega = I dS \cos(\theta) d\varphi d\theta, \tag{5.3.5}$$

where $\theta$ and $\varphi$ correspond to the azimuth and the inclination angles in spherical coordinates, respectively. The total arriving power is calculated by integrating Eq. 5.3.5 over the surface of a semi sphere

$$P_i = \int_0^\pi \int_0^{2\pi} I dS \cos(\theta)\sin(\theta) d\varphi d\theta = \pi I dS. \tag{5.3.6}$$

Similarly, the total transmitted power is obtained as

$$P_t = \int_0^\pi \int_0^{2\pi} I\mathcal{T}(\theta) dS \cos(\theta)\sin(\theta) d\varphi d\theta = \pi I dS \int_0^{\pi/2} \mathcal{T}(\theta)\sin(2\theta) d\theta, \tag{5.3.7}$$

$\mathcal{T}(\theta)$ being the angle-dependent transmission coefficient, that is supposed to be independent of $\varphi$. The angle averaged transmission coefficient is given by the ratio

$$\mathcal{T}_{av} = \frac{P_t}{P_i} = \int_0^{\pi/2} \mathcal{T}(\theta) \sin(2\theta) d\theta. \tag{5.3.8}$$

However a uniform distribution does not fully reflect the actual sound field, so an angle-dependent correction based on a Gaussian distribution is applied [KIKK00, KIKK02]. Hence the averaged transmission coefficient of the barrier is calculated as

$$\mathcal{T}_{av}(\omega) = \frac{\int_0^{\pi/2} e^{-\theta^2} \mathcal{T}_{SC}(\omega, \theta) \ \ sin(2\theta) \ d\theta}{\int_0^{\pi/2} e^{-\theta^2} \sin(2\theta) \ d\theta}, \tag{5.3.9}$$

and the same procedure can be applied to reflection and absorption coefficients, giving $\mathcal{R}_{av}(\omega)$ and $\mathcal{A}_{av}(\omega)$ from $\mathcal{R}_{SC}(\omega, \theta)$ and $\mathcal{A}_{SC}(\omega, \theta)$, respectively.

Coefficients $R_i$ in Eq. 5.3.1 are calculated as $1/\mathcal{T}_x$ where $\mathcal{T}_x$ is the direct $\mathcal{T} = \mathcal{T}_{av}$ or effective $\mathcal{T}_{\mathit{eff}}$, $\mathcal{T}'_{\mathit{eff}}$, $\mathcal{T}''_{\mathit{eff}}$ transmission coefficients obtained by applying $\mathcal{T}_{av}$ and $\mathcal{R}_{av}$ to Eqs. (5.2.1)-(5.2.3). These parameters are calculated at several frequencies in each one-third octave band and then they are integrated in order to get a single $R_i$ per band.

Due to the difficulty of differentiating the nine-dimensional objective function, it is employed the Nelder-Mead optimization method, which is based on the simplex algorithm [NM65]. With the purpose of globalize the search, several initializations have been programmed in order to ensure that no local maximums are reached. Physical constraints such as positive dimensions or no overlapped cylinders have been taken into account in the algorithm. Also practical constraints like a maximum barrier width of 1 m and a maximum external radii of 10 cm have been configured. A distance $D$ at least four times the maximum radius is set for the transparent topology in order to design barriers with low filling fractions. For the case of the opaque barrier, a minimum distance between cylinders of 1 cm is considered.

## 5.4 Results

Results from the optimization process are shown in Table 5.1, where a distance $\ell = 10$ m between parallel barriers has been assumed in Eqs. (5.2.2)

Table 5.1: Barrier parameters (see Fig. 5.2) obtained by the optimization algorithm. Length dimensions are in cm. Last row contains the airborne insulation index $DL_R$ in dB.

| | $\mathcal{T}$ | | $\mathcal{T}_{eff}$ | | $\mathcal{T}'_{eff}$ | | $\mathcal{T}''_{eff}$ | |
|---|---|---|---|---|---|---|---|---|
| | □ | △ | □ | △ | □ | △ | □ | △ |
| $r_1$ | 10.0 | 10.0 | 10.0 | 10.0 | 10.0 | 10.0 | 10.0 | 10.0 |
| $r_2$ | 10.0 | 10.0 | 10.0 | 10.0 | 10.0 | 10.0 | 10.0 | 10.0 |
| $r_3$ | 10.0 | 10.0 | 10.0 | 10.0 | 10.0 | 10.0 | 10.0 | 10.0 |
| $r_{i1}$ | 4.6 | 10.0 | 3.4 | 5.1 | 4.2 | 7.3 | 4.5 | 9.2 |
| $r_{i2}$ | 4.3 | 5.0 | 4.0 | 4.3 | 4.3 | 4.1 | 4.3 | 3.8 |
| $r_{i3}$ | 4.7 | 9.5 | 4.5 | 10.0 | 4.6 | 10.0 | 4.7 | 9.4 |
| $d_1$ | 32.1 | 18.2 | 31.2 | 18.2 | 31.8 | 18.2 | 32.1 | 18.2 |
| $d_2$ | 48.9 | 18.2 | 49.8 | 18.2 | 49.1 | 18.2 | 48.9 | 18.2 |
| $D$ | 40.0 | 21.0 | 40.0 | 21.0 | 40.0 | 21.0 | 40.00 | 21.0 |
| $DL_R$ | 7.2 | 18.6 | 6.7 | 16.6 | 14.0 | 24.7 | 21.1 | 32.1 |

and (5.2.3). It is noticeable that, for the case of opaque barriers (△ symbols in Table 5.1), the algorithm has always converged to the restrictions of maximum external radius and minimum distance between cylinders, that is, trying to make the SC more compact. The same applies to the case of the transparent barriers (□ symbols) where minimum distance $D$ and maximum radius are also obtained. In addition, distances $d_1$ and $d_2$ are practically the same for each transmission model in this topology.

Looking closer to the dimensions obtained, especially the internal radii, it is observed that the cases based on effective transmission $\mathcal{T}'_{eff}$ and $\mathcal{T}''_{eff}$ tend to the values obtained for the case of simple transmission $\mathcal{T}$ as the attenuation by geometrical spreading of waves increases. This fact is logical since multiple reflections are negligible when the attenuation by wave propagation is large, becoming only important the first incidence of the wave in the barrier. Note that differences in $DL_R$ between the $\mathcal{T}$ and $\mathcal{T}'_{eff}$, $\mathcal{T}''_{eff}$ cases are mainly due to the attenuation occurring along the path from the source to the first barrier. Therefore models $\mathcal{T}$ and $\mathcal{T}_{eff}$ models can be regarded as two extreme approaches. Practical cases will fall within them depending on their propagation attenuation and the distance between barriers. While in wide highways $\mathcal{T}'_{eff}$ and $\mathcal{T}''_{eff}$ models will obtain parameters that approach those given by $\mathcal{T}$,

situations such as narrow roads or railway lines will make these parameters closer to the $\mathcal{T}_{\mathit{eff}}$ model.

It is worth noting that for the case of simple transmission $\mathcal{T}$ there are two insulation mechanisms available: reflectance by the barrier periodic structure and absorption by the material of its building units. However the $\mathcal{T}_{\mathit{eff}}$ model only employs absorption since reflected waves always reach the opposite barrier without being attenuated during propagation. The practical constrain of minimum distance $D$ imposed to the optimization of the transparent barriers has avoided the chance of using reflection as the principal attenuation mechanism (band gaps cannot be formed in an efficient way). Therefore the optimization process has always chosen improving the absorption, thus resulting in barrier structures with similar parameters in the four transmission cases. On the other hand, for the opaque barrier where distances between cylinders are not so constrained, larger differences are found between the optimized parameters from the different transmission models. The configuration obtained from the $\mathcal{T}$ model needs larger rigid cores, especially in the first row, while the barrier derived from the $\mathcal{T}_{\mathit{eff}}$ model requires more rubber crumb. This fact highlights the differences between the transmission models in such a manner that in the first case a reflective barrier is obtained while the second corresponds to a barrier based on absorption phenomenon. The angular-averaged reflection $\mathcal{R}_{av}(\omega)$ and absorption $\mathcal{A}_{av}$ of these two cases are represented in Fig. 5.3, which shows how the barrier obtained from model $\mathcal{T}$ has a high reflective spectrum but a low absorption profile, while that resulting from model $\mathcal{T}_{\mathit{eff}}$ has an opposite behavior.

## 5.5 Experimental Verification

To support the theoretical predictions, a 3 m high by 4.5 m long barrier has been constructed and experimentally characterized in a transmission chamber (see Fig. 5.4). Due to practical limitations, the optimized dimensions in Table 5.1 have been slightly modified, so that building parameters are $r_1 = r_2 = r_3 = 10$ cm, $r_{i1} = r_{i2} = 0$, $r_{i3} = 4.5$ cm, $d_1 = 30$cm, $d_2 = 50$ cm and $D = 42$ cm. Theoretically the expected $DL_R$ of this barrier differs by less than 0.5 dB with respect to the optimized results reported in Table 5.1.

The sound transmission loss coefficients $R_i$ have been measured by fol-

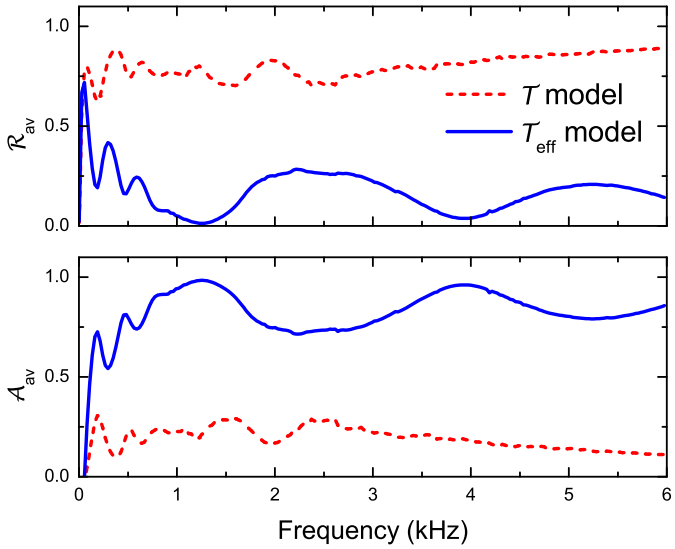


Figure 5.3: Angular-averaged reflection $\mathcal{R}_{av}(\omega)$ and absorption $\mathcal{A}_{av}(\omega)$ of the opaque barriers optimized through the $\mathcal{T}$ and $\mathcal{T}_{\mathit{eff}}$ models.

lowing the ISO10140-2 norm [ISO10]. In brief, a loudspeaker is placed at the source room of the transmission chamber and generates a white noise that becomes a diffuse sound field due to the multiple reflections on the room walls. Sound levels in source and receiver rooms (L1 and L2, respectively) are acquired with moving microphones in such a manner that the sound field is averaged in time and space. The transmission loss $R_i$ for each normalized one-third octave band is obtained as

$$R_i(dB) = L_1 - L_2 + 10\log\left(\frac{S}{A}\right), \tag{5.5.1}$$

where $S$ is the surface of the sample and $A$ is the equivalent absorption area of the receiver room. The parameter $A$ is obtained through the reverberation time $T$ measured in the receiver room applied to Sabine's equation

$$A = \frac{0.16V}{T}, \tag{5.5.2}$$

$V$ being the volume of the receiving room.

Figure 5.5 shows the $R_i$ coefficients measured (hollow squares) and calculated through models $\mathcal{T}$ (bold circles) and $\mathcal{T}_{\mathit{eff}}$ (bold triangles). According

Figure 5.4: Photograph taken inside the transmission chamber. The barrier is schematically described in Fig. 5.2 and has parameters $r_1 = r_2 = r_3 = 10$ cm, $r_{i1} = r_{i2} = 0$, $r_{i3} = 4.5$ cm, $d_1 = 30$ cm, $d_2 = 50$ cm and $D = 42$ cm.

to the absorptive properties of rubber crumb, the responses of attenuation obtained increase as frequency does. Note that although a bandgap is expected in the reflectance spectrum, it does not appear in Fig. 5.5 because the angular and frequency average performed on the $R_i$ coefficients smoothes the response. The agreement between theoretical predictions and experiment is remarkable, being the obtained experimental value of $DL_R = 6.78$ dB, close to those predicted by the two models. Theory and experiment differ only at low frequencies where normal modes of the room become important, resulting in a not completely diffuse acoustic field. Moreover both models produce similar curves due to the reduced reflectance of the barrier.

For comparison purposes, the case of SC barrier made of only rigid cylinders (with the same external radii) has been also considered and its coefficients are depicted in Fig. 5.5. Note that its corresponding quality factor has been strongly reduced in comparison with rubber crumb barrier, where absorption is the mechanism leading to the broadband sound attenuation needed for traffic noise.

Figure 5.5 also shows the coefficients calculated for a flat panel of rubber crumb with thickness $d = 20.9$ cm, thus having the same amount of this material per unit length than the measured barrier. These coefficients have

been also obtained by using Eq. (5.3.9), in which the transmission $\mathcal{T}_{SC}$ is replaced by that calculated for a slab made of a dissipative material [Bre80]

$$\mathcal{T}_{RC} = \left| e^{-\gamma d \cos(\theta')} \frac{1-\rho^2}{1-\rho^2 e^{-2\gamma d \cos(\theta')}} \right|^2, \tag{5.5.3}$$

where $\gamma = \alpha + ik$ is the exponential propagation in rubber crumb including attenuation effects and $\rho$ the reflectance between two semi-infinite layers of air and rubber crumb. The angle $\theta'$ is obtained through the Snell's law $ik_0 \sin(\theta) = \gamma \sin(\theta')$, where $k_0$ is the wavenumber in air. Note that the $DL_R$ value of the flat barrier is slightly higher than that for the sonic crystal barrier, but this small difference is clearly compensated with the improvement of flow resistance as well as aesthetic aspects of the sonic crystal barrier.

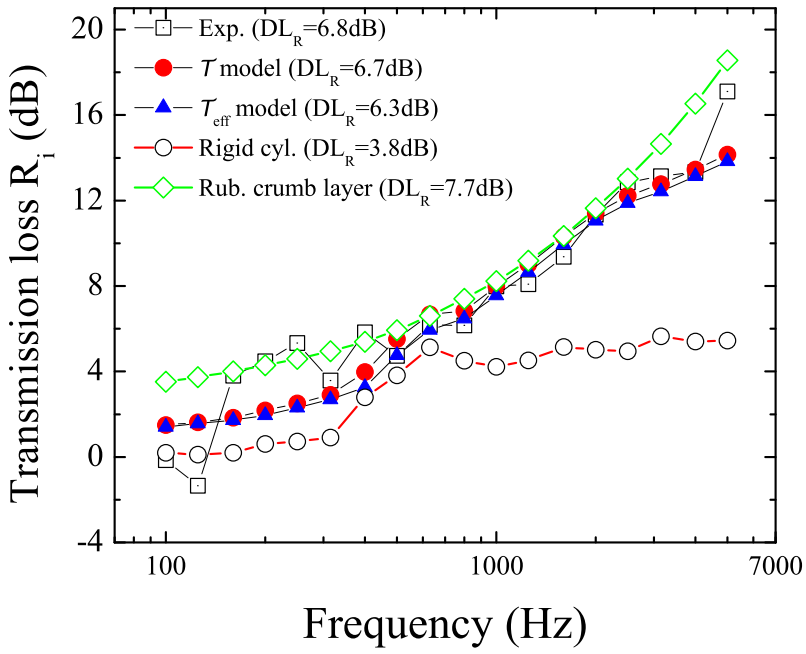


Figure 5.5: (Color online) $R_i$ coefficients and quality factors $DL_R$ (simulated and measured) of the barrier illustrated in Fig. 5.4. Coefficients simulated for a barrier made of only rigid cylinders with the same external radii are also depicted for comparison.

Nevertheless, it is important to mention that the $DL_R$ here achieved is

far from that of an efficient noise barrier. This fact is mainly due to the constraints imposed to the optimization process, especially those applied to the transparent topology. When these requirements are relaxed, more efficient designs can be obtained as observed in the case of the opaque barriers. If a higher attenuation is required while meeting the same constraints, the study of new absorption mechanisms should be considered. Thus the inclusion of additional absorbers into the scattering units can lead to a better performance without requiring too dense structures.

# Part II

# Noise barriers based on microperforated cylinders

# Chapter 6

# Introduction

## 6.1 Microperforated panels

Microperforated panels (MPP) consist of plates with sub-millimeter perforations backed by an air cavity and a rigid wall (see Fig. 6.1). MPPs represent an interesting alternative to the traditional use of fibers and foams, especially in outdoor applications where weathering and fiber quality deterioration are major drawbacks. They are also useful in those applications requiring fibreless materials like ventilation systems where fiber contamination becomes an issue. Unlike bulk absorbers, MPPs are robust in severe environments, cleanable, light weight and non-combustible. Moreover aesthetic aspects can be enhanced since the panels can be built with transparent materials (like methacrylate) or even in decorated or surface-treated plates. The absorption spectrum of MPPs is tunable and can provide better sound absorption at low frequencies than typical fibers and foams.

The absorbing mechanism of a MPP is based on a Helmholtz-type resonance. The energy losses are mainly due to the viscous friction of the saturated fluid in the walls of the perforations, although other secondary effects such as heat transfer or piston-like motion of the perforations may be considered. This inherent damping eliminates the need to use porous or fibrous materials, although these absorbing materials could be placed in the cavity in order to improve the performance of the structure. From the point of view of acoustic impedances, a MPP can be described as the series connection of a resistance and an inductive reactance (corresponding to the equivalent


Figure 6.1: Basic structure of a microperforated panel. It is based on a microperforated plate of thickness $t$ and an air cavity of thickness $D$ backed with a rigid wall.

model of the holes) with a capacitive reactance due to the air cavity. When the system resonates, both reactances cancel each other in such a manner that the characteristic impedance of the panel becomes purely real. Under these circumstances, a high absorption can be obtained provided that the resistance of the plate approaches that of air. It is remarkable that circuit equivalent models have been widely used in many works since it simplifies the calculation of MPPs and allows the analysis of more complex structures based in the same principles.

Ordinary perforated panels (with perforations on the order of millimeter or even centimeters) have been traditionally used as protective facing for sound absorbing materials. They have also been extensively employed as narrowband Helmholtz absorbers for mufflers. Due to the large size of the perforations, they have very low acoustic resistance and therefore their absorption is low except at very narrow bands. MPP absorbers were first proposed by Maa [Maa75]. Maa showed that, by reducing the diameter of the holes to sub-millimeter dimensions, the normal impedance of the panel increases. If the size of the holes is small enough, the real part of the impedance becomes close to the characteristic impedance of air in such a manner that the absorption coefficient will be close to one at the resonant frequencies.

Since the first work of Maa, many other studies have been published in

this topic reporting improvements and more detailed analysis. Maa [Maa87] proposed double resonators made with two parallel MPPs. He demonstrated through electrical equivalent circuits that this configuration broaden the absorption band of the structure. A new variation was introduced by removing the rigid wall of a double MPP, showing that the new structure can enhance the absorption at low frequencies [SMK06]. Since lightweight panels are preferable, Sakagami et al. [SMY05] investigated the effects of vibrations in the perforated plate. They showed that vibrations can affect negatively to the performance of the sound absorber and suggested tuning the optimal values of the design to account for this phenomenon. On the other hand the vibrations in the backing plate were studied by Dupont and coworkers, who demonstrated that the absorptive properties of the MPPs can be improved in some bands with a proper design [DPL03]. Toyoda and Takahashi proposed a partitioned backing cavity [TT08] where each cell creates a local one-dimensional field (even with oblique incidence) which enhance the Helmholtz resonance. This idea allowed them to improve the response of the sound absorber at medium frequencies. Practical works have been also reported, the first real application being published in 1997, when patented microperforated panels were installed in the German Parliament Building in Bonn [FZ97b, FZ97a]. The use of transparent MPPs for window systems was studied by Kang and Brocklesby [KB05], paying attention to the light transmission and the natural ventilation through the plates. More recently Asdrubali and Pispola shown the feasibility of using transparent MPP absorbers in outdoor applications [AP07]. In his work a numerical optimization of a MPP with three layers was applied in order to get the best design according to the criteria of the European normative. The use of MPPs in flow duct applications such as automotive exhaust or ventilation systems has been studied by Allam and Åbom [AÅ11]. They proposed a dissipative silencer based on a microperforated tube surrounded by concentric cavities and demonstrated that this technology can compete with the use of porous materials.

MPPs were initially manufactured with circular perforations, according to the initial proposal by Maa. The plates were drilled through laser cutting techniques, leading to an expensive product that was considered too costly for commercial use. However affordable MPPs are now available due to the

research focused on developing cheap fabrication processes and materials. Instead of circular perforations, slit-shaped holes probed to be an advantageous alternative. They have similar acoustic properties than the holes with circular shape [Maa00] and can be manufactured in plastic or metal by pressing or cutting methods. In addition, Pfretzschner et al. considered the use of textile materials because their structure is inherently microperforated [PCS+06b]. Since the perforation ratio of these materials is too high, the authors proposed to combine them with rigid perforated plates having relatively large perforations and a low perforation ratio. This method resulted in an effective and cheap way to build MPPs and gave rise to a patent application [PCS06a].

## 6.2 Objectives

In previous chapters it was shown that noise barriers made with rubber crumb cylinders provide acceptable levels of attenuation in the medium and high frequency ranges of the traffic noise spectrum. However this proposal is unable to provide effective attenuation mechanisms at low frequencies. The two phenomena involved, absorption by a porous material and a band gap associated with the periodicity of the scatterers, require too large cylinders and high filling fractions when dealing with long wavelengths. Thus, this part of the work presents a study intended to include the technology of MPPs to the SC-based barriers previously proposed. Due to the standard behavior of MPPs it is expected a considerable improvement in the absorptive properties of the barrier, especially in the low frequency range. The new scattering units will be based on microperforated shells, which are obtained by rolling up microperforated plates. It is intended to develop a theoretical model for the new scattering units and demonstrate its validity with an experimental realization. Note that this proposal can be combined with the latter so that scattering units having a microperforated shell and inner porous layers could be considered. An optimization procedure similar to that developed in the last chapter will be performed and the results of adding microperforated plates to the scatterers will be shown and discussed.

# Chapter 7

# Theoretical model of microperforated cylinders

An approach for the calculation of MPPs was presented by Maa in the seventies [Maa75], and it was further improved in 1998 [Maa98]. Maa developed a simplified model to characterize the absorption properties of MPP absorbers having circular-shaped holes. The analysis of the structure was based on acoustic impedance calculations, where the total impedance of a MPP is determined by the impedance of the plates as well as the air cavity. This approach has been employed in the numerical calculations here presented. Thus, the impedance of microperforated plates with circular and slit-shaped geometries are first described in Section 7.1. Some remarks about MPPs will be provided in Section 7.2 when the impedance of the air cavity is taken into consideration. After this the study of a microperforated cylindrical shell can be approached from the impedance of the plate employed in building the scattering unit. Thus the expression of the T matrix of different scatterers containing a microperforated shell is deduced and verified in Section 7.3.

## 7.1 Impedance of a perforation

The impedance of a microperforated plate is calculated as the sum of two contributions: the internal and the external parts. The former accounts for the effects that take place inside the holes and is modelled by considering infinitely long perforations. On the other hand the external part takes into

account the phenomena occurring on the surface of the plate and the openings of the perforations. This term can include other effects like non-linearities or the presence of wind. The external part will be expressed through several corrections that are added to the total impedance. Note that the impedance of a perforation is considered as a lumped element since its size is supposed to be much smaller than the wavelength of the incident sound.

### 7.1.1 Internal part

The internal part is the most significant contribution to the total impedance of the microperforated plate. Its deduction relies on the study of the sound propagation inside infinitely long tubes. The first works in this topic were developed by Rayleigh [Ray45] and Kirchhoff [Kir68]. An approximate simplification of the Rayleigh's theory was presented by Crandall [Cra26], who considered a negligible contribution of the thermal conductivity in tubes whose length is small compared to the wavelength. Under these circumstances a radial-dependent laminar flow along the tube is obtained and the propagation characteristics can be calculated in a cross section of the tube. This simplification was adopted by Maa to deduce the acoustic impedance of small tubes.

When considering friction losses in a fluid, the equation of motion (see Eq. (2.1.5)) needs to account for terms that depend on the dynamic viscosity of the fluid. By considering an incompressible fluid with mass density $\rho_0$ and dynamic viscosity $\eta_0$, the new equation of motion becomes the Navier-Stokes equation

$$-\nabla P + \eta_0 \Delta \vec{v} = \rho_0 \left[ \frac{\partial \vec{v}}{\partial t} + \vec{v}\,(\vec{v} \cdot \nabla) \right], \tag{7.1.1}$$

whose linearized form is

$$-\nabla P + \eta_0 \Delta \vec{v} = \rho_0 \frac{\partial \vec{v}}{\partial t}. \tag{7.1.2}$$

Consider a tube with circular section of radius $r_0$ whose axis is parallel to the coordinate $z$. According to the assumptions of Crandall, the velocity field has only non-zero components in the $z$ direction. Due to the geometry of the problem, it is convenient to express the last equation in cylindrical coordinates

$$-\nabla_z P + \frac{\eta_0}{r} \frac{\partial}{\partial r} \left( r \frac{\partial v_z}{\partial r} \right) = \rho_0 \frac{\partial v_z}{\partial t}. \tag{7.1.3}$$

where $r$ corresponds to the radial coordinate. If a sinusoidal motion is supposed, the time derivatives are replaced by $i\omega$ terms. By rearranging the above equation we obtain

$$\left(\frac{\partial^2}{\partial r^2} + \frac{1}{r}\frac{\partial}{\partial r} + l^2\right) v_z = \frac{1}{\eta_0}\frac{\partial P}{\partial z}, \tag{7.1.4}$$

where

$$l^2 = -\frac{i\omega\rho_0}{\eta_0}. \tag{7.1.5}$$

Taking into account that the velocity vanishes on the surface of the cylinder, the solution to this equation has the form

$$v_z = -\frac{1}{i\omega\rho_0}\frac{\partial P}{\partial z}\left[1 - \frac{J_0(lr)}{J_0(lr_0)}\right], \tag{7.1.6}$$

$J_0$ being the Bessel function of zero order. From this expression the average velocity over a cross section of the tube can be obtained as

$$\overline{v}_z = \frac{2}{r_0^2}\int_0^{r_0} v_z r dr = -\frac{1}{i\omega\rho_0}\frac{\partial P}{\partial z}\left[1 - \frac{2}{s\sqrt{-i}}\frac{J_1(s\sqrt{-i})}{J_0(s\sqrt{-i})}\right], \tag{7.1.7}$$

where the parameter $s$ is defined as

$$s = r_0\sqrt{\frac{\omega\rho_0}{\eta_0}}, \tag{7.1.8}$$

and is known as the perforate constant. Its value is proportional to the ratio of the radius of the tube to the viscous boundary layer thickness. The viscous layer corresponds to the spatial zone close to a surface where viscous phenomena need to be taken into consideration. Navier-Stokes equation has to be applied within this layer. The non-viscous equation of motion could be employed outside since viscosity effects are negligible. Therefore large boundary layers compared to the radius of the cylinders will lead to more viscous dissipation, which is in accordance with the requirement of holes with small radii.

When considering a tube with a finite length $t$, its impedance can be calculated from Eq. (7.1.7) provided that $t$ is much smaller than the wavelength of the sound. In this case the pressure gradient can be approximated by the pressure difference between both tube ends divided by the thickness $t$.

Replacing this gradient in Eq. (7.1.7) the internal impedance of the circular hole has the form

$$Z_{c,i} = i\omega\rho_0 t \left[1 - \frac{2}{s\sqrt{-i}} \frac{J_1(s\sqrt{-i})}{J_0(s\sqrt{-i})}\right]^{-1}. \tag{7.1.9}$$

Consider now a slit-shaped hole along the $z$-axis and whose walls are defined by the planes $x = -a$ and $x = a$. The slit is supposed to be narrow and long, in such a manner that the contributions of its ends (located at $y = \pm b$) are negligible. The velocity field has only z-component and only depends on the coordinate $x$ due to the boundary layer of the walls. Therefore Eq. (7.1.2) reduces to [AA93]

$$-\frac{\partial P}{\partial z} + \eta_0 \frac{\partial^2 v_z}{\partial x^2} = i\omega\rho_0 v_z. \tag{7.1.10}$$

The solution of this equation, taking into account that velocity vanishes at $x = \pm a$, is

$$v_z = -\frac{1}{i\omega\rho_0} \frac{\partial P}{\partial z} \left[1 - \frac{\cos(lx)}{\cos(la)}\right]. \tag{7.1.11}$$

The averaged velocity over a cross section becomes

$$\overline{v}_z = \frac{1}{2a} \int_{-a}^{a} v_z dx = -\frac{1}{i\omega\rho_0} \frac{\partial P}{\partial z} \left(1 - \frac{tanh(s'\sqrt{i})}{s'\sqrt{i}}\right). \tag{7.1.12}$$

The parameter $s'$ corresponds to

$$s' = a\sqrt{\frac{\omega\rho_0}{\eta_0}}, \tag{7.1.13}$$

which is identified as the perforate constant of the slit. Therefore the internal impedance of the slit-shaped hole has the form

$$Z_{s,i} = i\omega\rho_0 t \left[1 - \frac{tanh(s'\sqrt{i})}{s'\sqrt{i}}\right]^{-1}. \tag{7.1.14}$$

### 7.1.2 Viscous end correction

The viscous end correction takes into account the amount of energy dissipated by the panel surface near the hole. It depends on the velocity profile of the fluid particles along the surface, which is difficult to calculate even for simple

geometries. Ingard suggested that this effect can be estimated through the resistance of an oscillatory flow over an infinite plane surface [Ing53]

$$R_S = \frac{1}{2}\sqrt{2\eta_0\omega\rho_0}, \tag{7.1.15}$$

when the radius of curvature is large compared to the viscous boundary layer thickness. However Ingard argued that this value may be in serious error in the case of surfaces with small radii of curvature. In these circumstances the particle velocity over the surface is higher and therefore the dissipation effects are stronger. He demonstrated experimentally that the correction is closer to $4R_S$ in this case. As a general rule, Guo et al. expressed the correction as [GAÅ08]

$$R_S = \alpha\sqrt{2\eta_0\omega\rho_0}, \tag{7.1.16}$$

where $\alpha$ is a factor which equals 4 for circular holes with sharp edges, 2 for rounded edges and 2 for slit-shaped holes. These values are in agreement with those used by Maa in his papers.

### 7.1.3 Mass end correction

Besides the air reactance due to the fluid filling the hole, there is another contribution caused by the air motion outside the hole. This effect is interpreted as an extra mass attachment and is often expressed in the form of an added length $\delta$ to the tube. In the case of a circular hole Crandall [Cra26] and Sivian [Siv35] proposed the Rayleighs expression for the air mass reactance of a vibrating piston

$$\delta = \frac{16r_0}{3\pi}, \tag{7.1.17}$$

which is the value employed by Maa in his models. However this expression ignores the interaction between neighboring holes which in practice reduces the value of $\delta$. Note that this fact can induce to error, especially in large apertures where the end correction is an important contribution. Ingard calculated the mass end correction for different geometries by considering a uniform velocity distribution in the aperture [Ing53]. Assuming that a microperforated panel acts as a distributed Helmholtz resonator, the theory developed by Ingard allows taking into account the neighboring effect. The added length was approximated as

$$\delta = 0.96\sqrt{A}(1 - 1.25\xi), \tag{7.1.18}$$

where $A$ is the area of the aperture and $\xi$ is a factor that must be less than 0.4. In the case of circular holes $\xi = 2\sqrt{\sigma/\pi}$ where $\sigma$ is the perforation ratio, defined as the drilled area divided by the total area of the plate. Note that the above expression becomes Eq. (7.1.17) when $\sigma$ is negligible. In the case of slit-shaped holes $\xi = \sqrt{\sigma}$. If values of $\xi$ greater than 0.4 were used, it would be necessary to use the exact expressions reported by Ingard.

Melling revised the effect of interaction between perforations and presented a function [Mel73]

$$\Psi(\epsilon) = \left( \sum_{n=0}^{\infty} a_n \epsilon^n \right)^{-1}, \tag{7.1.19}$$

with $\epsilon = \sqrt{\sigma}$ and whose first coefficients are $a_{0-8}$=[1, -1.4092, 0, 0.33818, 0, 0.06793, -0.02287, 0.03015, -0.01641]. The corrected length is expressed as $\delta = \delta_0/\Psi(\epsilon)$, where $\delta_0$ is the Rayleigh correction of Eq. (7.1.17). It is worth noting that the correction given by Melling is an approximation of the exact values obtained by Ingard in the full range of $\sigma$ for circular holes.

The mass end correction is added as a series reactance to the hole impedance with the form $X_m = \omega \rho_0 \delta$. Other authors argue that $\delta$ must be added to the length $t$ of the tube in the formula of $Z_i$, thus affecting also to the real part of the internal impedance [SS85, Mel73].

### 7.1.4 Nonlinear effects

The impedance of a hole depends on the intensity of the incident wave. The first evidence of this fact was reported by Sivian, who observed experimentally an increase in the resistance at high particle velocities [Siv35]. The phenomenon is explained by turbulence and jet effects in the region of the aperture, and appears when the sound pressure exceeds levels on the order of 100dB approximately [Maa75]. Ingard and Ising reported measures of nonlinear impedance of circular holes concluding that the opening resistance may be estimated by [II67]

$$R_{nl} = \rho_0 |\vec{v}|, \tag{7.1.20}$$

where $|\vec{v}|$ is the particle velocity amplitude. For high sound pressure levels $R_{nl}$ is the dominant component of the resistive part of the total impedance. On the other hand, non-linear reactance tends to decrease for high intensity

fields. The non-linear reactive part is difficult to calculate. In his work Ingard only concluded that its value reduces to a half of the linear value at high sound levels. For this term Maa proposed a modified mass end correction [Maa98]

$$\delta' = \delta(1 + \frac{|\vec{v}|}{\sigma c_0})^{-1}, \tag{7.1.21}$$

where $c_0$ corresponds to the phase velocity of sound waves in the fluid.

### 7.1.5 Grazing flow effects

A tangential flow on the microperforated plate is referred to as grazing flow. It is shown that the acoustic behaviour of the microperforated panel is modified by the presence of grazing flow, and therefore additional terms need to be added to the total impedance. The real part of the correction is modelled as $\beta M Z_0$ where $M$ is the Mach number, $Z_0$ is the characteristic impedance of air and $\beta$ a constant. This model was initially proposed by Rice, who suggested the value $\beta_c = 0.3$ for ordinary perforated plates [Ric71]. For plates with small perforations Guo and co-workers proved that this value is actually lower, reporting a value of $\beta_c = 0.15$ [GAÅ08]. The case of slit-shaped holes is more complex since the impedance depends on the orientation of the slits with respect to the flow. The same authors found the values $\beta_s = 0.079$ for slits parallel to the flow direction and $\beta_s = 0.044$ for slits perpendicular to it [GAÅ08].

On the other hand the presence of grazing flow decreases the value of reactance in the holes due to the effective reduction of mass attachment in the openings. According to another work of Rice, this effect can be described through a modified mass end correction $\delta_g = \delta/(1 + \chi M^3)$ with $\chi = 305$ [RFA71]. Allam and Åbom found that this value of $\chi$ is much larger for microperforated panels, suggesting $\chi_c = 12.6^3$ for plates with circular perforations [AÅ11].

### 7.1.6 Total impedance

Taking into account all the phenomena described in the previous sections, the total impedance of a circular hole has the form

$$Z_c = i\omega\rho_0 t\left[1-\frac{2}{s\sqrt{-i}}\frac{J_1(s\sqrt{-i})}{J_0(s\sqrt{-i})}\right]^{-1}+\alpha\sqrt{2\eta_0\omega\rho_0}+\rho_0|\vec{v}|+\beta_c M\rho_0 c_0+ i\omega\rho_0\frac{16r_0}{3\pi}\frac{1-1.25\frac{2}{\sqrt{\pi}}\sqrt{\sigma}}{\left(1+\frac{|\vec{v}|}{\sigma c_0}\right)(1+\chi_c M^3)}. \quad (7.1.22)$$

For a slit-shaped hole the total impedance is

$$Z_s = i\omega\rho_0 t\left[1-\frac{tanh(s'\sqrt{i})}{s'\sqrt{i}}\right]^{-1}+2\sqrt{2\eta_0\omega\rho_0}+\rho_0|\vec{v}|+\beta_s M\rho_0 c_0+ 0.96i\omega\rho_0\sqrt{a\,b}\frac{1-1.25\sqrt{\sigma}}{\left(1+\frac{|\vec{v}|}{\sigma c_0}\right)(1+\chi_s M^3)}, \quad (7.1.23)$$

where $2a$ and $2b$ are the width and length of the rectangle which defines the slit, respectively. For simplicity this work supposes a negligible grazing flow and a linear behaviour of the hole impedance. Therefore the expressions used in further analyses are

$$Z_c = i\omega\rho_0 t\left(1-\frac{2}{s\sqrt{-i}}\frac{J_1(s\sqrt{-i})}{J_0(s\sqrt{-i})}\right)^{-1}+\alpha\sqrt{2\eta_0\omega\rho_0}+ i\omega\rho_0\frac{16r_0}{3\pi}\left(1-1.25\frac{2}{\sqrt{\pi}}\sqrt{\sigma}\right), \quad (7.1.24)$$

$$Z_s = i\omega\rho_0 t\left(1-\frac{tanh(s'\sqrt{i})}{s'\sqrt{i}}\right)^{-1}+2\sqrt{2\eta_0\omega\rho_0}+ 0.96i\omega\rho_0\sqrt{a\,b}\left(1-1.25\sqrt{\sigma}\right). \quad (7.1.25)$$

## 7.2 Microperforated panels

In the last section the impedance $Z_{hole}$ of a perforation , which is referred to as $Z_c$ or $Z_s$ depending on the geometry, has been studied. In this analysis a

single hole has been supposed. When an air cavity and a rigid termination are included, the resulting structure consists of a single Helmholtz resonator. A MPP can be though as a 2D distribution of independent Helmholtz resonators. This is a valid assumption when the perforation ratio is small, although it also applies to plates with larger values of $\sigma$ through the inclusion of neighboring corrections in the impedance expression. The effective impedance of the set of Helmholtz resonators is given by the impedance of a single hole divided by the perforation ratio $\sigma$:

$$Z_p = \frac{Z_{hole}}{\sigma} = R_p + i\omega M_p. \tag{7.2.1}$$

On the other hand the impedance of an air cavity of depth $D$ backed by a rigid wall is calculated through a one dimensional model as

$$Z_{back} = \frac{-iZ_0}{tan(k_0 D)}, \tag{7.2.2}$$

where $k_0$ is the wavenumber in air. Thus the total impedance of a MPP at normal incidence is $Z_{MPP} = Z_p + Z_{back}$. The absorption coefficient of the panel is therefore given by

$$\alpha = \frac{4Z_0 R_p}{(Z_0 + R_p)^2 + \left(\omega M_p - \frac{Z_0}{tan(k_0 D))}\right)^2}. \tag{7.2.3}$$

It is worth noting that the reactance of the holes $M_p$ and the impedance of the cavity are of opposite signs. The resonance will occur at the frequency $f_0$ where the imaginary part of $Z_{MPP}$ vanishes, satisfying the equation

$$\omega_0 M_p = \frac{Z_0}{tan(\omega_0 D/c_0))}, \tag{7.2.4}$$

whose solution is located around the frequency where $D$ is one-quarter of the acoustic wavelength. At $f_0$ the absorption coefficient reaches its maximum value

$$\alpha_0 = \frac{4Z_0 R_p}{(Z_0 + R_p)^2}. \tag{7.2.5}$$

which results in total absorption when $R_p = Z_0$. It is shown that the absorption spectrum can be tuned to targeted frequency bands by adjusting the cavity depth. On the other hand it is also remarkable that the MPP absorber

is not effective in other frequency bands. To illustrate this behavior, Fig. 7.1 represents the absorption coefficient as a function of the frequency and the cavity depth of a MPP built with the microperforated plates employed in the experimental characterization of the next chapter. It is observed a good performance at low frequencies where strong absorption bands appear between narrow bands with low absorption. At high frequencies this trend is reversed and the low absorption bands dominate the spectrum of the MPP, making the structure inefficient as sound absorber.

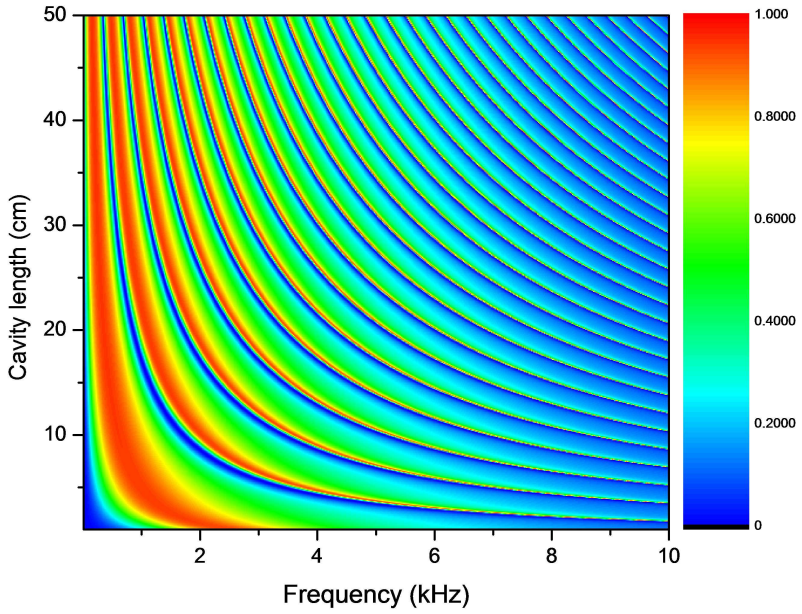


Figure 7.1: Absorption spectrum of a MPP as a function of the frequency and the cavity depth. The MPP has slit shaped holes with parameters $b = 1.61$ mm, $a = 48.1$ $\mu$m, $\sigma = 3.3\%$ and $t = 1$ mm.

The absorption coefficient of a MPP depends on the angle of incidence of the impinging sound. In the case of oblique incidence the expression of $Z_p$ does not change since the holes behave as a locally reacting material. The air inside the pores vibrates along its axis and this vibration only depends on the pressure of air above the pore. At the other side of the plate (inside

the cavity) the impinging wave will travel with the same oblique angle of incidence $\theta$ following the Huygens'Principle. The impedance of the air cavity changes according to the expression

$$Z_{back} = \frac{-iZ_0}{\cos(\theta)} \frac{1}{tan(k_0 D \cos(\theta))}. \tag{7.2.6}$$

and therefore the sound absorption coefficient becomes

$$\alpha(\theta) = \frac{4Z_0 R_p \cos(\theta)}{(Z_0 + R_p \cos(\theta))^2 + \left(\omega M_p \cos(\theta) - \frac{Z_0}{tan(k_0 D \cos(\theta)))}\right)^2}. \tag{7.2.7}$$

The new resonance frequency is now $f_0' = f_0/\cos(\theta)$, higher than that found at normal incidence. The maximum absorption can be greater or smaller than the values obtained with normal incidence depending on $\theta$ and $R_p$.

## 7.3 T matrix of microperforated cylinders

A microperforated cylindrical shell is easily constructed by rolling up a microperforated plate. The T matrix of this scattering unit will be here calculated as a function of the impedance of the plate $Z_p$ in such a manner that different effects (such as wind or non linearities) could be easily introduced in the model through impedance corrections. First, the T matrix of a single microperforated shell will be deduced. Note that microperforated plates provide good sound absorption at low frequencies although they are not so efficient in the high frequency range. In order to improve the high frequency operation of the scattering units it is interesting to include an absorbing cylinder inside the microperforated shell. Thus the T matrix of a cylindrical shell with a porous core will be later considered, as well as the insertion of a second microperforated shell.

### 7.3.1 Hollow microperforated cylinder

Consider a thin microperforated shell between the radii $R^+$ and $R^-$, in such a manner that $R^+ - R^- = t$. The medium inside the shell is referred to as medium $A$ and is characterized by the acoustic parameters $\rho_a$ and $k_a$. The

medium $B$ is located outside the shell and its parameters are $\rho_b$ and $k_b$. The acoustic field in both media can be expressed in cylindrical coordinates as

$$P_a(r,\theta) = \sum_{q=-\infty}^{+\infty} A_q^0 J_q(k_a r) e^{iq\theta}, \quad (r < R^-), \tag{7.3.1}$$

$$P_b(r,\theta) = \sum_{q=-\infty}^{+\infty} B_q^0 J_q(k_b r) e^{iq\theta} + \sum_{q=-\infty}^{+\infty} B_q H_q(k_b r) e^{iq\theta}, \quad (r > R^+). \tag{7.3.2}$$

It will be useful to express the radial velocity of the above fields to apply the boundary conditions. According to Eq. (2.1.6), the radial velocity equals to

$$v_r = \frac{-i}{\omega\rho}\frac{\partial P}{\partial r}, \tag{7.3.3}$$

and therefore

$$v_{ra}(r,\theta) = \sum_{q=-\infty}^{+\infty} \frac{-ik_a}{\omega\rho_a} A_q^0 J_q'(k_a r) e^{iq\theta}, \tag{7.3.4}$$

$$v_{rb}(r,\theta) = \sum_{q=-\infty}^{+\infty} \frac{-ik_b}{\omega\rho_b} \left(B_q^0 J_q'(k_b r) + B_q H_q'(k_b r)\right) e^{iq\theta}. \tag{7.3.5}$$

The first boundary condition imposes the continuity of the normal velocities at each side of the perforated plate. These velocities correspond to $v_{ra}$ and $v_{rb}$ and could be interpreted as the velocities given by Eqs. (7.1.7) and (7.1.12) averaged by the perforation ratio $\sigma$. Hence

$$\sum_{q=-\infty}^{+\infty} \frac{k_b}{\rho_b} \left(B_q^0 J_q'(k_b R^+) + B_q H_q'(k_b R^+)\right) e^{iq\theta} = \sum_{q=-\infty}^{+\infty} \frac{k_a}{\rho_a} A_q^0 J_q'(k_a R^-) e^{iq\theta}. \tag{7.3.6}$$

Multiplying by $e^{is\theta}$ and integrating from 0 to $2\pi$ the above equation yields

$$\frac{k_b}{\rho_b} \left(B_q^0 J_q'(k_b R^+) + B_q H_q'(k_b R^+)\right) = \frac{k_a}{\rho_a} A_q^0 J_q'(k_a R^-). \tag{7.3.7}$$

The second boundary condition relates the pressure difference between both sides of the plate and the normal velocity through the plate impedance $Z_p$, leading to

$$v_{ra}|_{r=R^-} = v_{rb}|_{r=R^+} = \frac{P_b|_{r=R^+} - P_a|_{r=R^-}}{Z_p}. \tag{7.3.8}$$

When applying the above condition to the proposed acoustic fields we obtain

$$\frac{-iZ_p k_a}{\omega\rho_a} A_q^0 J_q'(k_a R^-) = B_q^0 J_q(k_b R^+) + B_q H_q(k_b R^+) - A_q^0 J_q(k_a R^-). \quad (7.3.9)$$

Combining Eqs. (7.3.7) and (7.3.9) the T matrix of a microperforated shell is shown to be

$$T_q = \frac{B_q}{B_q^0} = -\frac{\rho_q J_q'(k_b R^+) - J_q(k_b R^+)}{\rho_q H_q'(k_b R^+) - H_q(k_b R^+)}, \quad (7.3.10)$$

where

$$\rho_q = \frac{\rho_a k_b}{\rho_b k_a} \frac{J_q(k_a R^-)}{J_q'(k_a R^-)} - \frac{iZ_p k_b}{\omega\rho_b}. \quad (7.3.11)$$

### 7.3.2 Microperforated cylinder with porous core

Consider the structure shown in Fig. 7.2, where the medium $A$ is an absorbing material with porosity $\Omega$ and the microperforated shell is defined by the radii $R^+$ and $R^-$. The acoustic fields in each region are expressed as

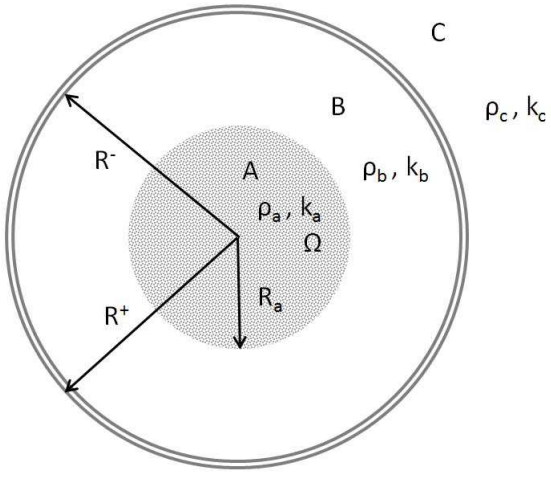


Figure 7.2: Structure of a microperforated shell ($R^- < r < R^+$) with a porous core ($r < R_a$). The acoustic parameters are indicated in each layer.

$$P_a(r,\theta) = \sum_{q=-\infty}^{+\infty} A_q^0 J_q(k_a r) e^{iq\theta}, \quad (r < R_a), \tag{7.3.12}$$

$$P_b(r,\theta) = \sum_{q=-\infty}^{+\infty} B_q^0 J_q(k_b r) e^{iq\theta} + \sum_{q=-\infty}^{+\infty} B_q H_q(k_b r) e^{iq\theta}, \quad (R_a < r < R^-), \tag{7.3.13}$$

$$P_c(r,\theta) = \sum_{q=-\infty}^{+\infty} C_q^0 J_q(k_c r) e^{iq\theta} + \sum_{q=-\infty}^{+\infty} C_q H_q(k_c r) e^{iq\theta}, \quad (r > R^+). \tag{7.3.14}$$

The boundary conditions at the $B-C$ interface are the same as those presented in last section, those are

$$v_{rb}|_{r=R^-} = v_{rc}|_{r=R^+} = \frac{P_c|_{r=R^+} - P_b|_{r=R^-}}{Z_p}. \tag{7.3.15}$$

By applying the conditions to $P_b$ and $P_c$ we get

$$\frac{k_c}{\rho_c}\left(C_q^0 J_q'(k_c R^+) + C_q H_q'(k_c R^+)\right) = \frac{k_b}{\rho_b}\left(B_q^0 J_q'(k_b R^-) + B_q H_q'(k_b R^-)\right), \tag{7.3.16a}$$

$$\frac{-iZ_p k_c}{\omega\rho_c}\left(C_q^0 J_q'(k_c R^+) + C_q H_q'(k_c R^+)\right) = C_q^0 J_q(k_c R^+) - B_q^0 J_q(k_b R^-) - B_q H_q(k_b R^-). \tag{7.3.16b}$$

On the other hand the boundary conditions at the $A-B$ interface are

$$P_a|_{r=R_a} = P_b|_{r=R_a}, \tag{7.3.17a}$$

$$\frac{1}{\rho_b}\left.\frac{\partial P_b}{\partial r}\right|_{r=R_a} = \frac{\Omega}{\rho_a}\left.\frac{\partial P_a}{\partial r}\right|_{r=R_a}, \tag{7.3.17b}$$

from which the subsequent expressions are derived:

$$B_q^0 J_q(k_b R_a) + B_q H_q(k_b R_a) = A_q^0 J_q(k_a R_a), \tag{7.3.18a}$$

$$\frac{k_b}{\rho_b}\left(B_q^0 J_q'(k_b R_a) + B_q H_q'(k_b R_a)\right) = \frac{\Omega k_a}{\rho_a} A_q^0 J_q'(k_a R_a). \tag{7.3.18b}$$

Taking into account the above expressions, the T matrix of a microperforated shell with porous core is expressed as

$$T_q = \frac{C_q}{C_q^0} = -\frac{\rho_q J_q'(k_c R^+) - J_q(k_c R^+)}{\rho_q H_q'(k_c R^+) - H_q(k_c R^+)}, \tag{7.3.19}$$

where

$$\rho_q = \frac{\rho_b k_c}{\rho_c k_b} \frac{J_q(k_b R^-) + T_q^s H_q(k_b R^-)}{J_q'(k_b R^-) + T_q^s H_q'(k_b R^-)} - \frac{i Z_p k_c}{\omega \rho_c}. \tag{7.3.20}$$

The parameter $T_q^s$ has the form

$$T_q^s = \frac{B_q}{B_q^0} = -\frac{\rho_q^s J_q'(k_b R_a) - J_q(k_b R_a)}{\rho_q^s H_q'(k_b R_a) - H_q(k_b R_a)}, \tag{7.3.21}$$

with

$$\rho_q^s = \frac{1}{\Omega} \frac{\rho_a k_b}{\rho_b k_a} \frac{J_q(k_a R_a)}{J_q'(k_a R_a)}. \tag{7.3.22}$$

$T_q^s$ coincides with the T matrix of a porous cylinder, as previously explained in Section 2.2.1. Moreover, if the porous core is replaced by a rigid cylinder, Eq. (7.3.19) is valid while $T_q^s$ becomes

$$T_q^s = -\frac{J_q'(k_b R_a)}{H_q'(k_b R_a)}. \tag{7.3.23}$$

### 7.3.3 Cylinder with two perforated shells

A second microperforated shell can be placed inside the external one in an effort to enhance the absorption of the scattering unit. Consider the scheme shown in Fig. 7.3, where a new perforated layer with impedance $Z_{pa}$ has been introduced in the region $R_a^- < r < R_a^+$. On the other hand the external microperforated layer is located at $R_b^- < r < R_b^+$, and its impedance is denoted as $Z_{pb}$. Because of their similarity, the expressions of the pressure fields in this case has the same form than Eqs. (7.3.12) to (7.3.14). By applying boundary conditions at the interface B-C we get

$$\begin{aligned} \frac{k_c}{\rho_c}\left(C_q^0 J_q'(k_c R_b^+) + C_q H_q'(k_c R_b^+)\right) = \\ \frac{k_b}{\rho_b}\left(B_q^0 J_q'(k_b R_b^-) + B_q H_q'(k_b R_b^-)\right), \end{aligned} \tag{7.3.24a}$$

$$\begin{aligned} \frac{-i Z_{pb} k_c}{\omega \rho_c}\left(C_q^0 J_q'(k_c R_b^+) + C_q H_q'(k_c R_b^+)\right) = C_q^0 J_q(k_c R_b^+) + \\ C_q H_q(k_c R_b^+) - B_q^0 J_q(k_b R_b^-) - B_q H_q(k_b R_b^-). \end{aligned} \tag{7.3.24b}$$

Similarly to the previous case, the T matrix has the form

$$T_q = \frac{C_q}{C_q^0} = -\frac{\rho_q J_q'(k_c R_b^+) - J_q(k_c R_b^+)}{\rho_q H_q'(k_c R_b^+) - H_q(k_c R_b^+)}, \tag{7.3.25}$$

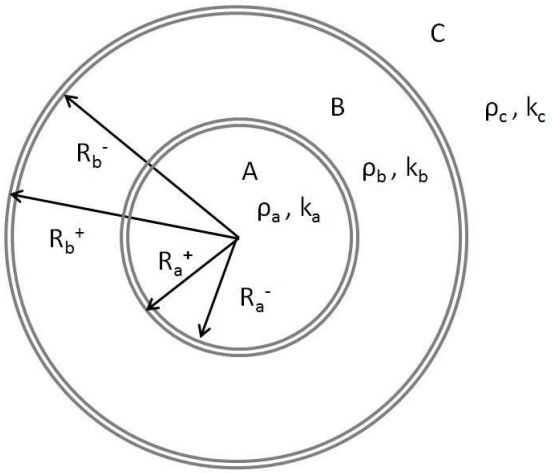


Figure 7.3: Structure of a microperforated shell ($R_b^- < r < R_b^+$) with an additional microperforated core ($R_a^- < r < R_a^+$). The acoustic parameters are indicated in each layer.

where

$$\rho_q = \frac{\rho_b k_c}{\rho_c k_b} \frac{J_q(k_b R_b^-) + T_q^s H_q(k_b R_b^-)}{J_q'(k_b R_b^-) + T_q^s H_q'(k_b R_b^-)} - \frac{i Z_{pb} k_c}{\omega \rho_c}. \tag{7.3.26}$$

$T_q^s$ is defined as the relation between $B_q$ and $B_q^0$ coefficients. Its calculation is similar to the deduction provided in Section 7.3.1. Therefore its expression can be derived from Eq. (7.3.10) as

$$T_q^s = \frac{B_q}{B_q^0} = -\frac{\rho_q^s J_q'(k_b R_a^+) - J_q(k_b R_a^+)}{\rho_q^s H_q'(k_b R_a^+) - H_q(k_b R_a^+)}, \tag{7.3.27}$$

with

$$\rho_q^s = \frac{\rho_a k_b}{\rho_b k_a} \frac{J_q(k_a R_a^-)}{J_q'(k_a R_a^-)} - \frac{i Z_{pa} k_b}{\omega \rho_b}. \tag{7.3.28}$$

### 7.3.4 Numerical verification

In order to check numerically the presented theory, finite element simulations have been performed for a 3D scatterer. It consists of a cylindrical perforated shell with radius $R^+ = 4$ cm and a plate thickness of $t = 0.5$ mm. The holes have a radius of $r = 0.25$ mm and are separated by a distance $b = 1.25$ mm. The height of the shell is set to $h = b\sqrt{3}/2$. The structure is supposed to

be infinitely height since periodic conditions are configured in the top and bottom boundaries. This scheme results in a perforated surface where the holes are arranged in a rectangular pattern whose perforation ratio is

$$\sigma = \pi \frac{r^2}{bh} = \frac{2\pi}{\sqrt{3}} \left(\frac{r}{b}\right)^2 = 14.51\%. \tag{7.3.29}$$

The computation of the problem through the Navier-Stokes equation requires finding the velocity field instead of the pressure. This involves solving three scalar equations (one for each velocity component), increasing the computational complexity. In addition more elements need to be added in order to fully describe the viscous boundary layer. It results in a high number of elements, especially when considering a 3D simulation. Because of this, viscosity has been disregarded and the simulation has been carried out by applying the acoustic Helmholtz equation given in Eq. (2.1.20). In this limit Eq. (7.1.24) becomes

$$Z_c = i\omega\rho_0 \left[ t + \frac{16 r_0}{3\pi} \left( 1 - 1.25 \frac{2}{\sqrt{\pi}} \sqrt{\sigma} \right) \right], \tag{7.3.30}$$

in such a manner that the holes are purely inductive. Note that the above equation is approximately valid for large holes whose radii are much larger than the boundary layer thickness.

The problem has been solved by using the commercially available software Comsol Multiphysics. The geometry of the 3D model is shown in Fig. 7.4 and consists of a perforated shell embedded in a cylindrical cavity. The T matrix of the perforated scatterer has been obtained through the procedure explained in Apendix A and the results are directly compared with the data calculated from Eq. (7.3.10). Figures 7.5 and 7.6 show the real and imaginary parts of the three first orders of the T matrix in a frequency range from 100 Hz to 6 kHz. It is found a good agreement between the numerical simulations and the theoretical approach, thus proving the validity of the developed expressions.

### 7.3.5 Experimental verification

The acoustic transparency of a sample composed of three rows of hollow cylinders made with perforated plates was described in Chapter 4. This

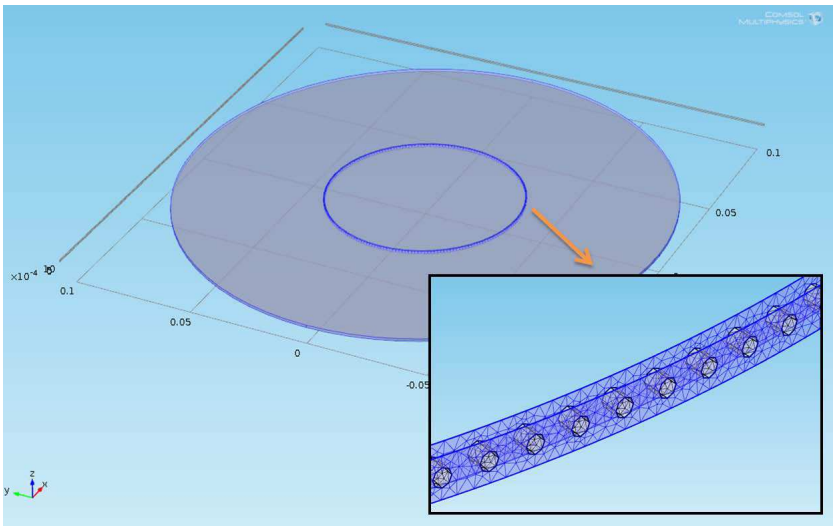


Figure 7.4: Finite element simulation of a perforated shell with radius $R^+ = 4$ cm, thickness $t = 0.5$ mm, radius of the perforations $r = 0.25$ mm and perforation ratio $\sigma = 14.51\%$. The figure shows the whole simulation domain required for the calculation of the T matrix (see Apendix A). A zoom of the perforated shell is illustrated in the inset.

property was experimentally demonstrated, although a theoretical approach was not provided. The model developed in the previous sections has been here applied to calculate the response of that sample. The perforated cylinders have a thickness of $t = 0.5$ mm and a radius of 4 cm. The perforations have a radius of $r = 250$ $\mu$m and they are arranged with a triangular pattern whose separation between holes is $b = 1.25$ mm. The perforation ratio is therefore

$$\sigma = \frac{2\pi}{\sqrt{3}} \left(\frac{r}{b}\right)^2 = 14.51\%. \tag{7.3.31}$$

Note that theses cylinders are equivalent to those simulated in the last section, despite the fact of having different patterns in the distribution of holes. Figure 7.7 is a copy of Fig. 4.6 where the theoretical results have been included. The transmission of the flat plate at normal incidence (Fig. 7.7(a)) has been calculated from the plate impedance $Z_p$ and the characteristic impedance of air $Z_0$ as

$$T_p = \frac{2Z_0}{2Z_0 + Z_p}. \tag{7.3.32}$$

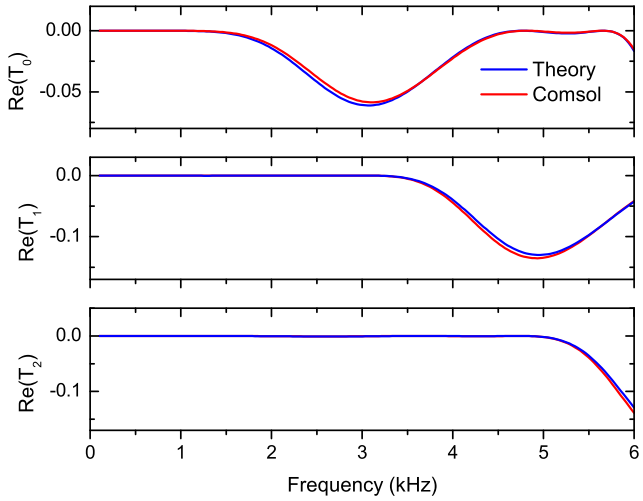


Figure 7.5: Real part of the T matrix of the cylinder shown in Fig. 7.4 for $q = 0, 1, 2$. Red lines are obtained through finite element simulations and blue lines correspond to the theoretical model developed in Section 7.3.1.

It is obtained a theoretical transmission close to unity which is in good agreement with the experiments and proves the acoustical transparency of the flat perforated plates. On the other hand the transmission of the SC structure (Fig. 7.7(b)) has been computed for a sample with three infinite rows of perforated cylinders by using the T matrix expressed in Eq. (7.3.10) and the impedance model shown in Eq. (7.1.24). The transmission of this slab is slightly lower than the values found for a flat plate. It is remarkable the presence of a minimum at approximately 3 kHz, coinciding with the transmission reduction experimentally observed. The good agreement between experimental and theoretical data gives support to the reported model. Note that the frequency at which the minimum occurs is close to the diffraction limit of the crystal, where the wavelength of the impinging wave equals the lattice constant. The observed phenomenon is the result of a Wood anomaly related to the excitation of modes that travels along the axis of the structure. To understand the underlying physics, this effect will be comprehensively analyzed in Chapter 10.

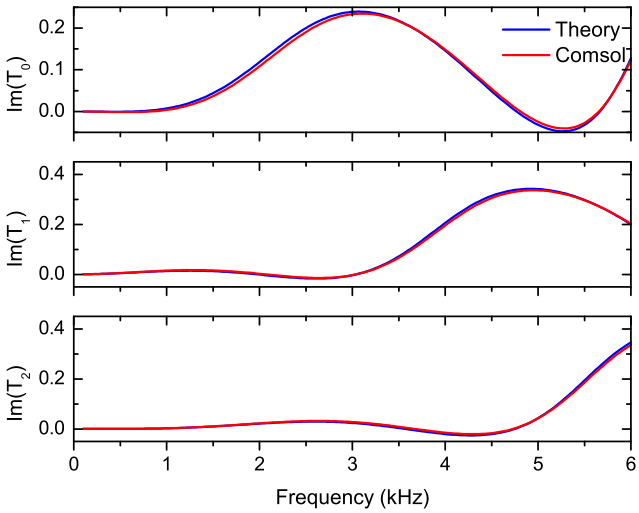


Figure 7.6: Imaginary part of the T matrix of the cylinder shown in Fig. 7.4 for $q = 0, 1, 2$. Red lines are obtained through finite element simulations and blue lines correspond to the theoretical model developed in Section 7.3.1.

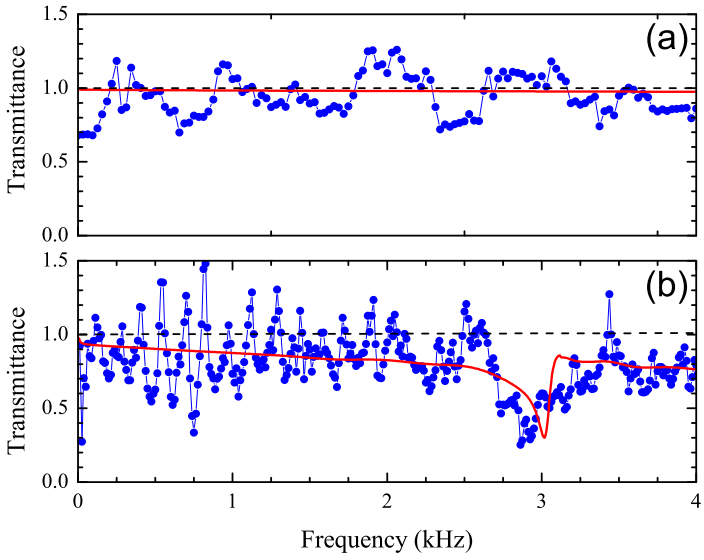


Figure 7.7: (a) Measured (blue dots) and calculated (red line) transmittance of a flat perforated plate with a thickness of 0.5 mm. The perforations are circular with diameter 0.5 mm and are arranged in a hexagonal lattice. (b) Measured (blue dots) and calculated (red line) transmittance of a SC structure consisting of three rows of cylinders with 8 cm of diameter fabricated with the perforated plates characterized above. The dashed horizontal lines are guides for the eye.

# Chapter 8

# Experimental characterization

A noise barrier prototype has been built in order to check the theory developed in the last chapter and observe the advantages of using microperforated cylinders. First, the geometry of the samples and the microperforated plates employed in building them are introduced and analysed. Then the measurement setup is described and an improved procedure to characterize sonic crystal-based samples is presented. The experimental results are shown and compared with the theoretical predictions. A discussion about the relevant findings is finally provided.

## 8.1 Experimental setup

### 8.1.1 Samples

The measured samples consist of slabs based on a square distribution of scatterers with different numbers of rows. Each row has 30 cylinders with a height of 3 m and an external radius of 8 cm. Considering a maximum of three rows and a lattice parameter of 22 cm, the maximum dimensions of the samples are $6.54 \times 0.6 \times 3$ m$^3$. The barrier samples have been placed in an outdoor environment. A photograph of the structure is shown in Fig. 8.1.

The cylinders are made by rolling up microperforated plates manufactured by the company Sontech. A porous core with radius 4 cm filled with rubber crumb is considered to be included inside the microperforated shells. For this purpose perforated cylinders have been built as containers. Figure

Figure 8.1: Sample made with 3 rows of microperforated 3 m-high cylinders.

8.2 shows the appearance of a cylinder with a porous core, whose scheme is in accordance with Fig. 7.2 provided that the perforated shells are acoustically transparent.

The perforated cylinders that contains the rubber crumb have holes with a diameter of 3 mm and a perforation ratio of 32.6%. The thickness of the steel plates is 1 mm. Figure 8.3 shows numerical calculations of a slab with three rows of these hollow perforated cylinders arranged in the same way as the measured samples. The slab shows a transmission spectrum with a high transparency and therefore the structure will allow the sound to interact with the rubber crumb contained therein. It is also observed the presence of very narrow peaks associated with the excitation of Wood anomalies, as explained in Chapter 10. Note that, since the perforation ratio is too high, the expression derived by Melling for the mass end correction [see Eq. (7.1.19)] has been used instead of its approximate form given by Ingard [Eq. (7.1.18)].

The microperforated plates are made with 1 mm-thickness aluminum plates. Instead of being drilled, the perforations are performed by a punching method. This process deforms slightly the surface of the plate, resulting in

Figure 8.2: Detail of a microperforated shell with radius 8 cm and a porous core of radius 4 cm filled with rubber crumb.

a complex pore geometry (see details in Fig. 8.4). However regarding the shape of the apertures it is found that they can be approached by a slit, according to previous works performed with similar plates [GAÅ08, AÅ11]. The parameters of the equivalent slit have been obtained by measuring the sound absorption of the sample shown in Fig. 8.4 in an impedance tube. The experimental results and the corresponding fitted curves are represented in Figs. 8.5 and 8.6 for different cavity depths between the sample and a rigid backing. The expression used for the impedance of the microperforated apertures corresponds to Eq. (7.1.25) and the absorption coefficient is then obtained by following Eq. (7.2.3). It is found a good agreement between theoretical and measured curves, validating the slit-based approach for the actual perforations. The effective slit has a half-length $b = 1.61$ mm and a half-width $a = 48.1$ $\mu$m. The perforation ratio is $\sigma = 3.3\%$ and the nominal thickness of the plate $t = 1$ mm has been assumed.

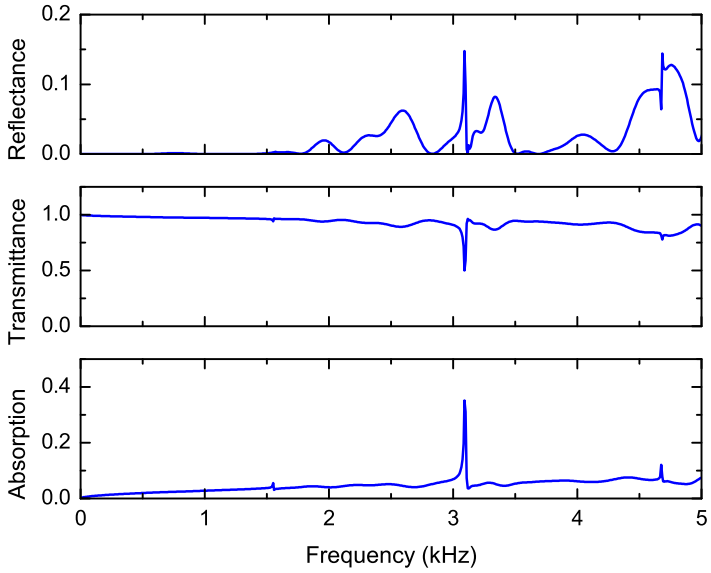


Figure 8.3: Reflectance, transmittance and absorption spectrum of 3 rows of perforated shells with radius 4 cm and thickness 1 mm, arranged in a square lattice with lattice constant 22 cm. The holes have a radius of 3mm and the perforation ratio is 32.6%.

### 8.1.2 Measurement method

The measurement method presented in Section 4.1 is fast and relatively easy to carry out. Nevertheless it is unable to provide reliable data at frequencies higher than the diffraction limit of the structure. This issue is especially severe in large structures where the diffraction limit is located at low frequencies. Even when measuring data below the diffraction limit, some errors can be induced by the presence of evanescent modes if the microphone is placed too close to the sample. Because of this, a new measurement method is proposed in this chapter.

Consider a sonic crystal made with several rows, each row having infinite cylinders. As shown in Chapter 2, when a plane wave impinges on the slab, the pressure field can be expressed as an infinite sum of plane waves. These waves are propagating or evanescent depending on the frequency of the impinging sound. If an incident field with an undetermined amplitude $A_0$ is

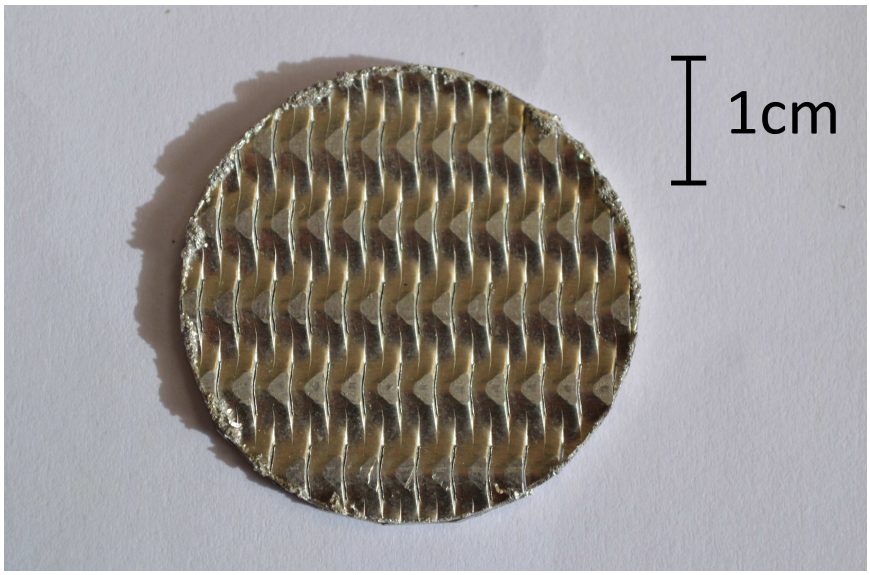


Figure 8.4: Sample of the microperforated plate use in building the scattering units. The surface has an irregular profile due to the fabrication process, although the apertures can be approached as slit-shaped holes. The results of the experimental characterization as well as the effective parameters of the equivalent holes are shown in Figs. 8.5 and 8.6.

supposed, the total pressure field given by Eq. (2.4.16) becomes

$$P(r,\theta) = A_0 e^{i\vec{k_0}\cdot\vec{r}} + \sum_{\nu=-\infty}^{+\infty} C_\nu^{\pm} e^{i\vec{k_\nu^{\pm}}\cdot\vec{r}}. \tag{8.1.1}$$

Knowing the amplitudes $C_\nu^{\pm}$ of the modes, reflectance and transmittance spectra are calculated by applying the normalized amplitudes $C_\nu^{\pm}/A_0$ to Eqs. (2.4.22) and (2.4.24). To fully characterize these spectra it is necessary to measure at least all the propagating modes at each frequency. In addition some of the first evanescent modes can be considered to take into account their slight influence on the measured pressure field. This fact involves acquiring the pressure at as many spatial points as the number of modes taken into account plus one (note that the incident field amplitude $A_0$ is also unknown). Consider a set of $M+1$ points at positions $\vec{r_m}$ with $m = 0, 1, ...M$, all of them being located in the same side of the SC than the impinging wave. The complex pressure measured at each point $\vec{r_m}$ is denoted as $P_m$.

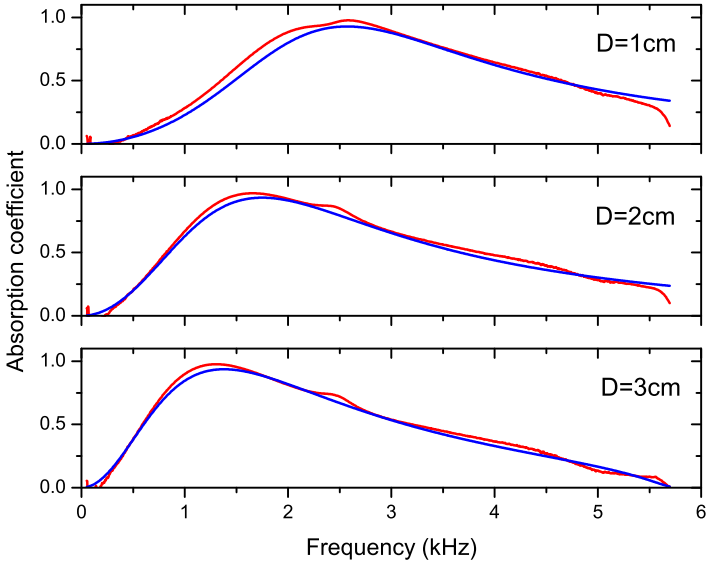


Figure 8.5: Absorption coefficient measured (red line) and theoretically fitted (blue line) of the microperforated sample shown in Fig. 8.4 with cavity depths of $D = 1, 2, 3$ cm. The best fit is achieved for $t = 1$ mm, $a = 48.1$ $\mu$m, $b = 1.61$ mm and $\sigma = 3.3\%$ in Eq. (7.1.25).

According to Eq. (8.1.1) the contribution of each reflected mode is

$$P_\nu^-(r,\theta) = C_\nu^- e^{i\vec{k_\nu^-}\cdot\vec{r}}, \tag{8.1.2}$$

where the propagation constant is obtained by taking the negative sign of Eq. (2.4.11). Considering the influence of $N+1$ reflected modes, their amplitudes are obtained by solving the linear system

$$\begin{bmatrix} e^{i\vec{k_0}\cdot\vec{r}_0} & e^{i\vec{k_0^-}\cdot\vec{r}_0} & \dots & e^{i\vec{k_N^-}\cdot\vec{r}_0} \\ e^{i\vec{k_0}\cdot\vec{r}_1} & e^{i\vec{k_0^-}\cdot\vec{r}_1} & \dots & e^{i\vec{k_N^-}\cdot\vec{r}_1} \\ \vdots & \vdots & \ddots & \\ e^{i\vec{k_0}\cdot\vec{r}_M} & e^{i\vec{k_0^-}\cdot\vec{r}_M} & \dots & e^{i\vec{k_N^-}\cdot\vec{r}_M} \end{bmatrix} \begin{bmatrix} A_0 \\ C_0^- \\ \vdots \\ C_N^- \end{bmatrix} = \begin{bmatrix} P_0 \\ P_1 \\ \vdots \\ P_M \end{bmatrix} \tag{8.1.3}$$

With regard to the transmitted wave, consider another set of $M'$ points located at positions $\vec{r_m}'$ in the other side of the SC and the pressure measured on them $P'_m$. The amplitude of $N'+1$ transmitted modes is obtained through

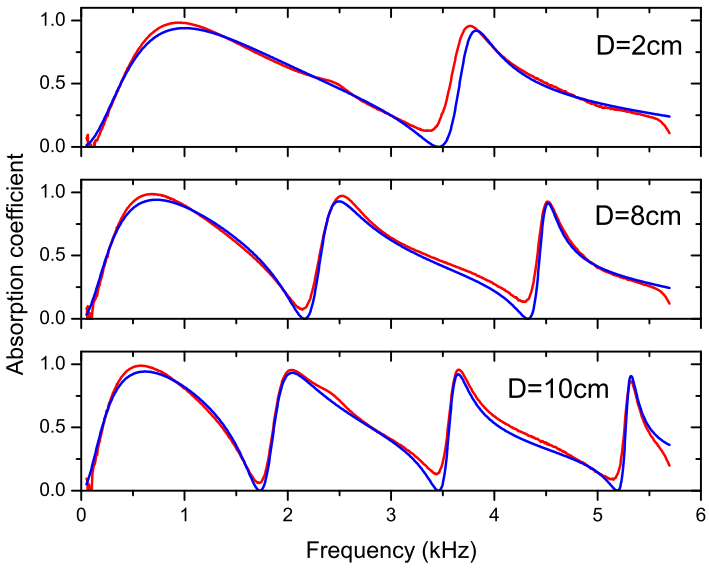


Figure 8.6: Absorption coefficient measured (red line) and theoretically fitted (blue line) of the microperforated sample shown in Fig. 8.4 with cavity depths of $D = 5, 8, 10$ cm. The best fit is achieved for $t = 1$ mm, $a = 48.1$ $\mu$m, $b = 1.61$ mm and $\sigma = 3.3\%$ in Eq. (7.1.25).

the system

$$\begin{bmatrix} e^{i\vec{k_0}\cdot\vec{r_0}'} & e^{i\vec{k}_1^+\cdot\vec{r_0}'} & \cdots & e^{i\vec{k}_{N'}^+\cdot\vec{r_0}'} \\ e^{i\vec{k_0}\cdot\vec{r_1}'} & e^{i\vec{k}_1^+\cdot\vec{r_1}'} & \cdots & e^{i\vec{k}_{N'}^+\cdot\vec{r_1}'} \\ \vdots & \vdots & \ddots & \\ e^{i\vec{k_0}\cdot\vec{r_M}'} & e^{i\vec{k}_1^+\cdot\vec{r_M}'} & \cdots & e^{i\vec{k}_{N'}^+\cdot\vec{r_M}'} \end{bmatrix} \begin{bmatrix} A_0 + C_0^+ \\ C_1^+ \\ \vdots \\ C_{N'}^+ \end{bmatrix} = \begin{bmatrix} P_0' \\ P_1' \\ \vdots \\ P_M' \end{bmatrix} \tag{8.1.4}$$

Note that $A_0$ must be known for the calculation of the first coefficient of transmittance. This parameter will be obtained from the reflectance measurement. When $M = N + 1$ and $M' = N'$ both systems have a unique solution. In practice $M$ and $M'$ are chosen much greater than $N$ and $N'$, i.e., the field is measured at many more points than needed. The equation systems become overdetermined and they are solved by using the method of least squares. This procedure provides good immunity to random noise. Moreover it is worth noting that it is not practical to consider too many evanescent modes since their exponentials terms are close to zero. Under

these circumstances columns with very low values may appear in the matrices and the systems become ill-conditioned. The computations presented in this work have been performed by assuming a maximum number of 10 modes. Since this number of modes is too high at low frequencies, a lower value is automatically selected when the condition numbers of the matrices are above a threshold. This ensures the stability of the calculations.

To check the proposed method, a numerical simulation of a slab with three rows arranged in a square configuration has been performed. Each row has nine rigid cylinders with 2 cm of radius separated by a lattice constant of 11 cm. These parameters match with those of sample 1 in Chapter 4. The total pressure field has been computed in a grid of 20 points at each side of the structure. The separation between points of the grid is 1 cm. For this test the maximum number of computable modes has been constrained to 6. Figure 8.7 shows a comparison between the results of the new method and the data obtained with the procedure employed in Chapter 4. The theoretical response of the infinite extension of the array (where each row has infinite cylinders) is also included. The improvement of the new measurement procedure is remarkable, especially at high frequencies where the previous method takes unphysical values.

### 8.1.3 Experimental setup

The acquisition of the pressure field at multiple points is performed by a 2D positioning system which moves a microphone B&K 4958 on a defined grid. The sweep area starts in front of the central cylinder of the structure and ends in front of the next cylinder, thus covering a lattice parameter with a spatial resolution of 2 cm. In the perpendicular direction to the axis of the slab, the sweep starts at 5 cm from the face of the cylinder (13 cm from its center) and covers a distance of 4 cm with a step of 1 cm. The sweep is carried out at the two sides of the sample. A scheme of the sweep area is represented in Fig. 8.8 for clarity purposes.

A column speaker UDE AC-150 was employed as excitation source. It was located at 7 meters from the sample and aligned with the central cylinder. The high distance between the sample and the speaker as well as the acquisition of data at half-height of the cylinders and very close to their faces

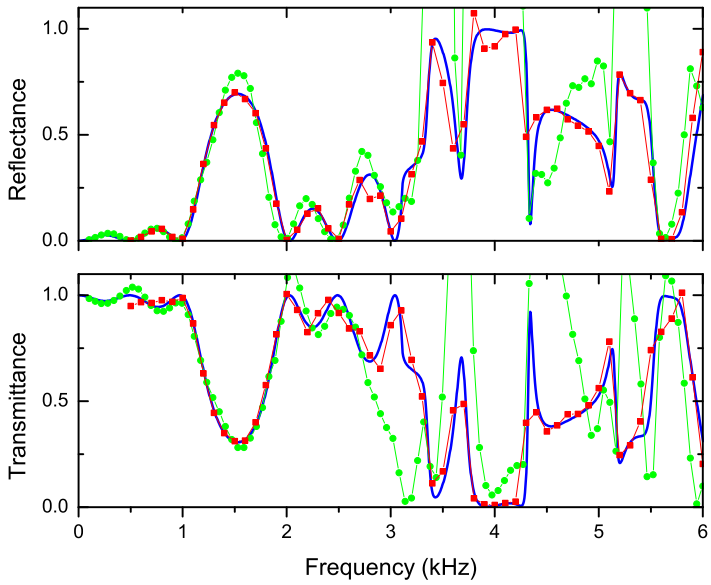


Figure 8.7: Reflectance and transmission spectra of 3 rows with 9 rigid cylinders with radius 2 cm and lattice constant 11 cm. Green dots correspond to a simulation of the measurement method presented in Chapter 4. Red squares are obtained through the new procedure applied on a grid of 20 points at each side of the sample. The theoretical spectra calculated for an infinitely extended slab with 3 rows (blue lines) are included for comparison purposes.

(where diffraction and edge effects are minimized) results in an experimental system whose response approximates that of a plane wave impinging on an slab with infinite cylinders in each row. The sample has been built in a garden close to the Electronic Engineering Department of the Polytechnic University of Valencia. This environment presents several drawbacks, being the most important of them the undesired reflections produced by the surrounding buildings. To avoid this effect, a pulsed excitation technique has been employed, in such a manner that echoes are avoided by acquiring the signals until the arrival time of the first reflection. However is difficult to cover a wide spectrum by emitting short-time signals since the energy must be distributed over the whole range of frequencies, leading to a poor signal to noise ratio. For this reason a narrow band signal which concentrates its

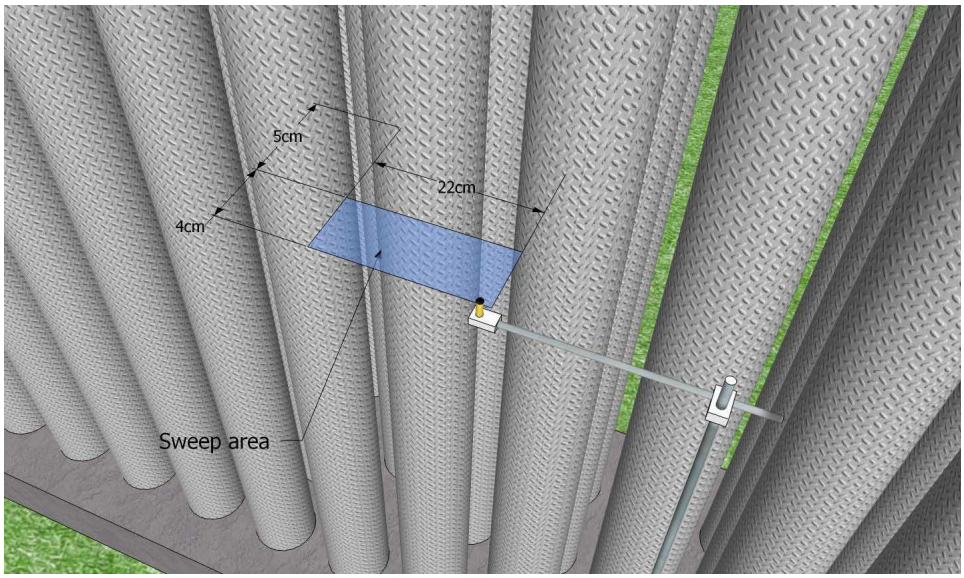


Figure 8.8: Location and size of the area where the pressure field is measured. Note that a similar area is measured at the other side of the barrier.

energy in a specific frequency is here employed. Thus the full spectrum will be measured by performing a frequency sweep. At each step a short pulse is emitted and the acquired signals are processed to obtain the specific value of the corresponding frequency. This task is performed at each point of the spatial sweep during the procedure. The signal processing involves a Fourier transform from which the amplitude and phase of the signal are obtained. In order to avoid sudden increases in the signal driving the speaker, a Gaussian pulse was selected as envelope of the excitation. Modulating the envelope with a carrier of frequency $f_c$ the excitation signal becomes

$$x(t) = Ae^{-\left(\frac{t}{\sigma}\right)^2} \sin(2\pi f_c t), \tag{8.1.5}$$

whose spectrum is

$$X(f) = \frac{Ae^{-2\pi^2(f-f_c)^2\sigma^2}}{\sigma\sqrt{2\pi}}, \tag{8.1.6}$$

which consists of a Gaussian function centered at $f_c$. The bandwidth at 3dB is given by

$$f_{BW} = \sqrt{\frac{ln(2)}{\pi^2\sigma^2}}. \tag{8.1.7}$$

The bandwidth and consequently the duration of the pulse are tunable by the parameter $\sigma$. The value of $\sigma$ in the experiments was fixed to obtain a bandwidth $f_{BW} = 100$ Hz. The described excitation is generated by a NI PCI-6731 card, while data acquisition is performed with a Pico Scope 3224 digitizer. All the processes, including robot motion and signal processing, are managed by a custom Labview program.

## 8.2 Results

Several configurations have been measured in the frequency range from 100 to 5000 Hz with increments of 100 Hz. They are described in Table 8.1. First, a slab with three rows of hollow microperforated shells referred to as sample 1 was characterized. The measured reflectance, transmittance and absorption spectra are shown in Fig. 8.9 along with the theoretical predictions. Numerical calculations have been performed by using the T matrix given by Eq. (7.3.10) for a sample with 3 rows containing infinite microperforated cylinders. Reflection and transmission are obtained through Eqs. (2.4.22) and (2.4.24), while absorption is computed by assuming energy conservation as $\mathcal{A} = 1 - \mathcal{T} - \mathcal{R}$. The agreement between theory and experiment is remarkable, especially when considering the practical drawbacks of outdoor measurements. The most noticeable feature of Fig. 8.9 is the high absorption spectrum at low frequencies, which would not be achievable with classical absorbing materials having the same dimensions. At higher frequencies the absorption is slightly degraded, according to the standard behavior of the microperforated panels. In addition, not clear evidence of an acoustic band gap is found in the reflectance spectrum due to the high absorption of the microperforated units. This response should be expected around 780 Hz, where the lattice parameter equals one-half wavelength.

Scattering units with a porous core made with rubber crumb were then measured. The structure was characterized for 1, 2 and 3 rows of cylinders, referenced as samples 2, 3 and 4, respectively (see Table 8.1). The experimental and theoretical results are represented in Figs. 8.10, 8.11 and 8.12. The numerical calculations have been performed by using the T matrix expressed in Eq. (7.3.19). A good agreement is again found between theory and experiments and a high absorption profile is also found at low frequencies. It

Table 8.1: Dimensions of the cylindrical units used in building the barrier samples studied. The external diameter of the cylindrical microperforated shells is 16 cm in all cases and $d_a$ is the diameter of its inner core, which is filled with rubber crumb. The column *Rows* gives the number of rows of the structure, which can vary between 1 and 3.

| | $d_a$(cm) | *Rows* |
|---|---|---|
| sample 1 | 0 | 3 |
| sample 2 | 8 | 1 |
| sample 3 | 8 | 2 |
| sample 4 | 8 | 3 |

increases with the number of layers in the sample as intuitively expected. For the case of samples 3 and 4 a small peak appears in the reflectance spectrum at the frequency where the band gap is expected. This effect can be related to Bragg reflection since the inner cores filled with rubber crumb increase the reflectivity of the cylinders. Anyway the amplitude of such peaks is reduced as a consequence of the high absorption of the samples. Sample 2 does not present this feature since a band gap is hardly defined by a single line of scatterers. Despite this detail, it is shown that the reflectance spectrum is barely modified by the number of layers. Note that in all the measures non unphysical values are generally found, even at frequencies much greater than the diffraction limit which is located around 1500 Hz. This fact and the good agreement between the model and the experiments validate the measurement method proposed.

## 8.3 Discussion

Figure 8.13 represents the theoretical and measured attenuation of the different samples, calculated as the inverse of the transmission coefficient. For the sake of comparison the insertion loss of a solid wall (black dashed lines) having the same dimensions as the thickest samples (3 m high and 0.6 m thick) is included in the figure. It has been calculated by applying the expressions given in the norm ISO9613 [ISO96] and assuming a microphone located at 1 m from the rear face of the sample. It is remarkable the high attenuation

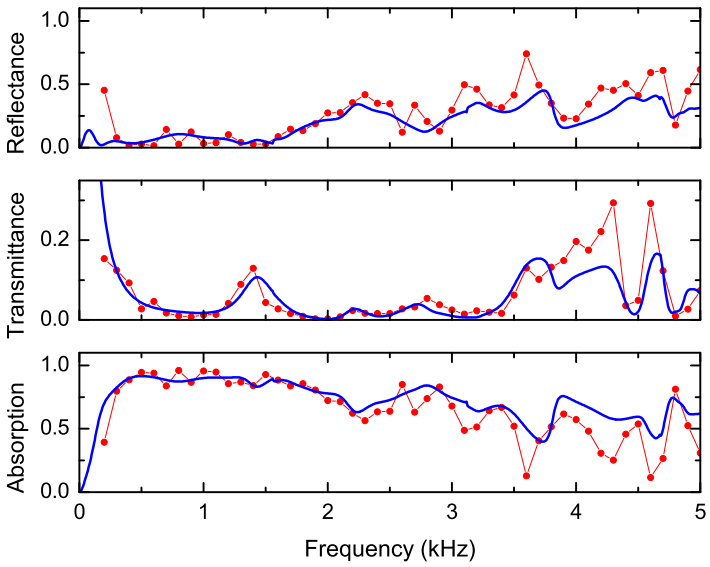


Figure 8.9: Theoretical (blue lines) and experimental (red dots) spectra of reflectance, transmittance and absorption of a sample made with microperforated shells of radius 8 cm. The sample is arranged in a square lattice with 3 rows of 30 cylinders separated by 22 cm (sample 1 in Table 8.1).

at low frequencies of the two samples with 3 rows, which compete with the solid wall and even exceed its attenuation levels in some frequency ranges. Moreover the microperforated samples present the advantage of having an absorptive spectrum, instead of a reflective behavior which does not dissipate the incident acoustic energy. The attenuation of the samples is reduced at high frequencies, although its values remain relatively high (around 10 dB for samples 1 and 4). In the high frequency region the differences between samples 1 and 4 are not significant, showing that rubber crumb has not much effect on the attenuation of the structure. This fact is due to the low fraction of sound that reaches the interior of the microperforated shells. Note that the impedance of a microperforated plate is inductive, so its imaginary part increases with frequency. Except at the frequency where the inductance resonates with the backing cavity, the plate impedance is highly mismatched to that of air in the high frequency region. Therefore sound does not penetrate into the cylinders and rubber crumb does not work properly. This problem

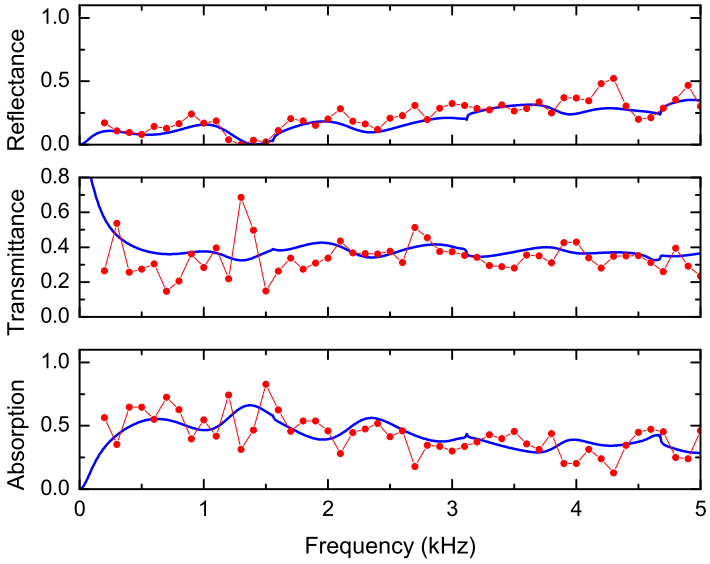


Figure 8.10: Theoretical (blue lines) and experimental (red dots) spectra of reflectance, transmittance and absorption of a sample made with microperforated shells of radius 8 cm and an inner core with radius 4 cm filled with rubber crumb. The sample has 1 row of 30 cylinders separated by 22 cm (sample 2 in Table 8.1).

can be solved by using plates whose impedance has a lower inductive part, that is, plates having smaller perforations.

An interesting comparison is given in Fig. 8.14, where the absorption of sample 1 is compared with the absorption of several flat MPPs with cavity depths of 5, 10 and 20 cm. Figure 8.14(a) shows the absorption at normal incidence. It is observed that the absorption of sample 1 is generally higher than that of the flat panel. This is due to the fact that flat panels are resonant systems and they alternate peaks and valleys on their response, as shown in the last chapter. When considering microperforated cylinders, sound impinges at multiple angles as a consequence of the shape of the scatterers and the multiple scattering events. This occurs even at normal incidence and the attenuation spectrum is smoothed as a result. When a diffuse incident field is applied, the responses of the flat panels are also smoothed. Figure 8.14(b) shows a comparison for this case, where the absorption coefficients have been

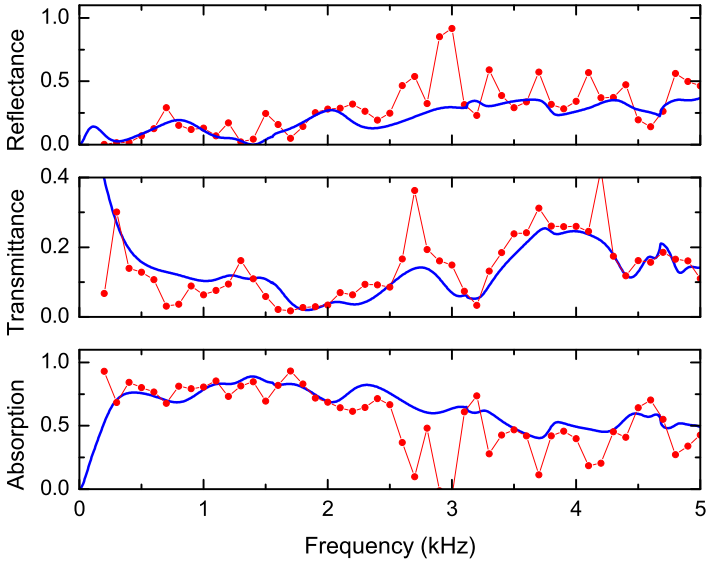


Figure 8.11: Theoretical (blue lines) and experimental (red dots) spectra of reflectance, transmittance and absorption of a sample made with microperforated shells of radius 8 cm and an inner core with radius 4 cm filled with rubber crumb. The sample is arranged in a square lattice with 2 rows of 30 cylinders separated by 22 cm (sample 3 in Table 8.1).

calculated by applying the angle averaging shown in Section 5.3

$$\mathcal{A}_{av}(\omega) = \frac{\int_0^{\pi/2} e^{-\theta^2} \mathcal{A}_{SC}(\omega, \theta) \sin(2\theta)\, d\theta}{\int_0^{\pi/2} e^{-\theta^2} \sin(2\theta)\, d\theta}. \tag{8.3.1}$$

The absorption of sample 1 remains being generally higher than the flat panels, although the differences are reduced. It is concluded that the barrier made with cylinders provide slightly better absorption than the flat panels. Nevertheless it is worth noting that each meter of barrier requires a larger surface of microperforated plates, although in exchange it has the advantage of being visually transparent and having less resistance to wind.

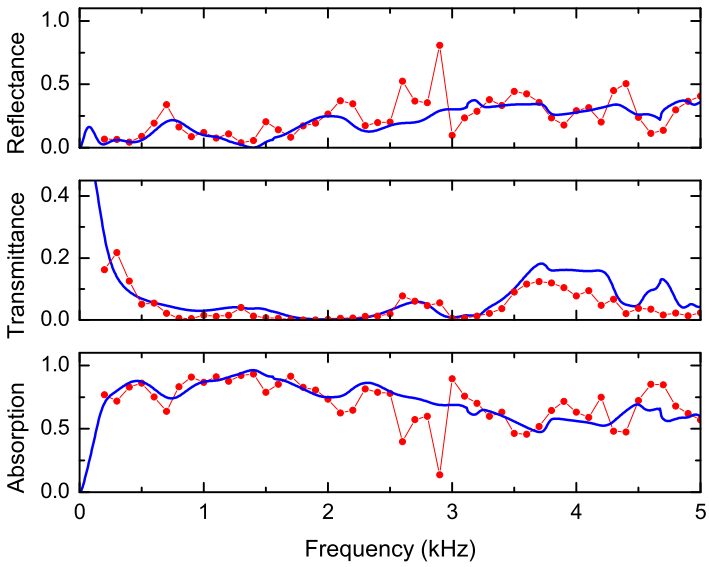


Figure 8.12: Theoretical (blue lines) and experimental (red dots) spectra of reflectance, transmittance and absorption of a sample made with microperforated shells of radius 8 cm and an inner core with radius 4 cm filled with rubber crumb. The sample is arranged in a square lattice with 3 rows of 30 cylinders separated by 22 cm (sample 4 in Table 8.1).

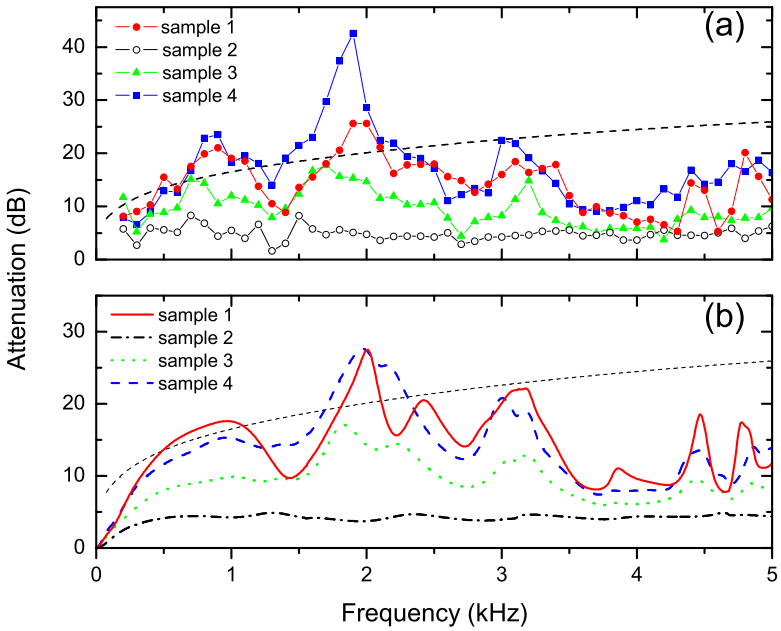


Figure 8.13: Experimental (a) and theoretical (b) attenuation spectra of the different samples described in Table 8.1. Attenuation is calculated in dB as $-10log(\mathcal{T})$, where $\mathcal{T}$ is the simulated or measured transmittance. The dashed lines correspond to the insertion loss predicted for a rigid wall having the same dimensions as the samples.

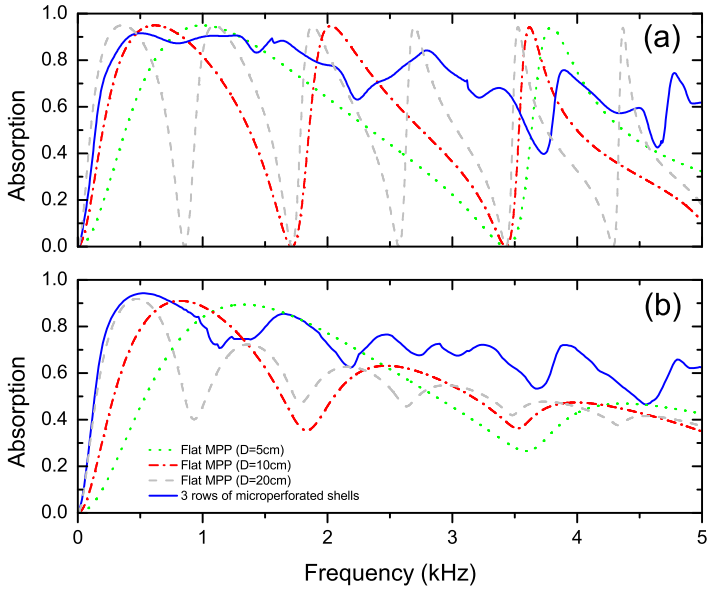


Figure 8.14: Absorption spectra of sample 1 in Table 8.1 (solid line) compared to flat microperforated panels with cavity depths of 5 cm (dotted line), 10 cm (dash-dotted line) and 20 cm (dashed line). The data is shown for normal incidence (a) and a diffuse field (b).

# Chapter 9

# Optimum barrier design

In the last chapters it was deduced and experimentally verified a theory describing the behavior of cylinders made with microperforated shells. The next step is to apply this theory to obtain barriers designed for a specific application, which in this case is the attenuation of traffic noise. However, as explained in Chapter 5, a direct theoretical design is unapproachable due to the complexity of the equations which govern the system. Because of this, a design procedure has been performed by using an optimization algorithm. First, the different barrier topologies will be explained along with the parameters involved in the optimization process. Then the geometry and attenuation of the relevant resulting barriers will be shown and discussed. In addition, a brief remark about the optimization of the parameters concerning the perforations of the plates will be provided.

## 9.1 Optimization model

In Chapter 5 it was presented a multiple reflection model that accounts for the reflected waves from two hypothetical barriers located at both sides of a road. As concluded, the models based on multiple reflections with attenuation by factors $1/r$ and $1/r^2$ (namely $\mathcal{T}'_{\mathit{eff}}$ and $\mathcal{T}''_{\mathit{eff}}$, respectively) are an intermediate case between the transmission through a single barrier ($\mathcal{T}$) and the multiple reflection model without attenuation due to wave propagation ($\mathcal{T}_{\mathit{eff}}$). Because of this, only these last two cases will be here analyzed. It is expected that differences between both models are lower than those found in Chapter 5 since

the scattering units built with microperforated shells are mainly absorptive, reflectance playing a less important role.

The theoretical model employed in this set of optimizations is the same as presented in Chapter 5. As a reminder, the objective function is the $DL_R$ parameter, which is defined as [EN 97]

$$DL_R = -10\log_{10}\left|\frac{\sum_{i=1}^{18} 10^{-0.1R_i}10^{0.1L_i}}{\sum_{i=1}^{18} 10^{0.1L_i}}\right|, \tag{9.1.1}$$

where $L_i$ is the normalized traffic spectrum and $R_i$ the sound transmission loss, both being distributed in third octave bands between 100 Hz and 5000 Hz. According to the norm ISO140-3 [ISO10], $R_i$ coefficients are obtained by measuring the sample with a diffuse incident field. This requires an angular averaging of the transmission coefficient of the barrier, that is, [KIKK00]

$$\mathcal{T}_{av} = \frac{\int_0^{\pi/2} e^{-\theta^2}\mathcal{T}_{SC}(\omega,\theta)\sin(2\theta)d\theta}{\int_0^{\pi/2} e^{-\theta^2}\sin(2\theta)d\theta}, \tag{9.1.2}$$

where $\mathcal{T}_{SC}$ is the transmittance of a single barrier calculated through Eq. (2.4.24) or the effective transmission defined in Eq. (5.2.1). Thus, the $R_i$ coefficients can be approached as the mean of $1/\mathcal{T}_{av}$ in each third octave band.

The barrier geometry here considered is the same as in Fig. 5.2. The structure contains three rows of scatterers, the separation between them being $d_1$ and $d_2$. The cylinders of the same row are identical and they are separated by a distance $D$. They have an external radii $r_1$, $r_2$, $r_3$ and internal cores with radii $r_{i1}$, $r_{i2}$, $r_{i3}$. The centers of the cylinders are aligned, allowing an observer to see between both sides of the barrier. This topology will be referred to as transparent barrier. On the other hand if the cylinders of the second row are displaced half lattice parameter, an opaque configuration is achieved. These two schemes will allow comparing the two extreme cases of an open structure and a compact barrier. In the first case a low wind resistance and high visual transparency are ensured, while much higher losses are expected in the second one.

The system geometry is defined by nine parameters which results in a nine-dimensional objective function. It has been optimized through a constrained nonlinear algorithm based on the simplex method. To globalize the

search several initial parameters have been configured for each execution of the algorithm, trying to exclude results which have converged to local maximums of the objective function. Geometrical constraints have been imposed in order to avoid unphysical results such as those derived from overlapping cylinders. In addition, practical constraints have been also considered. The main of them is the maximum radius of the cylinders which is set to 10 cm. Moreover the maximum width of the barrier is limited to 1 m. For the case of the transparent barrier a distance $D$ at least four times the radius of the largest cylinder is fixed. On the other hand, the only restriction for the opaque barrier will be a minimum distance between cylinders of 1 cm. These settings match with those employed in Chapter 5. When the optimization procedure starts from different initial parameters, it sometimes converges to different solutions having close values of $DL_R$. In these cases the maximum $DL_R$ is not directly taken but the cheaper barrier is considered. This means that, for differences in $DL_R$ lower than 0.5 dB, it is selected the structure with less volume of material.

Different scattering units have been considered for the optimization process. The different topologies are summarized in Fig. 9.1. Thus, samples of type $A$ consists of three rows of microperforated shells. Samples $B$ and $C$ have three rows of shells with an additional core made with a rigid material or rubber crumb, respectively. In the case of $D$-type samples, a second microperforated shell is employed as inner core of the scattering units. Samples $E_n$ (with $n$ from 1 to 6) also have three rows and consist on the six possible combinations of rows having either rubber crumb cylinders or microperforated shells. In all cases, the microperforated shells are supposed to be made with the plates presented in Section 8.1. The T matrix of the cylinders of the topology $A$ are calculated through Eq. (7.3.10). For samples of type $B$ and $C$ Eq. (7.3.19) is employed, where the expression of $T_{qs}$ is given by Eq. (7.3.21) for $C$-type samples and Eq. (7.3.23) for the $B$-type. In the case of samples $D$, whose cylinders have two concentric microperforated shells, Eqs. (7.3.25)-(7.3.28) have been considered. Finally, the T matrix of the rubber crumb cylinders of samples $E_n$ has been calculated through Eq. (2.2.24) and the effective parameters provided in Chapter 3.

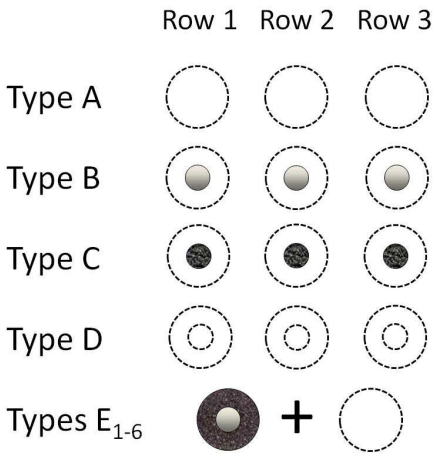


Figure 9.1: Scheme of the microperforated units employed in each of the three rows considered in the optimization procedure. The last case (samples $E_{1-6}$) summarize the six possible combinations of rows made with rubber crumb and microperforated shells.

## 9.2 Results

Coinciding with the results obtained in Chapter 5, the algorithm tends to optimum samples having the maximum allowed radius of the cylinders. There is also a tendency to compact the structure by setting the minimum distance $D$ between the cylinders of the same row. In general terms, the $DL_R$ of all the opaque barriers exceed 20 dB for both transmission models, overcoming the levels obtained in Chapter 5. It is worth noting that those barriers with rigid or rubber crumb inner cores ($B$ and $C$-types) result in values of $DL_R$ similar to the optimization of hollow shells. In some cases they have a slightly higher attenuation than the $A$-type, although this improvement is not considered because it is lower than 0.5 dB and the inclusion of the inner cores is not cost-effective. In other cases the inner cores seem to be unnecessary since their radii converge to a negligible value. This fact is in agreement with the conclusions of the experimental study performed in the last chapter, where the effect of the inner cores made with rubber crumb proved to be ineffective. Because of these reasons, topologies B and C have been discarded from the analysis. The same applies to samples $E_n$ where

lower values of $DL_R$ are generally obtained with respect to $A$-type samples, especially when there are two rows of rubber crumb cylinders. The only topology showing a remarkable improvement is given by samples of type $D$. However the cost increase derived from the inclusion of an additional microperforated shell should be here considered.

The geometric parameters of the optimum barriers of types $A$ and $D$ are shown in Table 9.1 for the transparent ($\square$) and opaque ($\triangle$) configurations and the transmission models $\mathcal{T}$ and $\mathcal{T}_{\mathit{eff}}$. The maximum $DL_R$ is obtained for the opaque topology of the type $D$. Its value is 24.0 dB and falls within the limit of the $B_3$ class ($DL_R > 24$ dB), which is the highest quality category defined by the normative [EN 97]. The samples of type $D$ have converged to the same result for the two transmission models. The resulting barriers are based on a compact structure with cylinders of the maximum allowed radius and inner shells very close to the outer ones. This fact confirms that reflectance cannot be used as the main attenuation mechanisms when dealing with microperforated scattering units. In the case of samples of type $A$, the maximum $DL_R$ achieved is 22.4 dB. The main difference with the previous cases is the convergence to the maximum thickness allowed, i. e., $r_1 + r_3 + d_1 + d_2 = 1m$. Anyway the difference in $DL_R$ with the compacted structures (obtained by reducing $d_1$ and $d_2$) is low, so narrower barriers can be considered when the available space is reduced.

With regard to the transparent topology, the values of $DL_R$ are obviously much lower. Anyway an improvement with respect to barriers based on rubber crumb cylinders is here achieved. It is obtained a maximum $DL_R$ of 8.7 dB, which is a reasonable value when considering the low filling fraction of the barrier. In all cases the minimum distance between cylinders of the same row is obtained, as well as the maximum width of the barrier. Unlike the opaque topology, in the transparent $D$-type samples the radii of the inner cores have converged towards one half of the external radius, approximately.

To illustrate the behavior of the optimized samples, the attenuation spectra of the samples $A$ and $D$ with opaque configurations and calculated through the $\mathcal{T}$ model are shown in Fig. 9.2 for a normally incident plane wave. The response of sample 1 from Chapter 8 (see Table 8.1) has been also included for comparison purposes. The differences between the optimized designs and this reference barrier are obvious. The transmission levels have

Table 9.1: Geometric parameters of the optimum barriers found for the topologies $A$ and $D$ (see Fig. 9.1) with opaque ($\triangle$ symbols) and transparent ($\square$) configurations. The optimizations have been performed by assuming a single barrier ($\mathcal{T}$ model) and two parallel barriers ($\mathcal{T}_{\mathit{eff}}$ model). The quality factor $DL_r$ is expressed in $dB$ and the remaining parameters are in $cm$.

| | Type A | | | | Type D | | | |
|---|---|---|---|---|---|---|---|---|
| | $\mathcal{T}$ | | $\mathcal{T}_{\mathit{eff}}$ | | $\mathcal{T}$ | | $\mathcal{T}_{\mathit{eff}}$ | |
| | $\triangle$ | $\square$ | $\triangle$ | $\square$ | $\triangle$ | $\square$ | $\triangle$ | $\square$ |
| $r_1$ | 10.0 | 10.0 | 10.0 | 10.0 | 10.0 | 10.0 | 10.0 | 10.0 |
| $r_{i1}$ | - | - | - | - | 9.7 | 4.9 | 9.7 | 5.2 |
| $r_2$ | 10.0 | 10.0 | 10.0 | 10.0 | 10.0 | 10.0 | 10.0 | 10.0 |
| $r_{i2}$ | - | - | - | - | 9.7 | 4.8 | 9.7 | 4.4 |
| $r_3$ | 10.0 | 10.0 | 10.0 | 10.0 | 10.0 | 10.0 | 10.0 | 10.0 |
| $r_{i3}$ | - | - | - | - | 9.7 | 4.8 | 9.7 | 5.0 |
| $D$ | 21.0 | 40.0 | 21.0 | 40.0 | 21.0 | 40.0 | 21.0 | 40.0 |
| $d_1$ | 34.2 | 49.7 | 62.3 | 30.9 | 18.2 | 28.8 | 18.2 | 30.7 |
| $d_2$ | 45.8 | 30.3 | 17.8 | 48.8 | 18.2 | 51.2 | 18.2 | 49.3 |
| $DL_R$ | 22.4 | 8.4 | 20.3 | 7.9 | 24.0 | 8.7 | 22.9 | 8.3 |

been greatly improved, especially at low frequencies. Two concentric shells prove to be more efficient at low frequencies than a single shell, reversing this trend at high frequencies. Due to the distribution and weights assigned to the third octave bands in the EN1793 norm, the behavior of cylinders with two concentric shells results in a higher $DL_R$. It is remarkable that both responses presents a local minimum at 1 kHz where the normative assigns the maximum weight. This minimum is found around frequencies associated with high symmetry points of the structure when considering the periodicity given by the lattice parameter $D$ ($c_0/a = 1559$ Hz for sample 1 having a square lattice and $c_0/\sqrt{3}a = 943$ Hz for a triangular lattice with $a = 21$ cm). The convergence of the optimization algorithm can be understood by paying attention to the third octave bands and their weights $L_i$ around 1 kHz. The three colored bands of Fig. 9.2 correspond to the third octave bands having the maximum weights ($L_i = -9, -8, -9$ dB, respectively). Although the central band is not optimally attenuated, the two adjacent bands have a high attenuation. Their weight are not much lower than that assigned to the band centered at 1 kHz, so the solution obtained by the optimization algorithm is found to be efficient.

## 9.3 Optimization of the perforations

Apart from the geometrical parameters defining the sonic crystal lattice and the scattering units, noise barriers based on microperforated shells can be optimized through a proper design of the perforations. This implies not only the dimensions of the pores, but also the perforation ratio and the thickness of the plate. The inclusion of the perforation parameters in the design process involves adding three new parameters to the optimization tool. This extends the search space to twelve dimensions. However, the optimization of the hole parameters requires having in practice the technical means to build custom microperforated plates, which is not a common situation. Because of this, the search of optimized structures taking into account the parameters of the microperforated plates is out of the scope of this work.

In order to briefly illustrate the effect of the hole parameters in the quality of a noise barrier, Fig. 9.3 shows the $DL_R$ over a parametric sweep on the perforation ratio $\sigma$ and the radius of the perforations $r$. The sample consid-

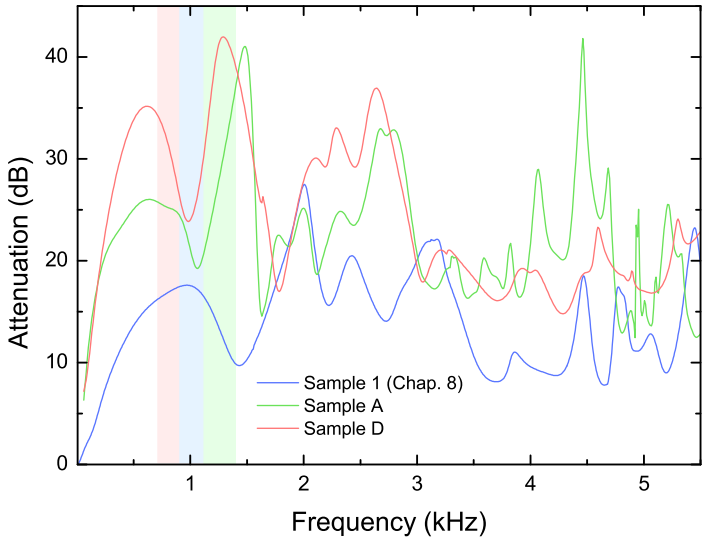


Figure 9.2: Attenuation spectra of the optimized designs for topologies $A$ and $D$ with opaque configuration and calculated through the $\mathcal{T}$ model (see Table 9.1). The attenuation spectrum of sample 1 from Chapter 8 is included as reference.

ered consists of three rows of cylindrical shells with radius 4 cm arranged in a square lattice with a separation of 11 cm between scatterers. As observed, the trend of the quality factor is clear: the $DL_R$ decreases with the radius, and for a given radius the maximum quality is obtained for a specific perforation ratio $\sigma_{opt}$. This optimum perforation ratio is close to zero for relatively high radii, although it increases significantly for radii lower than 100 $\mu$m. The optimum values are represented in Fig. 9.3 with a white line. The maximum $DL_R$ is achieved for the minimum radius considered ($r = 20$ $\mu$m) and $\sigma_{opt} = 33.5\%$, taking a value of 13.13 dB. Note that a careless design can result in very low levels of $DL_R$, even if hole radii lower than 100 $\mu$m are considered. Similar features are found when varying the width of slit-shaped holes in cylindrical shells employing this type of perforations. Thus, it is shown that an appropriate control of the geometrical parameters of the perforations can play an essential role in the design and fabrication of optimum noise barriers.

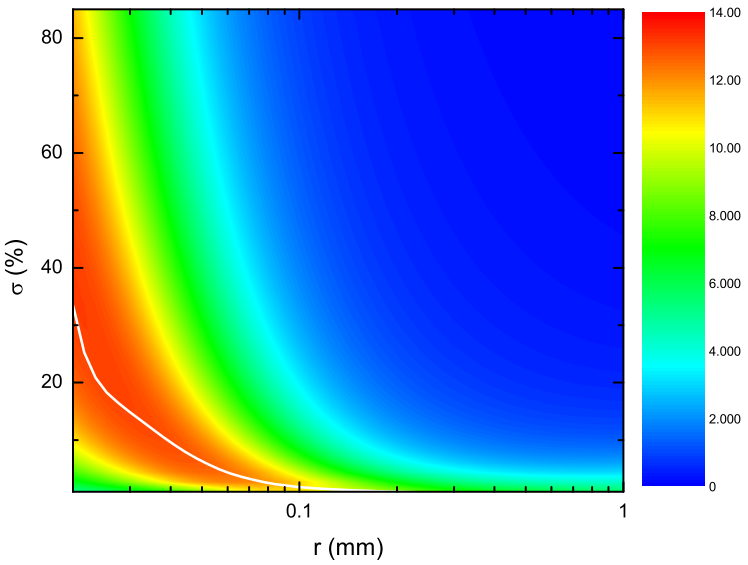


Figure 9.3: $DL_R$ (in dB) of a barrier made with three rows of perforated shells with radius 4 cm arranged in a square lattice with a separation of 11 cm. It is represented for different radius of the holes $r$ and perforation ratio $\sigma$ of the shells. The while line indicates the optimum values of $\sigma$ where a maximum $DL_R$ is achieved for each $r$.

# Chapter 10

# Anomalous absorption in lattices of perforated shells

Up to now, sonic crystals have been studied in an effort to maximize their sound attenuation. However, the aim of this chapter is to pay attention to the case of weakly absorbing scatterers, which can be implemented through perforated shells whose holes are relatively large. In general, the transmittance of lattices made with this type of cylinders is expected to be high, as theoretically and experimentally demonstrated in Chapters 4 and 7. However, it was shown in Fig. 7.7 that a transmission minimum is found in a slab with three rows of perforated scatterers when the wavelength of a normally incident wave approaches the lattice parameter. This chapter is intended to analyze this unusual suppression of transmission, whose origin is related with the excitation of Wood anomalies. Hence, a historical review of this phenomenon is first provided. To better understand the physical mechanisms involved in the anomalies, an analysis of lattices of perforated shells is performed under the assumption of negligible viscous losses. Then, dissipation is introduced in the model and its effect is studied based on the findings obtained from the loss-less scatterers.

## 10.1 Introduction

In 1902, Wood observed unusual dark and bright lines in the spectrum of an optical grating when illuminating it with a white light [Woo02]. He termed

them anomalies since there was not an established theory to explain such a phenomenon. The first interpretation was provided some years later by Rayleigh, who stated that the anomalies are due to the appearance of new diffraction orders which propagate tangentially to the grating [Ray07]. However this theory was incomplete since it was not able to explain all the experimentally observed phenomena. Fano analyzed the underlying physics and identified two types of anomalies [Fan41]. The first of them corresponds to the anomalies already explained by Rayleigh. Fano called them sharp anomalies due to the spectral discontinuity resulting from the emergence of grazing diffracted modes, although they are also known as Rayleigh or diffractive anomalies. The second type is the diffuse or resonant anomaly. It is caused by a resonant interaction between the incident wave and leaky guided modes that are supported by the grating. Fano associated this phenomenon to the excitation of a forced resonance having a complex eigenfrequency, its imaginary part being related with the energy leakage from the periodic grating to the background medium. The response found in these systems is characterized by a resonance with an asymmetric shape known as Fano profile. Since surface modes on the grating are involved, the phenomenon will depend not only on the geometry of the periodic surface and the angle of incidence as in the case of Rayleigh anomalies, but also on the properties of the material of the grating. Both kinds of anomalies may appear separately or almost superimposed when grazing modes couple with the guided leaky modes [HO65]. The resonant anomaly usually occurs at slightly lower frequencies than those where the Rayleigh anomalies are expected.

Because of the many applications of metallic gratings in optics, Wood anomalies have been widely studied. Numerous theoretical and experimental works have been reported since the first relevant papers cited above, leading to a deep understanding of the physical phenomena involved in the anomalies [LP97]. Modern approaches shown that Wood anomalies are based on the excitation of surface plasmon polaritons [RACH68]. In addition, new types of anomaly were identified such as the waveguide type in gratings coated with dielectric layers [MN77]. In fact, these cases correspond to different manifestations of the resonant anomaly introduced by Fano. The study of arrays of dielectric scatterers has been recently reported, the authors providing analytical expressions and numerical proofs of the excitation of Wood

anomalies in a linear arrangement of squared cylinders [MFM+14].

With regard to practical applications, Wood anomalies have been employed in the implementation of guided-mode resonance filters because of their highly selective frequency and angular responses [WM93]. The appearance of anomalies leads to the absorption of energy due to the dissipation to which the surface modes are subjected. This fact was already noted by Wood and Fano, and was later corroborated by several authors who even reported theoretical and experimental evidences of the full absorption of the incident wave [MP76, HM76]. It paved the way for developments such as the proposal of efficient photovoltaic cells [TdAB+08]. Surface plasmon polaritons have proven to be effective in the detection of antigens because of their high sensitivity to changes in a dielectric layer containing the corresponding antibodies [CL90].

The same principles of the Wood anomaly apply for mechanical waves. Although not as extensively as in electromagnetics, the acoustic and elastic counterparts of the Wood anomaly have been also investigated. Many authors analyzed and measured the reflective properties of periodic surfaces during the last century, most of them being focused on corrugated 1D boundaries that support surface modes. First works emphasizing Wood anomalies were reported during the eighties. Jungman et al. observed experimentally the existence of Rayleigh anomalies in an elastic sawtooth profile excited with an ultrasonic beam [JAQ82] and they provided later a theoretical interpretation of the phenomenon [JAAR83, MNL+89]. From these works it was shown that Scholte-Stoneley waves could be generated through diffraction in periodic gratings. It is remarkable the work developed by Declercq and coauthors in this field, who focus on the generation of these type of guided modes [DDBL04, DDBL05]. More recently, Estrada et al. demonstrated that perforated elastic plates can attenuate or transmit sound waves more efficiently than non-perforated plates at wavelengths close to the lattice period [ECU+08]. They stressed the intrinsic differences between the electromagnetic and acoustic approaches and discussed the different mechanisms involved in the transmission of sound through elastic plates with subwavelength perforations immersed in water [EdAC+09].

Wood anomalies were also predicted on 1D arrangements of rigid cylinders [ALK88, LT07], which can be considered as introductory studies of

this phenomenon in sonic crystals. The anomalies found consisted of the Rayleigh-type. Moiseyenco et al. analyzed and measured the distribution of energy between the available diffracted orders of a sonic crystal, although they did not pay attention to the Wood anomalies [MHDL12]. Apart from these works, the literature concerning Wood anomalies on sonic crystals is scarce, especially when the background medium is air.

## 10.2 Samples and theoretical approach

The structure here analyzed is made with the same scattering units as those employed in Chapter 4 to contain rubber crumb. It consists of a square arrangement of perforated shells with a radius of 4 cm and a lattice parameter of 11 cm. The thickness of the plates is $t = 0.5$ mm, the radius of the holes $r = 250$ $\mu$m and the perforation ratio is $\sigma = 14.5\%$. The theoretical approach is based on the T matrix expressed in Eq. (7.3.10), where the impedance of the flat plates is calculated through Eq. (7.1.24) with $\alpha = 4$.

The acoustic transparency of the flat perforated plates has been accurately characterized through a measurement in an impedance tube. A 3.5 cm-diameter disk has been measured through the procedure described by Song and Bolton [SB00]. By following this method the impedance $Z_p$ and wavenumber $k_p$ of the effective medium are obtained and the reflection $\mathcal{R}_p$ and transmission $\mathcal{T}_p$ coefficients of the plate can be calculated though the corresponding expressions of a fluid layer

$$\mathcal{R}_p = \left| R_0 \frac{1 - e^{-2ik_p t}}{1 - R_0^2 e^{-2ik_p t}} \right|^2, \tag{10.2.1}$$

$$\mathcal{T}_p = \left| \frac{1 - R_0^2}{1 - R_0^2 e^{-2ik_p t}} \right|^2, \tag{10.2.2}$$

with

$$R_0 = \frac{Z_p - Z_0}{Z_p + Z_0}, \tag{10.2.3}$$

$Z_0$ being the characteristic impedance of air. From these coefficients the absortion of the plate can be deduced by assuming energy conservation, i. e., $\mathcal{A}_p = 1 - \mathcal{R}_p - \mathcal{T}_p$. Figure 10.1 shows the reflection, transmission and absorption coefficients obtained from the experimental test. The measured

values are in good agreement with the theoretical predictions, thus supporting the validity of the impedance model given in Eq. (7.1.24). The analytical reflectance and transmittance have been obtained from the calculated impedance as

$$\mathcal{R}_p = \left| \frac{Z_p}{2Z_0 + Z_p} \right|^2 , \tag{10.2.4}$$

$$\mathcal{T}_p = \left| \frac{2Z_0}{2Z_0 + Z_p} \right|^2 . \tag{10.2.5}$$

As shown in Fig. 10.1, the reflection and absorption coefficients increase with the frequency, although their values are low. The transmission coefficient is close to one, proving that the energy impinging on the sample is mostly transmitted. Despite this transparency, it is worth noting that due to viscous friction of the air molecules inside the holes, the plate has a low but non-negligible absorption.

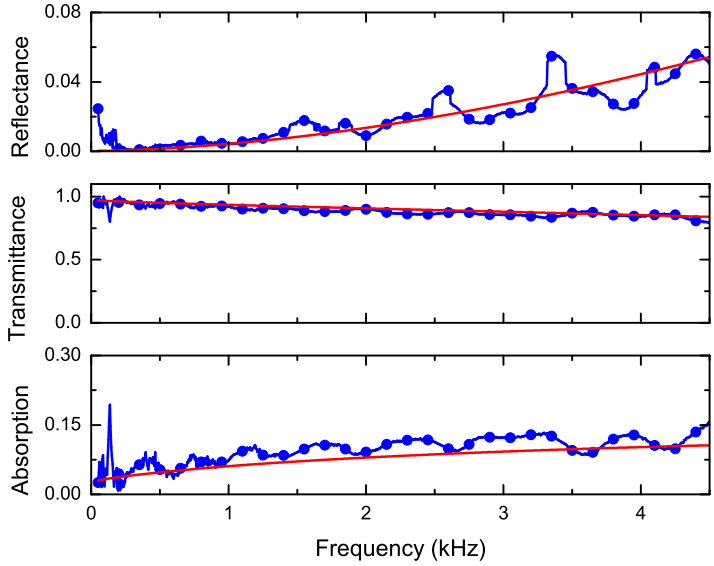


Figure 10.1: Reflectance, transmittance and absorption of a flat perforated plate with parameters $r = 0.25$ mm, $t = 0.5$ mm and $\sigma = 14.5\%$. Red lines correspond to theoretical calculations and blue dots represent experimental data acquired in an impedance tube.

## 10.3 Loss-less scatterers

Energy dissipation inside the holes is neglected by taking the limit of vanishing viscosity $\eta_0$ in the expression of the acoustic impedance, resulting in the loss-less impedance given by Eq. (7.3.30). This impedance is introduced in Eq. (7.3.10) in order to obtain the T matrix of the cylindrical scatterers. The transmittance spectra of sonic crystals having 1, 3 and 5 rows of perforated shells are shown in Fig. 10.2(a). It is almost one in the whole frequency range except around 3 kHz where it reaches a minimum with zero-transmission. The frequency where these phenomena occur is close to the diffraction limit ($\lambda = a$) which in this case is 3118.2 Hz. A zoomed view around the transmission minima is provided in Fig. 10.2(b). Full reflection of sound waves is found even for only one row of scatterers if viscous losses are neglected. In addition to the multiple scattering calculations (continuous lines), the transmittance obtained through finite element simulations of a 3D structure are also included (symbols). There is a good agreement between both types of simulations, the minor discrepancies being derived from our limited calculation capabilities of large 3D domains.

Figure 10.2(b) shows that the transmittance spectrum exhibit a narrow minimum with an asymmetric profile typical from a Fano resonance [Fan41]. It evidences an interference phenomenon occurring between the transmitted sound waves and a resonant state excited in the structure. This effect points to the presence of a resonant Wood anomaly, the resonance corresponding to a leaky guided mode propagating along the slab (normally to the direction of the impinging wave). The position of this resonance is located at wavelengths slightly higher than the diffraction limit, as predicted for this type of anomalies [Fan41]. In addition the position of the resonances shifts to lower frequencies for an increasing number of rows, proving the dependence between the resonant guided modes and the width of the slab. Besides the Fano resonance, additional sharp peaks can be observed in slabs with 3 and 5 rows, and are then analyzed.

The resonant modes of the slab have been obtained through an eigenfrequency analysis of the 3D structure modelled in Comsol. The positions where the resonances occur are indicated with arrows in the upper part of Fig. 10.2(b). There is a reasonable agreement between the frequencies where

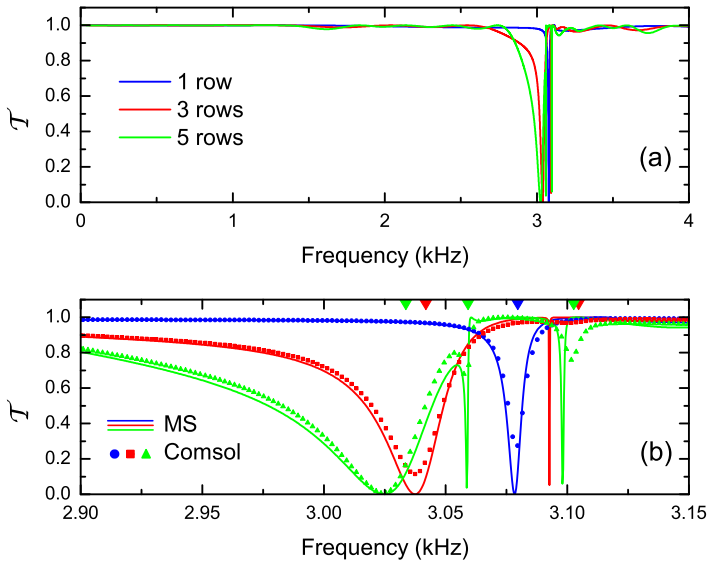


Figure 10.2: Transmittance of lossless slabs with 1, 3 and 5 rows of perforated shells calculated through the multiple scattering theory (a) and zoomed view in the range $2.9 - 3.15$ kHz (b). The symbols correspond to numerical data obtained through 3D finite element simulations. The symbols in the upper part of figure (b) indicate the eigenfrequencies of the resonant states of the slabs. Note that the color of these symbols corresponds to the case having the same line color.

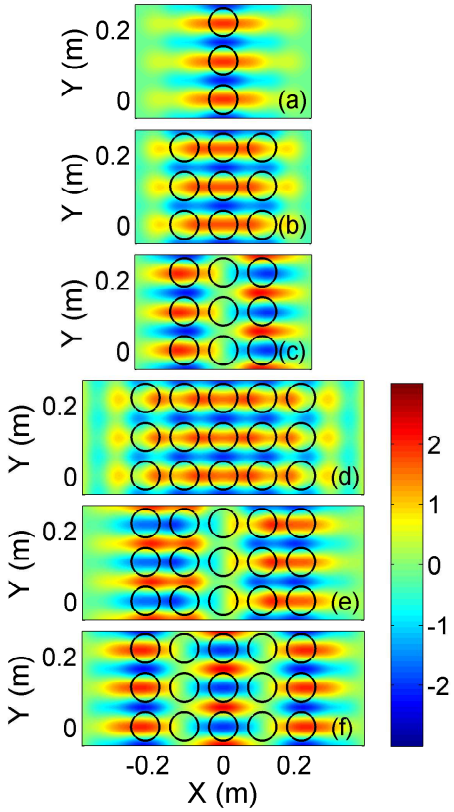


Figure 10.3: Pressure field of the eigenmodes obtained through 3D finite element simulations of slabs with 1, 3 and 5 rows of perforated shells with no losses. The eigenfrequencies of figures (a)-(e) are $3079.7+3.9i$, $3041.9+13.7i$, $3104.7+4.6i$, $3033.7+20.6i$, $3059.2+0.9i$ and $3102.6+2.4i$ Hz, respectively.

the transmission minima appear and the calculated eigenfrequencies, thus supporting the explanation of the observed phenomenon through resonant Wood anomalies. Figures 10.3(a), 10.3(b) and 10.3(d) show the pressure field of the eigenmodes found at the first peak of transmittance in slabs with 1, 3 and 5 rows of scatterers. It is observed a guided mode travelling through the interior of the slab. It consists of a stationary wave based on the combination of two identical modes travelling along the $y$-axis in opposite directions. However, propagating modes that travel in a single direction can be observed in slabs excited with an incident wave having a finite cross section, as shown later.

The extremely narrow peaks in Fig. 10.2(b) are associated with the eigenmodes illustrated in Figs. 10.3(c), 10.3(e) and 10.3(f). These pressure maps indicate that they correspond to resonances of higher-order. While in the previous cases the phase of the modes keeps almost constant along the $x$-axis, in this case two and three lobes appear within the slab. The values of the eigenfrequencies are specified in the caption of Fig. 10.3. Note that they are complex and their imaginary part is related to the lifetime of the resonant modes. The lifetime of the low frequency resonances (Figs. 10.3(a), 10.3(b) and 10.3(d)) decreases significantly with increasing number of rows. A low lifetime in slabs with many rows involves higher leaks from the guided mode to the free space, leading to wider resonances. The higher-order resonances have long lifetimes, which is consistent with the sharp profile of the associated transmission minima.

Similar conclusions can be drawn from multiple scattering calculations of slabs excited with a plane wave at similar frequencies. The resulting pressure maps are illustrated in Fig. 10.4. It is observed a good correspondence between the different subfigures and the eigenmodes shown in Fig. 10.3. Moreover, those modes having a high lifetime present high values of pressure inside the slabs as a result of the excitation of free resonances caused by the low value of the imaginary part of the eigenfrequency. Lower intensities are found in Figs. 10.4(b) and 10.4(d), where this imaginary part is higher and thus the resonances are forced.

The behavior of the lattice can be further analyzed when a sonic crystal slab is excited with a wave having a finite cross section. Figure 10.5 shows a multiple scattering simulation of a slab with 3 rows, each row consisting of 19 perforated shells with no losses. Here, a Gaussian beam at the frequency of the first zero-transmission minimum (3037.3 Hz) impinges normally to the slab from the left side (see blue arrow). The modes guided by the structure are clearly visible. When they reach the upper and lower ends of the slab, they leave it resulting in two 90°-redirected beams travelling along the $y$-axis (black arrows). Moreover it is observed the leaky nature of the guided modes through the waves leaving the sample at those positions where neither the impinging wave nor the ballistic transmission are present (red arrows). Although the slab is excited at the frequency where full reflection was found, the ballistic transmittance (white arrow) is high. This shows that the trans-

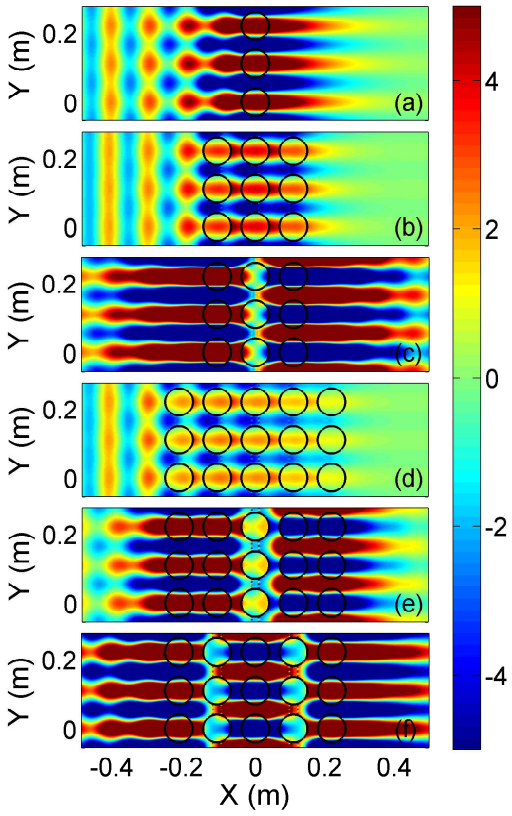


Figure 10.4: Pressure maps of a plane wave impinging on slabs with 1, 3 and 5 rows of perforated shells with no losses. The frequencies of figures (a)-(f) are 3078.3, 3037.3, 3092.67, 3024.7, 3058.7 and 3098 Hz, respectively.

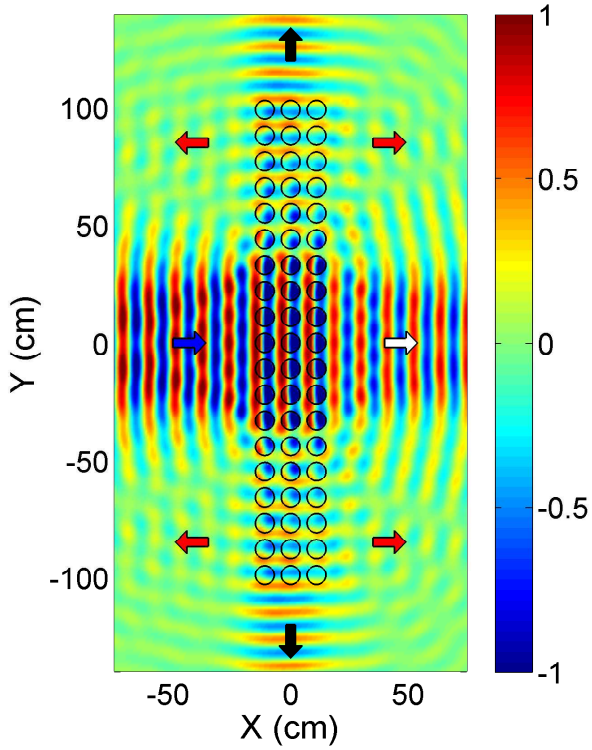


Figure 10.5: Pressure map of a Gaussian beam with frequency 3037.3 Hz impinging on a slab with 3 rows of perforated shells, each row having 19 units. The arrows indicate the direction of propagation of the different waves observed entering or leaving the sample.

mission suppression in lattice of loss-less perforated shells occurs as the slab becomes longer and the incident wavefront broadens.

## 10.4 Lossy scatterers

Figure 10.6 shows the reflectance $\mathcal{R}$, transmittance $\mathcal{T}$ and absorption $\mathcal{A}$ calculated for slabs with 1, 3 and 5 rows when the dynamic viscosity of air ($\eta_0 = 17.8\ \mu\text{Pa} \cdot \text{s}$) is taken into consideration. Now the transmittance is not unity but its value is still high. The transmittance spectra present a single minimum that appears at frequencies close to the diffraction limit and shifts to lower frequencies with increasing number of rows. Therefore, the

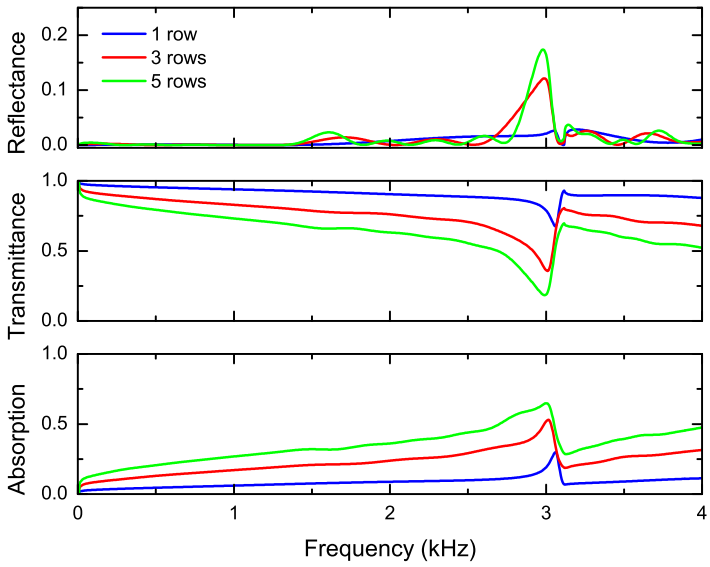


Figure 10.6: Theoretical reflectance, transmittance and absorption of lattices of SCs having 1 to 5 rows of perforated shells when considering viscous losses. Notice that the reflectance spectrum is plotted in a narrow range for better visualization.

Wood anomalies still exists in lattices of perforated shells with viscous losses, although their amplitudes are smaller and their frequency response broadens due to the dissipation. Note that the transmittance of a slab with 3 rows of shells of Fig. 10.6 is directly compared with experimental data in Fig. 7.7(b).

It is also noticeable that the reflectance spectrum takes low values compared to absorption, even in the resonance where full reflection was found in the non-lossy case. In this region reflectance is enhanced, although the total attenuation of the slabs is mainly due to energy dissipation. As observed in the lossless case, the resonant anomaly involves a guided wave that travels along the axis of the slab. It is worth noting that the energy which is coupled to such guided mode travels perpendicular to the incidence direction along the interior of the slab. Thus, the sound is deviated from the free space to a path with low losses but which is infinitely long, in such a manner that it is slowly dissipated as it propagates. This results in the absorption

enhancement observed in Fig. 10.6.

The coupling between the incident wave and the guided modes can be improved by increasing the filling fraction of the SC, i. e., by reducing the separation between cylinders. A sweep of the lattice parameter has been performed while the radius of the cylinders has been kept constant at 4 cm. Figure 10.7 shows the corresponding 2D map of absorption calculated for a slab with three rows of scatterers as a function of the frequency and the filling fraction of the SC ($ff = \pi(R/a)^2$ for a square lattice). It is clearly observed the band where the anomaly occurs. It is located at slightly lower frequencies than the diffraction limit, which is indicated with a dash line. In addition to the first anomaly, a second branch can be observed. It corresponds to the frequency where the wavelength approaches one-half lattice parameter. The maximum absorption is found for the maximum filling fraction considered in the calculations ($ff = 69.6\%$), for which the separation between cylinders is $a = 8.5$ cm. At this point the absorption is $\mathcal{A} = 0.77$ and the transmittance drops to $\mathcal{T} = 0.08$. A similar behavior is found for the cases of 1 and 5 rows, whose minimum transmittance takes the values $\mathcal{T} = 0.44$ and $\mathcal{T} = 0.012$, respectively.

It is worth noting that an arrangement of two parallel plates has similar levels of absorption when compared to an arrangement of one row of perforated cylinders. Thus the two parallel perforated plates would represent the front and rear surfaces of the row of cylinders. As a 1D slab, it will show attenuation bands (or bangaps) that depend on the separation between plates. However the response of such a system is less selective. The implementation with cylinders results in attenuation mechanisms that are focused on a narrow band, allowing a high transmittance of sound at the remaining spectrum. An example is given in Fig. 10.8, where the transmittance of one row of cylinders is compared with that of two parallel plates with similar perforations. It is observed that the overall transmittance of the slab of perforated shells is higher, although it presents a narrow peak where losses are highlighted. This lead to potential applications such as notch filters, where only a sharp specific band is intended to suppress.

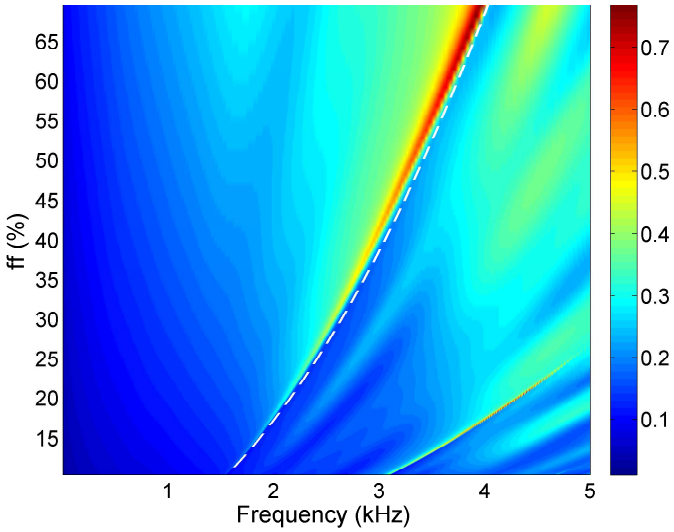


Figure 10.7: Sound absorption of a slab of three rows of perforated shells as a function of the frequency and the filling fraction of the lattice. The cylinders are the same as those used in the previous figures, varying only the lattice parameter from 8.5 cm to 22 cm for the sweep of filling fraction.

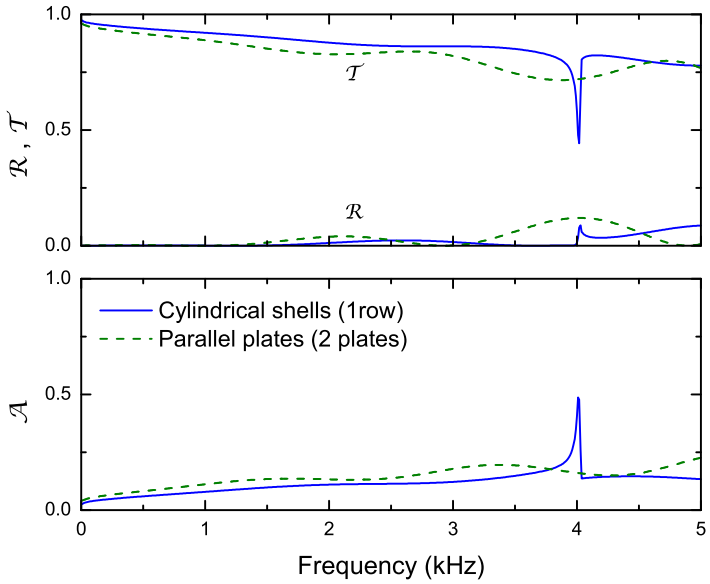


Figure 10.8: Reflectance, transmittance and absorption spectra of one row of cylindrical perforated shells (solid lines) and an arrangement of two parallel plates having the same perforations than the shells (dashed lines). The distance between the centers of nearest-neighbors cylinders and between the parallel plates is 8.5 cm. Viscous losses have been considered in the calculations.

# Part III

# Acoustic cloaking

# Chapter 11

# Introduction

## 11.1 Acoustic cloaking

Invisibility is a fascinating phenomenon that, until recently, was only found in science fiction novels and films. However this topic began to attract the interest of many scientists since Leonhardt and Pendry simultaneously reported a theory capable of designing invisibility cloaks for electromagnetic waves [Leo06, PSS06]. The idea is to surround an object with a cover which guides the waves and prevents them to interact with the hidden object. The waves emerge from the cloak keeping their initial trajectory as if they had traveled through the empty space, thus making the object invisible to any external observer. The approach was based on a coordinate transformation technique which maps a Cartesian space into a distorted mesh having a region which does not exist in the original space. This region corresponds to the space where the object to be hidden is inserted. Maxwell's equations have the same form in both coordinate systems, the geometrical differences being expressed in terms of the anisotropic and inhomogeneous constitutive parameters of the material composing the cloak.

Thus, the challenge of designing an invisibility cloak will depend on the ability to find materials with the required exotic parameters. Unfortunately, these properties are not found in natural materials and therefore the cloak should be implemented by means of artificially engineered structures, also referred to as metamaterials. They essentially consists on periodic arrangements of subwavelength units whose individual properties results in an ef-

fective medium with extraordinary parameters [PHRS99, SW11]. Given this background, the first practical realization of a cloak was reported in 2006 by Schurig and coauthors, who concealed a copper cylinder at microwave frequencies by surrounding it with a metamaterial based on split-ring resonators [SMJ+06]. Due to the difficulty of achieving the extreme constitutive parameters required by the theory, a reduced set of material properties was considered. The resulting cloak presented a similar phase velocity profile than the ideal implementation, although its impedance was not matched with the background, which resulted in some unwanted scattering.

From these early works, many theoretical and experimental studies have been reported so far. Interested readers are addressed to the reviews in Refs. [AE08, FA14]. In general the complexity of the required parameters has always led to different simplifications that result in feasible implementations at the expense of some performance limitations. One of the more relevant examples is the carpet cloak, which considers a simpler geometry and hides an object placed over a reflecting surface [LP08, LJM+09]. Besides refractive devices based on transformation optics, other physical mechanisms have also been considered to achieve invisibility. In this way scattering cancellation has proven to be an effective approach. It is based on the control and minimization of the scattering cross section of the system [CSA12]. By following this idea, a plasmonic cloak made through a metamaterial near its plasma resonance was proposed by Alù and Engheta [AE05] and later demonstrated [RKM+12]. Cloaks based on complementary media are calculated through transformation optics, although their operation can be compared to the scattering cancellation mechanism. They are based on the inclusion of a complementary image made with negative materials that cancels the scattering of the object, even allowing the concealment of objects placed outside the cloak [LCZC09].

The research on invisibility was also extended to other types of waves such as surface waves in liquids [FEGM08] and elastic waves [FGE09, SWW12]. The acoustic counterpart of the devices reported for electromagnetic waves has also been studied. The similarities between the electrodynamic and acoustic wave equations lead to an analogous approach named transformation acoustics. The inhomogeneous constitutive parameters of an ideal acoustic cloak were deduced by Cummer and Schurig [CS07]. The parameters

here reported were based on an isotropic bulk modulus and anisotropic mass density, both of them being inhomogeneous. An additional approach with isotropic mass density and anisotropic bulk modulus was later proposed by Norris [Nor09]. As in electromagnetic cloaks, the anisotropic and extreme values of the acoustic parameters resulted in non-feasible practical implementations. However, Torrent and Sánchez-Dehesa demonstrated that the cloak with anisotropic mass density could be implemented through a set of concentric layers made with isotropic media [TSD08a]. Although anisotropic materials were no longer required, the extreme properties of the resulting materials were still rarely found in nature.

Similarly to the electromagnetic case, the study of acoustic cloaking was subjected to the development of metamaterials capable of achieving specific properties. The study of acoustic metamaterials is a topic of intense research due to their potential applications. For instance, effective media showing negative bulk modulus [FXX$^+$06, GCGST$^+$12], mass density [LZM$^+$00, PPL$^+$11] or both simultaneously [LC04,GSGCTSD13] have been already reported. Despite this progress in material engineering, the fabrication of acoustic cloaks continues being a challenge and reported devices assume simplifications that degrade their performance.

The first demonstration of an acoustic cloak was performed at ultrasonic frequencies with a steel cylinder surrounded by a planar structure immersed in water [ZXF11]. Some months later a ground cloak was experimentally characterized [PZC11]. This cloak was based on an anisotropic metamaterial made with parallel perforated plates. The same type of sample was recently reported in 3D, being one of the few experimental demonstrations of a 3D acoustic cloak [ZPC14]. In both cases the authors claimed a broadband behavior of the devices. The employed metamaterials were designed by considering a reduced set of acoustic parameters and therefore the cloaks were slightly mismatched with the impedance of the background. Scattering cancellation has been also considered in acoustics. It was shown that a set of elastic or fluid layers (with positive and isotropic parameters) surrounding a solid object can reduce the scattering cross section up to negligible levels [GAH11, GHA12]. It is worth noting that one of the drawbacks of this approach is the specific knowledge of the shape and the material properties of the object being hidden, in such a manner that a new cloak must be de-

signed if some of the object properties changes. Acoustic complementary cloaks have been also proposed, demonstrating that they can be engineered through single negative materials [ZLK+11]. A hybrid cloak that combines the two aforementioned mechanisms was also reported by Martin and coworkers [MO12]. They proposed a fluid scattering cancellation layer surrounded by a non-ideal supercell based on transformation acoustics, showing a remarkable improvement with respect to the implementation of each cloak type separately.

## 11.2 Objectives

The aim of the next chapters is to report new advances in the topic of acoustic cloaking. Due to our experience in acoustic metamaterials for airborne sound, the presented cloaks are intended to work in air and, in addition, by employing solid materials. The design of structures embedded in this background results in a high impedance contrast with respect to almost any low loss solid or fluid, in such a manner that they can be considered as rigid materials with infinite mass density. Therefore refraction between different media cannot be here considered, unlike other backgrounds like water. This drawback strongly limits the design of acoustic metamaterials. Other alternatives such as the use of membranes could be considered, although they have disadvantages like the high degree of precision required for tuning the tension of each membrane. The implementation based on rigid materials presents the advantage of being mechanically robust and, in addition, the resulting structures are easier to fabricate.

Despite being a topic of intense research, most of the available literature deals with theoretical approaches and only a much reduced number of experimental works have been reported. Because of this, one of the main goals of this work is to perform the experimental characterization of acoustic cloaks. It will be shown that, due to the aforementioned limitations, this objective will be only accomplished by assuming severe limitations on the operation of the resulting devices.

# Chapter 12

# Reduced acoustic cloak based on temperature variations

This chapter proposes a new approach to control the propagation of sound through metamaterials based on rigid structures. The underlying physical mechanism is based on the dependence of the air properties with the temperature. The chapter begins with the formulation of a perfect cloak obtained through the transformation acoustics theory. From this model, a reduced implementation is developed as a set of concentric layers where the background fluid of each layer is conveniently heated or cooled. It will be shown that this system can be approached through an arrangement of cylinders whose surfaces are set at specific temperatures. Theoretical and simulated data will be provided to discuss the performance of the proposed cloak. It is worth mentioning that this temperature-based approach not only allows the implementation of acoustic cloaks, but it turns out to be a general technique for designing acoustic metamaterials.

## 12.1 Transformation acoustics cloak

Consider a cylindrical domain defined as $0 < r < R_b$. This space can be mapped into the annular region $R_a < r' < R_b$ of a transformed system by applying the simple rule

$$r' = R_a + \frac{r(R_b - R_a)}{R_b}. \tag{12.1.1}$$

Since the space within $r' < R_a$ does not exist in the original system, this region is not accessible to any impinging wave. In addition, the cylindrical shell of the transformed space will behave as the empty space provided that the region $r < R_b$ is filled with the background medium. The acoustic Helmholtz equation is invariant under the above coordinate transformation, which results in a set of constitutive parameters [CS07]

$$\rho_r(r) = \rho_0 \frac{r}{r - R_a}, \tag{12.1.2a}$$

$$\rho_\theta(r) = \rho_0 \frac{r - R_a}{r}, \tag{12.1.2b}$$

$$B(r) = B_0 \left( \frac{R_b - R_a}{R_b} \right)^2 \frac{r}{r - R_a}, \tag{12.1.2c}$$

where $\rho_0$ and $B_0$ are the mass density and bulk modulus of the fluid background. The parameters defining the cylindrical shell (or cloak) are inhomogeneous since depend on the radial coordinate. They diverge as $r$ approaches $R_a$, this fact being a major drawback for its practical implementation. The phase velocity profiles can be expressed as

$$c_r = \sqrt{\frac{B(r)}{\rho_r(r)}} = \frac{R_b - R_a}{R_b} c_0, \tag{12.1.3a}$$

$$c_\theta = \sqrt{\frac{B(r)}{\rho_\theta(r)}} = \frac{R_b - R_a}{R_b} \frac{r}{r - Ra} c_0, \tag{12.1.3b}$$

where $c_0$ is the sound speed of the background. It is found that the radial velocity is constant and lower than $c_0$, while the angular velocity is always larger than $c_0$ and depends on the radial coordinate. The requirement of sound speeds higher than that of the background is another drawback in the design of acoustic cloaks in air, since acoustic metamaterials based on rigid inclusions tend to reduce the effective sound velocity.

With regard to the mass density, it is shown in the above formulas that this parameter is anisotropic. Anisotropic inertia is not a property of natural fluids, although it can be achieved through artificial structures [PL08, TSD08b]. Moreover, the realization of an acoustic cloak with the properties expressed in Eqs. (12.1.2) was proposed by means of a multilayered structure with concentric layers whose fluids are made of two alternating

media: one with low ($\rho_-$) and another with high ($\rho_+$) isotropic densities. The expression of both set of parameters is [TSD08a]

$$\rho_\pm(r) = \rho_r(r) \pm \sqrt{\rho_r^2(r) - \rho_r(r)\rho_\theta(r)}, \tag{12.1.4}$$

where $\rho_r$ and $\rho_\theta$ are given in Eqs. (12.1.2a) and (12.1.2b). The main issues of this layered structure are the intrinsically instability of any mixture of fluids with different densities and the extreme values that are still required when $r$ approaches $R_a$. Despite being derived from the parameters of a perfect cloak, this implementation does not result in an ideal operation due to the finite number of layers. Obviously, a higher number of layers results in better performance. In turn, the quality of the cloak does not depend on the thickness of its layers and therefore it is possible to design devices as thin as desired, provided the associated fabrication difficulties are assumed. An example is given in Fig. 12.1 where the operation of a cloak made with 100 layers is illustrated. The external radius is chosen as $R_b = 2R_a$ and the wavelength of the impinging wave is $\lambda = 2R_a$. It is shown how the cloak guides the sound around the object and then reconstructs the wavefront as if the wave had travelled through the empty space.

## 12.2 Implementation through temperature variations

In the last section some of the difficulties for obtaining an acoustic cloak were described. One of them is the requirement of a sound speed higher than $c_0$. The inclusion of a rigid matrix in a fluid leads to metamaterials having always lower velocities than that of the background. In order to implement an acoustic cloak it is required to find a physical mechanism making possible that sound waves travel at higher velocities. It is known that temperature has a direct influence on the mass density while the bulk modulus remains constant. By assuming that the density of air is $\tilde{\rho_0} = 1.29$ kg/m$^3$ at $T_0 = 273$ K, the general expression of the density has the form [Ber86]

$$\rho_0(T) = \tilde{\rho_0}\frac{T_0}{T}, \tag{12.2.1}$$

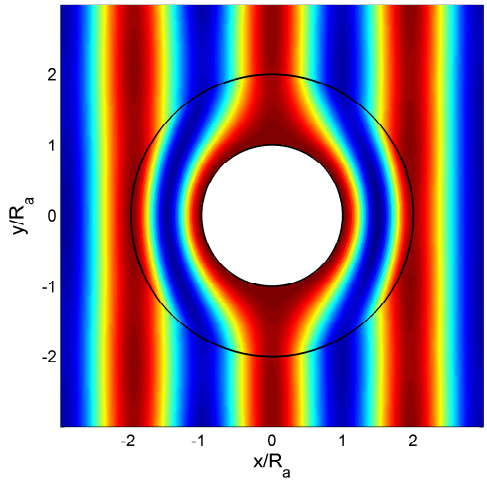


Figure 12.1: Acoustic cloak with inner $R_a$ and outer $R_b = 2R_a$ radii when a plane wave with wavelength $\lambda = 2R_a$ impinges on it. The cloak consists of an arrangement of 100 concentric isotropic layers whose parameters are obtained through Eqs. (12.1.2) and (12.1.4) (see Ref. [TSD08a] for more details).

which results in a sound speed

$$c_0(T) = \sqrt{\frac{B_0}{\rho_0(T)}} = \tilde{c_0}\sqrt{\frac{T}{T_0}}, \tag{12.2.2}$$

where $\tilde{c_0}$ is the sound speed at $T_0$. Thus it is shown that higher and lower sound velocities can be achieved through the control of the air temperature.

The issue is how to implement a metamaterial able to control the temperature of the background. The solution consists of setting the temperature of the solid inclusions employed in building the acoustic metamaterial. The proposal here developed considers an arrangement of identical rigid cylinders whose surfaces are heated or cooled at specific temperatures. A simple scheme of the proposed structure is shown in Fig. 12.2. Here a central rigid cylinder is surrounded by a series of concentric layers. The cylinders of each layer are set to the same temperature according to the required mass density. Due to the alternating profile of the density modelled in Eq. (12.1.4), it is expected that hot and cold layers are successively arranged.

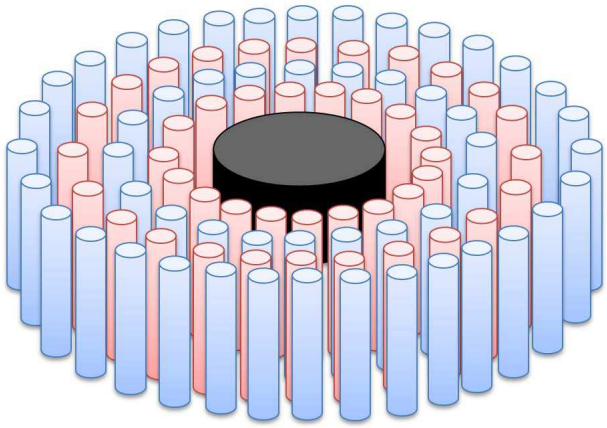

Figure 12.2: Scheme of the proposed cloak that employs temperature as the mechanism allowing the control of sound waves. It is based on a central cylinder surrounded by concentric layers of cylinders heated or cooled at different temperatures.

According to the homogenization theory of sonic crystals, the mass density of a periodic distribution of rigid cylinders can be expressed as [THCSD06]

$$\rho_{eff} = \frac{1+ff}{1-ff}\rho_0(T), \tag{12.2.3}$$

where $ff$ is the filling fraction of the lattice. Note that the effective density depends on both the temperature and the filling fraction. On the other hand, the bulk modulus is

$$B_{eff} = \frac{B_0}{1-ff}, \tag{12.2.4}$$

and does not depend on the temperature. From the above equation it is clear that $B_{eff} > B_0$. Since the bulk modulus of the ideal cloak expressed in Eq. (12.1.2c) is lower than $B_0$ at some points, it is concluded that perfect cloaks are not realizable by using the temperature as here described. However, the temperature approach can be used to realize reduced cloaks in terms similar to those proposed for electromagnetic waves [SMJ+06], which have the phase velocity profile of the ideal implementation [see Eqs. (12.1.3)], although the impedance is not matched with that of the background. This results in a non-zero reflectance at the expense of using the following reduced set of

parameters:

$$\hat{\rho}_r(r) = \alpha \left( \frac{R_b}{R_b - R_a} \right)^2 \rho_0, \tag{12.2.5a}$$

$$\hat{\rho}_\theta(r) = \alpha \left( \frac{R_b}{R_b - R_a} \right)^2 \left( \frac{r - R_a}{r} \right)^2 \rho_0, \tag{12.2.5b}$$

$$\hat{B}(r) = \alpha B_0. \tag{12.2.5c}$$

Here $\alpha$ is an arbitrary parameter that takes values $\alpha \geq 1$. From Eqs. (12.2.4) and (12.2.5c) a direct relation between $\alpha$ and the filling fraction can be established

$$ff = 1 - \frac{1}{\alpha}. \tag{12.2.6}$$

Thus a large value of $\alpha$ implies a high filling fraction, which is a good condition to accurately set the air temperature at the different layers since there is less empty space between cylinders. However a high filling fraction also leads to a dense lattice and a higher impedance mismatch between the cloak and the background.

In this work a value of $\alpha = 1.4$ has been chosen, resulting in a filling fraction of 28.6%. Once the filling fraction is fixed, the mass density of each layer can be obtained by adjusting the temperature in Eq. (12.2.3). Thus, the temperatures $T_+$ and $T_-$ of the layers having high and low densities are expressed as

$$T_\pm(r) = \frac{1 + ff}{1 - ff} \frac{\rho_0}{\rho_\pm(r)} T_0, \tag{12.2.7}$$

where $\rho_\pm$ are the mass densities from Eq. (12.1.4) with the anisotropic components described in Eq. (12.2.5).

The cylinders are arranged in concentric layers around the cloaked object. This distribution is named circular acoustic crystal (CAC), in a similar manner to the analogous photonic structure [HSN+04]. The position of the $m$th cylinder of the $\ell$th layer is given by

$$\vec{r}_{\ell m} = a(\ell + \ell_0) \left[ \cos(\Phi)\hat{x} + \sin(\Phi)\hat{y} \right], \tag{12.2.8}$$

with

$$\Phi = \frac{2\pi m}{6(\ell + \ell_0)}, \tag{12.2.9}$$

where $a$ is the radial distance between concentric layers and $\ell_0$ is an integer that defines the inner cloak radius $R_a = a\ell_0$. The total number of layers $N$ of

the shell determines the external radius of the cloak $R_b = R_a + aN$. Each layer has $6(\ell + \ell_0)$ cylinders located at the radial coordinate $r_{\ell m} = a(\ell + \ell_0)$ and separated by an angle of $\Delta\varphi_{\ell m} = 2\pi/6(\ell + \ell_0)$. This results in an arc-length of $d = r_{\ell m}\Delta\varphi_{\ell m} = 2\pi a/6$ between nearest-neighbor cylinders. To calculate the filling fraction of a CAC, consider a single layer of the structure. The area filled by the cylinders is $A_c = 6(\ell + \ell_0)\pi r_{cyl}^2$, $r_{cyl}$ being the radius of the cylinders. The area occupied by the layer shell is

$$A_s = \pi\left[\left(r_{\ell m} + \frac{a}{2}\right)^2 - \left(r_{\ell m} - \frac{a}{2}\right)^2\right] = 2\pi r_{\ell m} a = 2\pi a^2(\ell + \ell_0). \quad (12.2.10)$$

Thus the filling fraction of the CAC is

$$ff = \frac{A_c}{A_s} = 3\frac{r_{cyl}^2}{a^2}, \quad (12.2.11)$$

which is independent on $\ell$ and therefore the cylinders of the different layers have the same radius $r_{cyl} = a\sqrt{f/3}$.

The sample considered in this work has a shell with $N = 20$ layers and an external radius $R_b = 3R_a$. Consequently $\ell_0 = 10$ and $a = R_a/10$. The total number of cylinders $M$ can be calculated thought the expression

$$M = \sum_{\ell=1}^{N} 6(\ell + \ell_0) = 3N(N+1) + 6N\ell_0 \quad (12.2.12)$$

which results in M=2460 cylinders. However, an additional layer of cylinders should be taken into account to set the ambient temperature in the air surrounding the device at $r > R_b$. Otherwise the temperature profile would decay slowly from the last layer of cylinders due to its large temperature difference with the background. Because of this, a new outer layer whose cylinders are set to the background temperature is included, increasing the required number of cylinders up to M=2646.

## 12.3 Results

Simulations of the whole CAC have been performed through the finite element method with Comsol Multiphysics. First, the temperature profile of the different layers has been characterized. To do this, Laplace's equation

has been solved in a 2D domain where the surfaces of the cylinders are heated or cooled to those values derived from Eq. (12.2.7). Figure 12.3 shows the analytic required profile compared to the simulated data. It is found a good agreement between the air temperature set by the cylinders and the expected analytical values. The inset of the figure shows a temperature map in logarithmic scale. A layered distribution of temperatures is clearly observed and evidences the creation of a layered mass density profile. Nevertheless it is worth noting that the required temperature values are extreme and therefore the proposal is hardly realizable in practice.

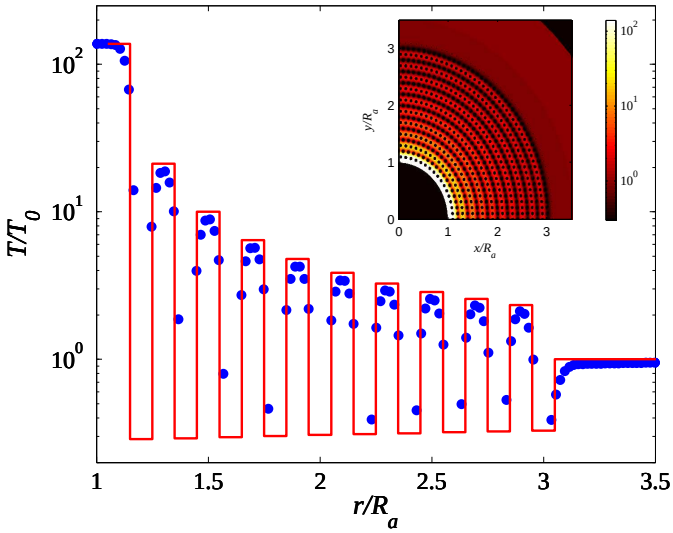


Figure 12.3: Temperature profile of the reduced acoustic cloak (continuous line) compared with the profile obtained by heating or cooling the cylinders arranged around the cloaked object (dots) . The inset shows the 2D distribution of temperature.

The performance of the acoustic cloak has been checked through the simulation of a plane wave impinging on the device. To account for the local density variations due to the temperature profile, the mass density of air has been derived from Eq. (12.2.1) where $T(x, y)$ is the temperature distribution previously calculated through Laplace's equation. Thus, the acoustic Helmholtz equation is solved for the arrangement of rigid cylinders embedded in a background whose mass density is temperature-dependent. The results are compared to those from a bare cylinder and a perfect cloak

with the same number of layers. The backscattered field has been calculated since it is a parameter characterizing the performance of the cloak. Figure 12.4 shows this parameter for the three aforementioned cases as a function of the normalized frequency of the incident wave. Due to the low number of layers, even the perfect cloak presents a non-negligible backscattering. Its value is much lower than the case of a bare cylinder at low frequencies and increases at higher frequencies. It is observed that the reduced cloak is able to reduce the backscattered with respect to the bare cylinder in some frequency bands where its performance is comparable to the ideal cloak. Both cloaks have higher backscattering than the bare cylinders at some frequencies. At this point it is worth mentioning that these devices have an external radius equal to three times the radius of the central cylinder and, in addition, a low number of layers. It is expected that a higher number of layers results in better performance.

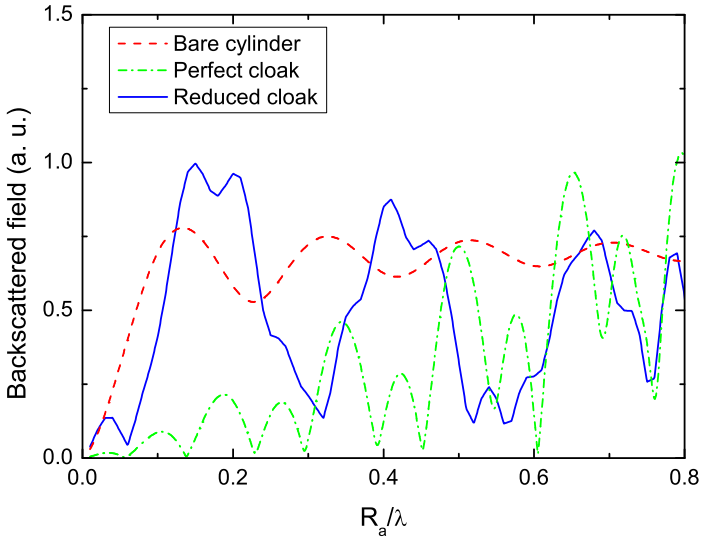


Figure 12.4: Backscattered field produced by a rigid cylinder of radius $R_a$ (dashed line) compared to the fields produced by the cylinder surrounded with two different cloaks: a perfect cloak made of 20 homogeneous layers (dashed-dot line) and the reduced cloak implemented through an arrangement of heated/cooled cylinders (continuous line).

Figure 12.5 shows the real part of the pressure field when a plane wave with wavelength $\lambda = 3R_a$ arriving from the left impinges on the object with a reduced cloak. The upper panel corresponds to a numerical simulation performed for the layered structure, each layer being made with a homogeneous fluid. The lower panel shows the data resulting from the finite element simulation of the system of rigid cylinders. The field distributions show a similar behavior in which the wavefront surrounds the object and is partially reconstructed at the outer side of the cloak. Note that some scattered field appears a consequence of the impedance mismatch of the reduced set of parameters of the shell. As previously mentioned, it is expected an improvement of the cloaking phenomenon for an increasing number of layers, as occurs in the case of the perfect implementation.

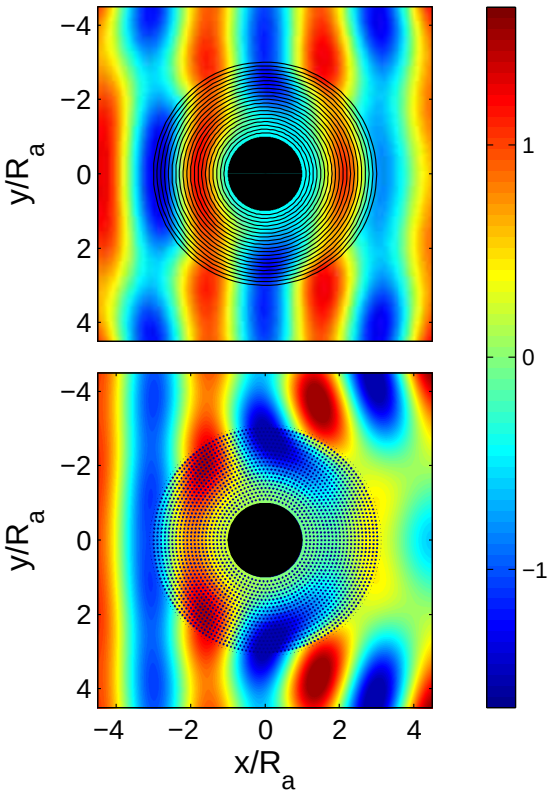


Figure 12.5: Real part of the pressure pattern produced by the scattering of a plane sound wave with wavelength $\lambda = 3R_a$ impinging on a reduced cloak made of layered metafluids. The upper panel shows the case of a cloak whose layers are made with isotropic and homogeneous fluids while the lower panel is based on a layered distribution of cylinders heated or cooled at specific temperatures.

# Chapter 13

# Two-dimensional cloak based on scattering cancellation

In the last chapter the design of acoustic cloaks through transformation acoustics was introduced and an approach based on the temperature of the background was developed. However the need for extreme temperature profiles makes this proposal unfeasible. This problem is common when dealing with cloaks derived from coordinate transformation techniques since they generally result in hardly realizable parameters. In order to provide a feasible implementation, a different approach is considered in this chapter. Scattering cancellation will be used here as the physical mechanism that renders an object acoustically invisible. The design procedure of a 2D cloak, which is based on a numerical optimization, is first reported. Then, the construction of the cloak as well as the 2D environment required to perform the experimental characterization are described. Finally the results obtained from the measurements are shown and the performance of the device is discussed.

## 13.1 Design

The basic idea of the scattering cancellation technique is to design a cloak producing a scattered field which cancels the scattering of the object intended to conceal. In this scheme the incident wave interacts with the central object unlike the ideal operation of the cloaks based on transformation acoustics. The new approach has the advantage of allowing the hidden device to sense

the external field, as recently reported [GAH14]. However the parameters of the cloak will depend on the acoustic properties and the dimensions of the hidden object. The proposed cloak is designed to work with airborne sound and employs rigid materials due to their robustness and ease of fabrication. This assumption strongly limits the design possibilities and it is not possible to achieve the operating conditions of an ideal implementation. Instead, the device will work in a narrow frequency range and only for waves coming from a specific direction.

The object to be cloaked is a rigid cylinder with radius $R_0 = 11.25$ cm. The impinging sound is a plane wave with frequency 3 kHz, that corresponds to the condition $\lambda = R_0$. The cloak consists of a distribution of 120 rigid cylinders with radius $r_0 = 7.5$ mm that surround the central object. Their positions are determined through a numerical optimization which combines two different methods: genetic algorithms (GA) and simulated annealing (SA).

GA are heuristic search algorithms inspired by the Darwinian evolution process [Gol89]. They start with an initial population of candidate solutions. Each candidate has a set of properties (chromosomes) related to the different parameters of the search space. New candidates are successively generated through random modifications of their properties (mutations) or the combination of several individuals (crossover). Each new solution is evaluated by means of a fitness function and the best candidates are selected for the next generation. This method is especially useful when dealing with huge search spaces and has been previously employed in the optimization of photonic and sonic crystal slabs [SHLZ$^+$04, HSDS04]. However the search space of the proposed cloak is too large even for GA and it needs to be combined with an additional method. SA is a global optimization technique based on the process of cooling melted solids in order to obtain uniform crystalline structures with minimum free energy [KJV83]. Starting from a given state, a new one is generated through some well-defined way (in this case a sequence of GA optimizations) and it is evaluated through the objective function. This new state is always selected if it has less energy. If the energy is higher, it is selected with a certain probability that depends on a parameter named temperature. The choice of worse solutions avoids converging to local optimums. As the algorithm progresses, the temperature and the transition probability

towards worse solutions are reduced until they reach zero.

Let $(x_n, y_n)$ the position of a given cylinder in the $n$-th iteration. The position in the next annealing step is defined by

$$x_{n+1} = x_n + T_n j_x, \tag{13.1.1}$$

$$y_{n+1} = y_n + T_n j_y, \tag{13.1.2}$$

where $T_n$ is the temperature and $(j_x, j_y)$ are integer numbers obtained through a short sequence of GA optimizations. Once the new positions are known, the quality of the candidate is evaluated through the fitness function. The transition to the new solutions is decided according to the difference between the current and previous fitness $\Delta E$. The probability of transition towards a worse state is here defined as $e^{-\Delta E/T_n}$.

The fitness function employed to search the optimum positions of the cylinders should be focused on the scattering cross section. However, a more efficient calculation is given by

$$F = 1 - \frac{\sum_{i=1}^{360} |P_t(r_c, \theta_i)|^2}{\sum_{i=1}^{360} |P_0(r_c, \theta_i)|^2} \tag{13.1.3}$$

where $(r_c, \theta_c)$ are the polar coordinates of 360 points uniformly distributed in a circumference with radius $r_c$ and centered in the central object. $P_t$ is the total pressure field of the system (calculated with the multiple scattering theory) and $P_0$ is the incident plane wave. Note that the second term of the formula evaluates how different are the incident wave and the total pressure field. It vanishes when both fields are similar and, therefore, $F = 1$ defines the complete acoustic concealment.

The optimization tool starts with a uniformly distributed set of cylinders and iterates until $T_n = 0$. The resulting distribution of cylinders is shown in Fig. 13.1. The cylinders are not uniformly arranged, although the cloak has a double mirror symmetry with respect to the planes passing through the $x$ and $y$-axes. The fitness of the solution is $F = 0.977$, indicating a remarkable concealment. The operation of the cloak is illustrated in Fig. 13.2 and compared to the scattering of a bare cylinder. As shown, the scattering produced by the large cylinder is almost completely cancelled when it is surrounded by the arrangement of small cylinders.

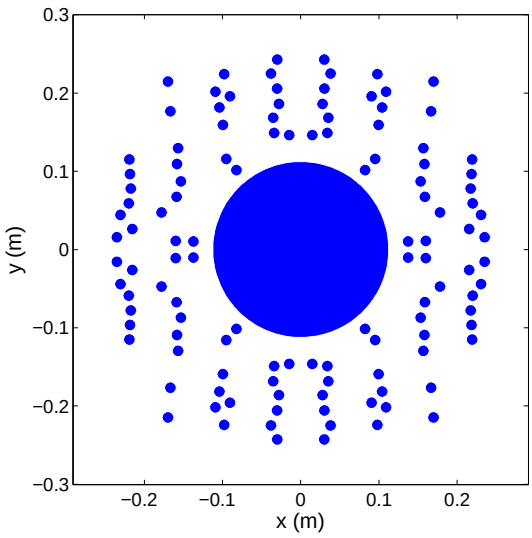


Figure 13.1: Distribution of 120 cylinders with radius 7.5 mm cloaking a central object with radius 11.25 cm. The positions of the cylinders have been calculated to render the structure invisible for waves at 3 kHz travelling along the $x$-axis.

## 13.2 Sample and experimental setup

The cloak is designed for 2D operation and therefore requires an experimental setup where waves only propagate in two dimensions. For this purpose, a 2D waveguide was specifically constructed. Figure 13.3 shows a photograph of the chamber. The top surface is built with wooden plates while the bottom is the floor of the laboratory. The chamber covers an area of $4.6 \times 3.66$ m$^2$ and its lateral boundaries are covered with a layer of fiber glass in order to avoid undesired reflections. The height of the waveguide is 5 cm, which results in single mode propagation until 3400 Hz where one-half wavelength equals this height. Above this cutoff frequency higher order modes with variations along the $z$-axis are excited, thus spoiling the experimental data. The propagating sound is generated by a JBL CBT100LA column speaker and introduced at the front side of the chamber. The sample is placed in the center of the chamber where a $68 \times 68$ cm$^2$ sample holder is located. The pressure field is measured through a B&K 4958 microphone attached to a 2D programmable robot. The data are acquired inside the chamber in an area of $75 \times 46$ cm$^2$ with a spatial resolution of 1 cm (see the blue area in Fig. 13.3).

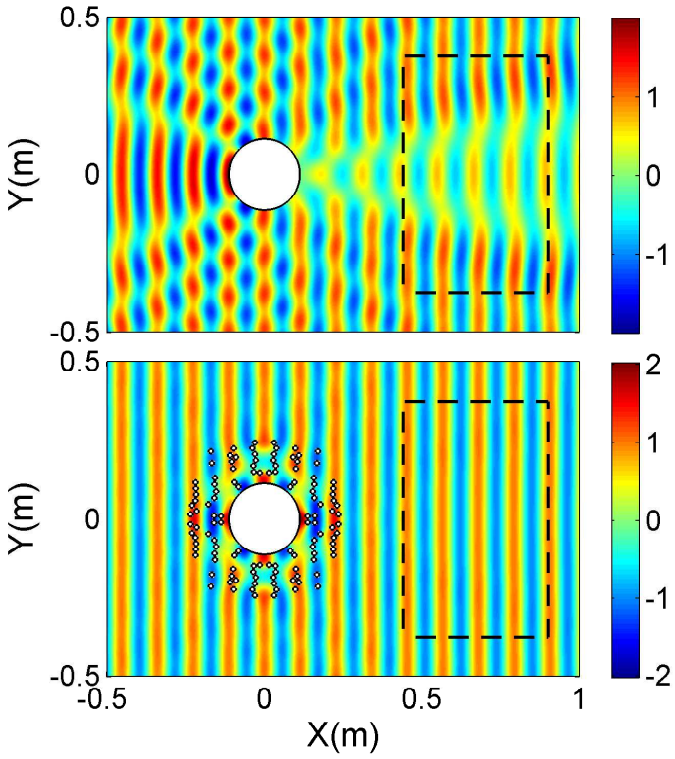


Figure 13.2: Real part of the total pressure field calculated for a bare cylinder with diameter 22.5 cm (upper panel) and the same object surrounded by the cloak depicted in Fig. 13.1. The impinging sound is a plane wave at 3 kHz coming from the left side of the figure. The rectangles defined by dashed lines define the area where the field is experimentally measured.

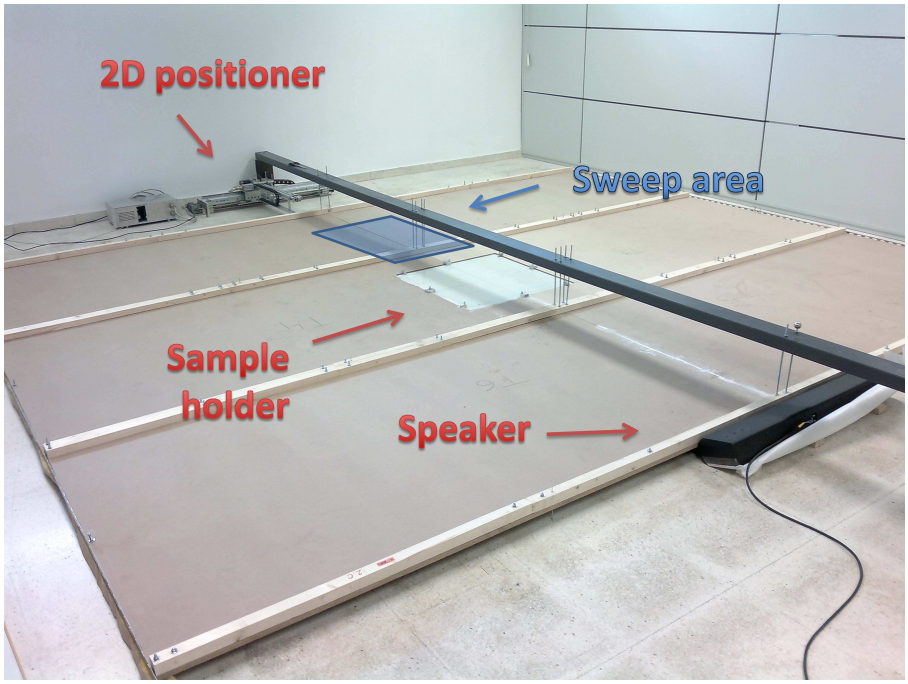


Figure 13.3: Experimental setup employed to characterize the samples in a 2D environment. It is built with a $4.6 \times 3.66$ m$^2$ wooden plate separated 5 cm from the floor of the room. A column speaker is placed at the front side of the chamber and excites a sound wave with a plane wavefront inside the waveguide. The samples are placed in a sample holder located in the center of the chamber and the sound is recorded on the blue area by means of a microphone moved with a 2D positioner.

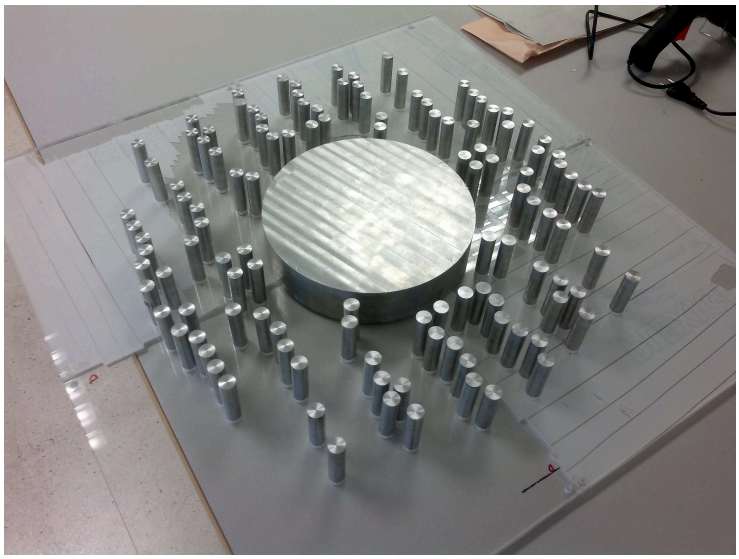

Figure 13.4: Photograph of the fabricated sample consisting of a central cylinder with radius 11.25 cm surrounded by a set of 120 cylinders with 1.5 cm of diameter. All the cylinders are fixed by a methacrylate plate with a distribution of holes drilled in accordance to the scheme of Fig. 13.1.

The cylinders shown in Fig. 13.1 have been built in aluminum, which is considered a rigid material for sound waves in air. The positions of the cylinders are fixed by means of a methacrylate plate where the holes have been drilled at their precise positions through a computer-controlled milling machine. The resulting structure can be observed in Fig. 13.4.

The excitation signal consists of a 3 kHz carrier modulated by a Gaussian envelope. It has a finite duration in order to acquire the response of the system until a specific time and avoid reflections coming from the limits of the waveguide. Despite the fiberglass absorbing layers included in the setup, these reflections can occur in the sides of the chamber where the speaker and the 2D positioner are placed. Several pulses are emitted at each position of the robot and the resulting data are averaged, processed through a Fourier transform and stored in a computer. All the process is managed by a custom LabVIEW program.

Excitation data is generated by a PCI-6731 card. The analog output of such a device goes to a power amplifier that drives the column speaker. The data received by the microphone are amplified by a B&K 2694-B and

digitized by a Pico Scope 3224. Since the behavior of the sample is wavelength sensitive, a rigorous control of the sound velocity was performed during the experiments. Temperature and humidity sensor were included in the system and these parameters were continuously acquired by the control software. The temperature sensor is based on a LM35 device while the humidity is measured with a HIH-4000-002 integrated circuit. These parameters were very stable along the time spent in data acquisition. The averaged values of temperature and relative humidity were 24.8°C and 54.7%, respectively, resulting in a sound speed of 347 m/s [WE85].

## 13.3 Results

The experiments were carried out for three cases: free space (i.e., empty waveguide), bare cylinder and cylinder surrounded by the cloak. The visibility factor $\gamma$ has been employed to quantify the performance of the cloaking. It is defined as [ZXF11]

$$\gamma = \frac{1}{N} \sum_{j} \frac{|P_{max,j}| - |P_{min,j}|}{|P_{max,j}| + |P_{min,j}|}, \tag{13.3.1}$$

where $P_{max,j}$ and $P_{min,j}$ are the maximum and minimum peak values along a given wavefront $j$. This parameter measures the stability of the wavefront reconstructed by the cloak and equals zero when the pressure amplitude takes the same value in each wavefront. The frequency response of the visibility $\gamma$ is shown in Fig. 13.5 for the three analysed cases. The measured data (symbols) are compared with numerical simulations obtained through the finite element method (lines). The operating frequency of the cloak corresponds to the point where $\gamma$ reaches a minimum. The experimental data corresponding to the cloak shows a minimum at 3061 Hz, which is a value slightly different from the frequency considered in the design process. This discrepancy can be explained by the difference between the sound velocity assumed in the calculations and its actual value inside the waveguide. As shown, at this frequency the visibility of the cloak is much lower than that of the bare cylinder and is very close to the free space, proving that the transparency of the object has been obtained. The behaviour of the cloak is narrowband and the performance decreases as frequency differs from the operating point. It

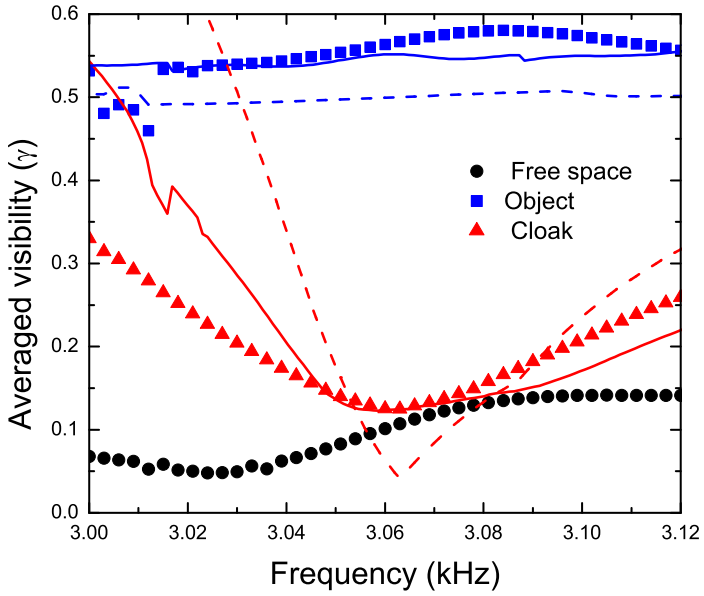


Figure 13.5: Averaged visibility as a function of the frequency for the free space (black), a rigid cylinder (blue) and a rigid cylinder surrounded by the designed cloak (red). The symbols represent results obtained from experimental data. Solid lines are obtained from finite element simulations with an incident plane wave while dashed lines result from simulations employing an incident sound profile fitted to that measured in the chamber.

is worth noting that the visibility of the free space is ideally zero. Although the measured value is not null, it is reasonably low.

The dashed lines in Fig. 13.5 represent simulations performed with a perfect plane wave as excitation source. However, the measured profile of the incident wave differs slightly from a plane wave. To account for this issue, the incident field has been modelled through the expression

$$P_{0,meas} = \frac{e^{-\left(\frac{y}{\sigma}\right)^2}}{(x+x_0)^n} e^{ikr}, \tag{13.3.2}$$

where

$$r = \sqrt{(x+x_{0r})^2 + y^2}. \tag{13.3.3}$$

The parameters of the above equations were obtained through a numerical

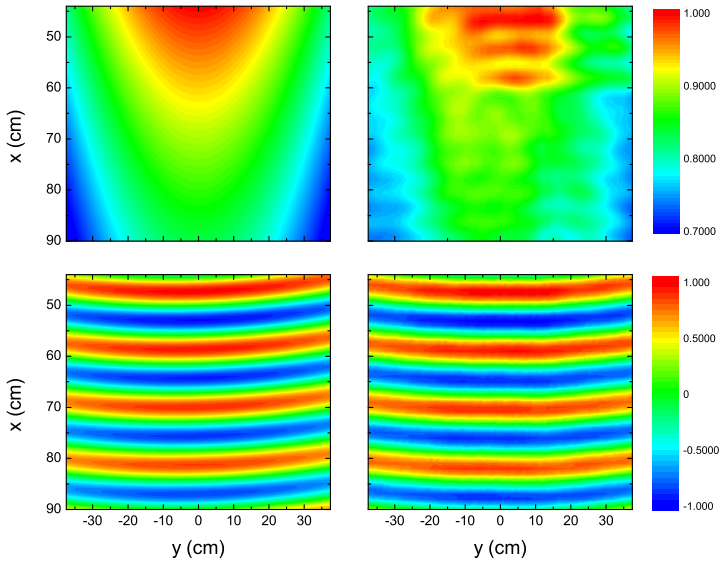


Figure 13.6: Amplitude (upper panels) and real part (lower panels) of the pressure within the region of exploration in the experimental setup. The right panels illustrate the measured data and the left panels show the field modelled through Eq. (13.3.2).

fitting with the measured data, giving $x_0 = 2.7$, $n = 1.16$, $\sigma = 0.83$ and $x_{0r} = 3.93$. A comparison between the measured and modelled fields within the region of exploration of the experimental setup is provided in Fig. 13.6. The simulations employing the fitted Gaussian beam are shown in Fig. 13.5 with solid lines. It is observed that the visibility factor calculated through this approach (continuous lines) results in a better agreement with the experimental data.

Figure 13.7 shows the real part (right panels) and the amplitude (left panels) of the pressure field measured at 3061 Hz for the three cases. The measured data of the free space is here included with the same color scale than the other cases in order to observe the pressure reduction when the object and the cloak are inserted in the chamber. The scattering of the cylinder clearly distorts the impinging wave and it is characterized by the shadow produced by the presence of a large rigid object. When the cylinder is surrounded by the cloak, the wavefronts are reconstructed and the amplitude of the waves

becomes practically uniform. These effects demonstrate the performance of the cloak. The maximum amplitude measured with the cloak is about 15% lower than that obtained for free space. This implies in principle the presence of losses associated to the cloak. However these losses are actually an artifact of the measurement procedure. The long time response of the cloak as a result of multiple scattering effects is not completely acquired and those components overlapped with the undesired echoes are discarded. Another source of absorption is given by the viscous losses that take place on the walls of the waveguide. This effect becomes more important inside the cloak where the field takes higher values.

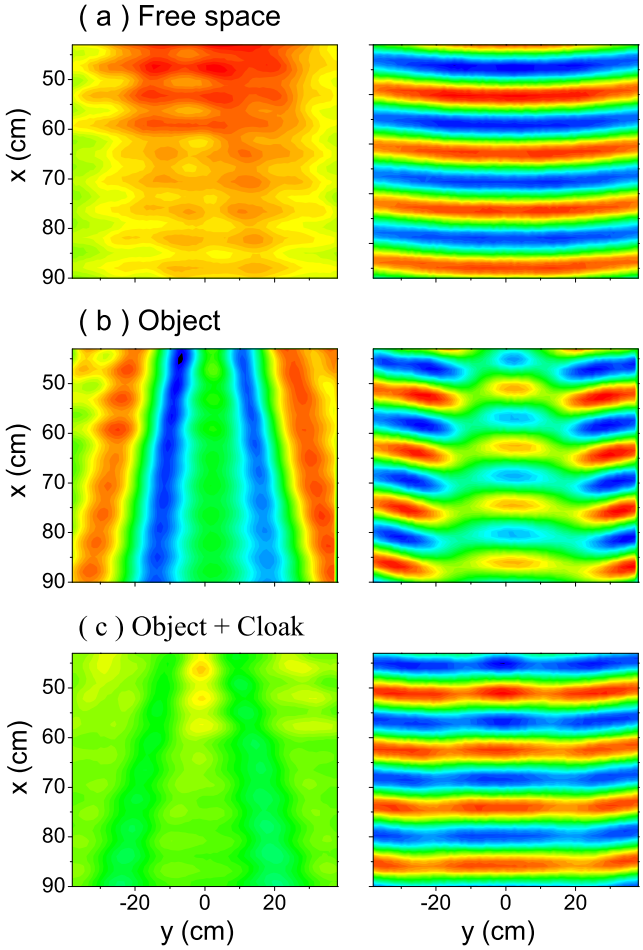


Figure 13.7: Pressure maps measured at 3061 Hz for the free space (upper panels), the bare cylinder (middle panels) and the cylinder with the cloak (lower panels). The left panels represent the amplitude of the pressure ($P$) and the right panels illustrate the real part ($P_r$). The color scale ranges from blue ($P = 0$, $P_r = -1$) to red ($P = 1$, $P_r = 1$).

# Chapter 14

# Three-dimensional cloak based on scattering cancellation

In the last chapter, a 2D acoustic cloak based on scattering cancellation was presented. The design of such a device was carried out through a numerical optimization which is also known as inverse design. The procedure developed for this purpose can be extended to account for new geometries and scenarios, resulting in a powerful tool for the practical realization of acoustic devices. In this chapter a 3D axis-symmetric cloak is implemented. The theoretical approach that leads to the definition of the objective function will be first provided. Then, the experimental characterization is described and finally the experimental results are shown and discussed.

## 14.1 Design

The proposed cloak is based on a specific distribution of concentric tori surrounding the cloaked object, which is a rigid sphere. The tori are also rigid and they all have the same transversal section. Their positions and major radii are determined through an optimization procedure similar to that presented in Chapter 13. It combines genetic algorithms and simulated annealing in order to deal with the huge search space of the problem. The process starts with the tori homogeneously distributed along the $z$-axis with their planes perpendicular to it. The cylindrical coordinates $(\rho_i, z_i)$ defining the major radius and position of each torus are obtained through successive

annealing steps while temperature decreases, as described in Section 13.1. The goal of this process is to cancel the field scattered by the sphere for sound waves travelling along the $z$-axis and whose wavelength is equal to the radius of the sphere ($\lambda = R_s$).

The design procedure requires an objective function that evaluates the performance of the cloaking. The computation of this function involves solving the direct problem, which consists of obtaining the field scattered by the sphere and the tori when an incident wave impinges on them. In order to efficiently perform these calculations, the method of fundamental solutions is here applied [SSRS86]. Taking into account the axial symmetry of the structure, the surfaces of the tori and the sphere can be discretized in a finite set of rings that lead to a system of linear equations describing the problem. Consider a plane wave propagating along the $z$-axis $P_0 = e^{ikz}$, where $k$ is the wavenumber in air. The total scattered pressure $P_s$ at the point $(\rho, z, \phi)$ can be expressed in cylindrical coordinates as the sum of $N$ virtual ring sources with amplitudes $\alpha_i$ and located at positions $(\rho_i, z_i)$:

$$P_s(\rho, z) = \sum_{i=1}^{N} \alpha_i G_{axis}(\rho, z; \rho_i, z_i), \tag{14.1.1}$$

where $G_{axis}$ is the free space axisymmetric Green's function of the Helmholtz equation, defined as [KF98]

$$G_{axis}(\rho, z; \rho_i, z_i) = \frac{1}{4\pi} \int_0^{2\pi} \frac{e^{ikR_i}}{R_i} d\phi_i. \tag{14.1.2}$$

The above integral is taken over the angular coordinate of the $j$-th ring source. The parameter $R_i$ is the distance between the points of the ring and the position where the field is calculated, then

$$R_i = \sqrt{(z - z_i)^2 + \rho^2 + \rho_i^2 - 2\rho\rho_i \cos(\phi_i - \phi)}. \tag{14.1.3}$$

The sphere and the tori are acoustically rigid and therefore the component of the velocity normal to their surfaces must be zero, that is,

$$\left. \frac{\partial P_t}{\partial n} \right|_{(\rho_i, z_i)} = 0, \tag{14.1.4}$$

where $P_t = P_0 + P_s$ is the total pressure field and $n$ indicates the normal to the surface at the points $(\rho_i, z_i)$. Taking into account Eq. (14.1.1) it follows

that

$$\left.\frac{\partial P_0}{\partial n}\right|_{(\rho_i,z_i)} + \sum_{i=1}^{N} \alpha_i \left.\frac{\partial G_{axis}}{\partial n}\right|_{(\rho_i,z_i)} = 0. \tag{14.1.5}$$

Equation (14.1.5) defines a linear system of coupled equations where the coefficients $\alpha_i$ are the unknowns. In practice the surface of each torus has been divided in $N_r = 15$ rings, while the sphere takes $N_s = 40$ rings. The number of equations of the system is therefore $N = N_r M + N_s$, where $M = 60$ is the number of tori in the cloak.

The objective function of the optimization procedure is expressed in terms of the scattering cross section $\sigma$ of the structure. To obtain this parameter the optical theorem is considered:

$$\sigma = \frac{4\pi}{k}\Im[f(0^\circ)], \tag{14.1.6}$$

where $f(0^\circ)$ is the far-field scattering amplitude at $\theta = 0^\circ$ and $\Im$ denotes imaginary part. The scattered field at large distances can be represented with a spherical wave as

$$P_s(r,\theta,\phi) = f(r,\theta,\phi)\frac{e^{ikr}}{r}. \tag{14.1.7}$$

Because of the axial symmetry of the structure and the impinging wave the far-field scattering amplitude can be expressed as $f(\theta = 0^\circ) = P_s z e^{ikz}$. Substituting $P_s$ by Eq. (14.1.1) and taking the limit $z \to \infty$ the scattering cross section is

$$\sigma = \frac{2\pi}{k}\Im\left[\sum_{i=1}^{N} \alpha_i e^{-ikz_i}\right]. \tag{14.1.8}$$

This expression allows an efficient calculation of the scattering cross section of any axisymmetric structure. From the scattering cross section of the bare sphere $\sigma_{sph}$ and the sphere surrounded by the arrangement of tori $\sigma_c$, the fitness function is calculated as

$$F = 1 - \frac{\sigma_c}{\sigma_{sph}}, \tag{14.1.9}$$

where $F = 1$ defines a perfect concealment of the system.

The cloak contains 60 tori surrounding a sphere with radius $R_s = 4$ cm. All the tori have a circular section whose radius is 26.7 mm. Since $\lambda = R_s$

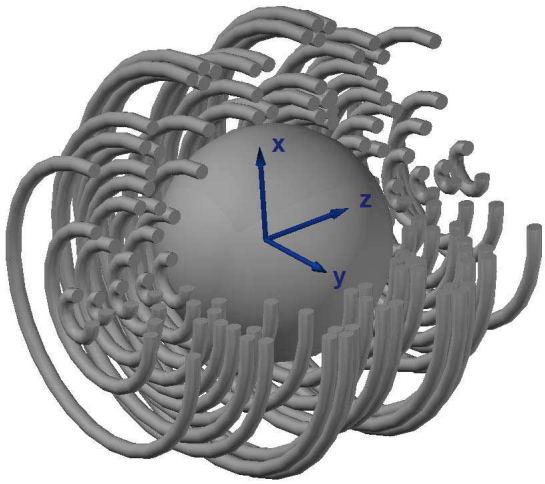


Figure 14.1: Schematic view of the designed 3D cloak. It consists of a rigid sphere with 4 cm of diameter surrounded by 60 tori whose major radii and positions are numerically optimized to conceal the whole structure.

the frequency of operation of the device is 8.62 kHz, where a sound speed of 344.8 m/s for a room temperature $T = 22°\text{C}$ has been assumed. The resulting structure after the optimization procedure is shown in Fig. 14.1. The distribution of tori is not uniform and, apart from the axial symmetry along the $z$-axis, mirror symmetry with respect to the $XY$ plane is also obtained. The fitness function of this optimum structure has a value of $F = 0.978$, which means a scattering cross section reduction of 97.8% with respect to that of the bare sphere.

The sphere with and without cloak has been simulated through the method of fundamental solutions. The corresponding field maps are shown in Fig. 14.2. The scattering of the bare sphere is observed in Fig. 14.2(a). In comparison with Fig. 13.2, it is observed that the scattering produced by a sphere is much weaker than that of a rigid cylinder. The region delimited with black dashed lines corresponds to the zone where the pressure is measured in the experimental characterization. The field within this area is mainly defined by the shadow of the rigid object and the diffraction along its boundaries. When the set of tori are added to the sphere (see Fig. 14.2(b)) the shadowing is almost completely restored. The wavefronts of the transmitted sound are reconstructed, resulting in a plane wave similar to the incident one. The

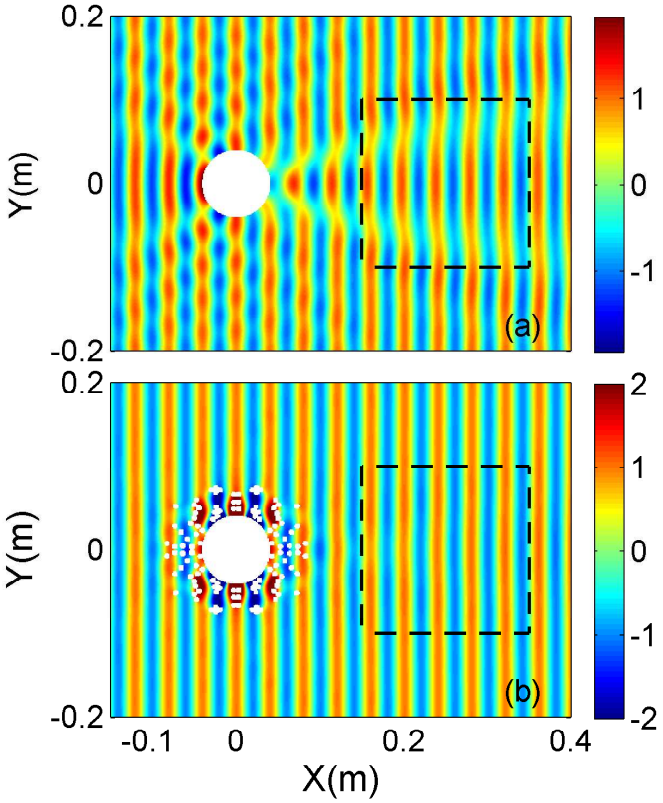


Figure 14.2: Pressure maps calculated for a plane wave at 8.62 kHz impinging on a bare sphere with 4 cm of radius (a) and the same sphere surrounded by the designed cloak (b). The rectangle defined by the dashed lines represents the area where the pressure field is experimentally acquired.

cloaking effect can be understood as a destructive interference between the waves scattered by the sphere and cloak. It is noticeable a strong accumulation of field pressure near the sphere surface in Fig. 14.2(b). It represents a resonant mode that appears as a consequence of the multiple scattering interference phenomenon.

The cloak performance has been characterized through the analysis of the ratio $\sigma_c/\sigma_{sph}$. Figure 14.3 illustrates the angular and frequency responses of this parameter. As shown, the designed device works for a narrow range of frequencies and angles of incidence. Defining the range of operation of the device as the region where the scattering reduction is higher than 70%, the

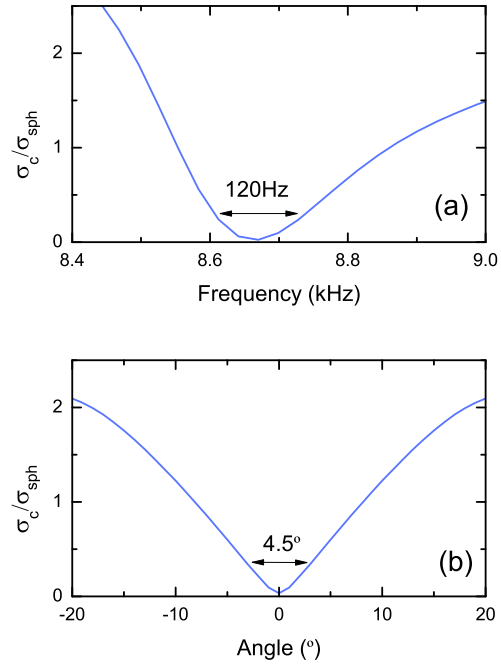


Figure 14.3: Frequency (a) and angular (b) responses of the ratio between the scattering cross section of the cloaked sphere $\sigma_c$ shown in Fig. 14.1 and that of a bare sphere $\sigma_{sph}$. A scattering reduction higher than 70% is achieved in a bandwidth of 120Hz for incident angles in the range $\pm 2.25°$.

bandwidth of the cloak is 120 Hz. With regard to the angle of incidence, the impinging wave should lie in the range $\pm 2.25°$ in order to provide an efficient concealment of the system.

Additional optimizations have been carried out to check the feasibility of our proposal at different design frequencies. Figure 14.4 shows optimized structures obtained by considering operating wavelengths of $\lambda = 2R_s$ and $R_s/2$. The sample under study (where $\lambda = R_s$) is included as a reference for comparison. A cloak based on a set of 60 rigid tori with the same minor radius has been considered in the three cases. It is observed in Fig. 14.4(a) that the performance of the cloaking is worse at high wavelengths due to the weaker scattering of the tori. In fact they are arranged in clusters whose elements are close together in order to deal with long waves. The fitness function of this case is $F = 0.421$, which is far from one and therefore the concealment

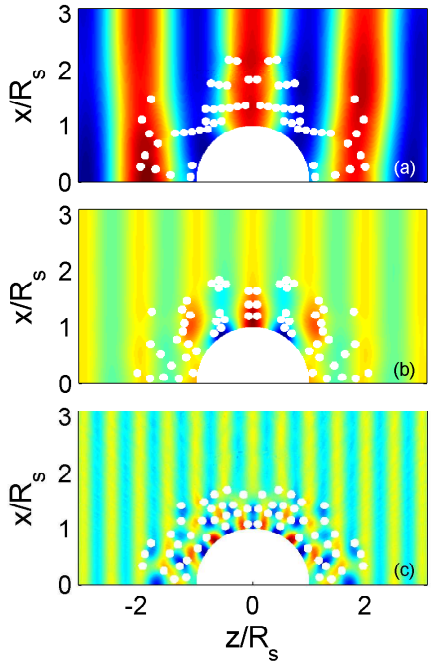


Figure 14.4: Pressure maps of a plane wave impinging on three cloaks designed to work with different wavelengths. The number of tori and their cross section is the same in the three cases. The design wavelengths are $\lambda = 2R_s$ (a), $R_s$ (b) and $R_s/2$ (c). The fitness function takes values of $F = 0.421$, 0.978 and 1.0, respectively.

is not efficient. On the other hand the structure optimized for $\lambda = R_s/2$ achieves a better performance, as shown in Fig. 14.4(c). The fitness function reaches $F = 1.0$, indicating a perfect concealment of the system. This effect occurs as a consequence of a higher interaction between the incident wave and the scatterers. Unlike the case for $\lambda = 2R_s$, it is observed that the tori are arranged in a more uniform distribution.

## 14.2 Sample and experimental setup

Due to the complexity of the design and the high accuracy required, the structure illustrated in Fig. 14.1 was constructed using a commercial 3D printer. The material employed by the printer is a thermoplastic polymer

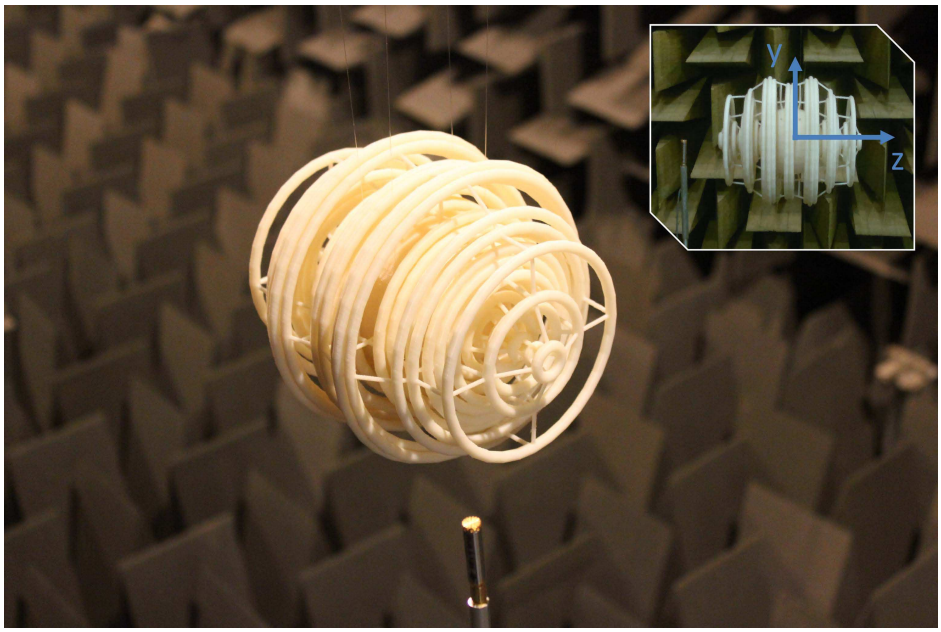


Figure 14.5: Photograph of the designed cloak after its fabrication. It is made in plastic with a sphere of radius 4 cm. The inset shows the coordinate axes of the experimental results. The total length of the sample along the $z$-axis is 17 cm.

(ABS), which can be considered acoustically rigid when dealing with airborne sound. The resulting sample is shown in Fig. 14.5. It is observed that the tori are interconnected through a set of thin beams that keep them at their calculated positions.

The experimental characterization was performed in an anechoic chamber with dimensions $8 \times 6 \times 3$ m$^3$. A photograph of the experimental setup is shown in Fig. 14.6. The sound excitation is provided through a JBL CBT100LA column speaker. According to the results of the previous section, the alignment between the direction of the incident sound and the sample is crucial. To accurately adjust the position and orientation of the sample, it was hung from angular and linear positioners that were attached to the ceiling of the chamber. The alignment with the speaker was carefully checked with a cross line laser level. The pressure field is scanned behind the sample along the $XZ$ (horizontal) and $YZ$ (vertical) planes according to the coordinate axes defined in the inset of Fig. 14.5. For this task two LTS300M linear

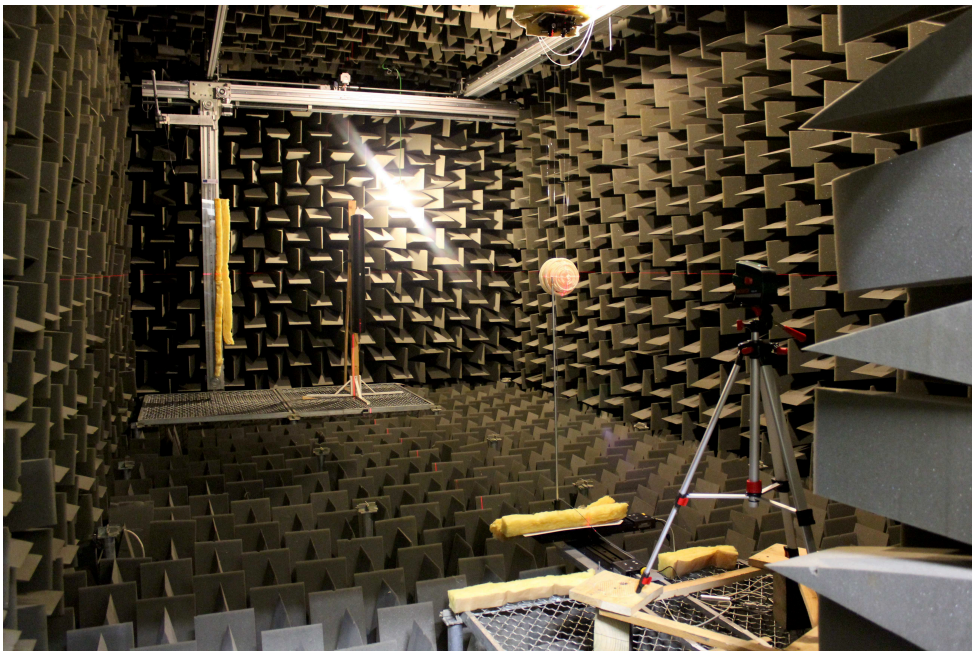

Figure 14.6: Photograph of the anechoic chamber where the experiments were carried out. A column speaker is placed at the back of the chamber and the sample is hung in front of it. Two linear stages move a microphone behind the sample in order to scan the pressure field.

stages where placed in the floor of the chamber. They move a B&K 4958 microphone over an area of $20 \times 20$ cm$^2$ with a spatial resolution of 5 mm. The region where the pressure field was measured is represented in Fig. 14.2 with black dashed lines.

A chirp with a frequency range from 7.5 to 9.5 kHz was used as the source signal. It is emitted at each spatial position of the moving robots until the pressure is acquired. The received signal is processed through a Fourier transform in order to obtain the amplitude and phase of the field. Several emissions are performed and the acquired responses are averaged to reduce the presence of random noise. The generation and acquisition of data was performed through a NI PXIe 6259 board controlled by a LabView program.

## 14.3 Results

The experimental procedure above described was applied to the three different cases: free space, bare sphere and sphere surrounded by the cloak. The cloaking performance has been measured through the averaged visibility $\gamma$ already employed in the previous chapter,

$$\gamma = \frac{1}{N} \sum_{j} \frac{|P_{max,j}| - |P_{min,j}|}{|P_{max,j}| + |P_{min,j}|}, \tag{14.3.1}$$

with $P_{max,j}$ and $P_{min,j}$ being the maximum and minimum amplitudes along a given wavefront $j$. The comparison of the three cases is shown in Fig. 14.7 for the two perpendicular planes where the field was scanned. The upper panels depict the visibility obtained from the measured data (symbols) and those derived in the same way from numerical calculations performed with the method of fundamental solutions (lines). In general it is observed that measured data follow fairly well the trend of the numerical simulations. The visibility of free space $\gamma_0$ is shown to be low although its non-null value indicates the existence of unwanted scattering events inside the chamber. They are mainly due to the presence of components of the experimental setup with dimensions of the order of the wavelength or higher. This is especially remarkable in the case of the $YZ$ plane, where one of the linear stages is placed vertically and therefore closer to the sample. The visibility of the sphere $\gamma_{sph}$ takes values higher than that of the free space as expected. These values are in turn lower than those found for a rigid cylinder in the last chapter, proving the weaker scattering of the sphere. The cloaked sphere shows a visibility $\gamma_c$ whose value reaches a minimum below the levels of the bare sphere and close to those of the free space. The optimum frequency is 8.55 kHz, which is very close to the value employed in the design procedure. The slight difference can be again explained through the difference between the actual sound velocity and the value assumed in the calculations.

The lower panels of Fig. 14.7 show a comparison between the experimentally determined ratio $\gamma_c/\gamma_{sph}$ (symbols) and the relation between the scattering cross sections $\sigma_c/\sigma_{sph}$ (black lines). Note that the visibilities are taken with respect to the reference visibility of the free space for a fair comparison. It is observed that the ratio $\gamma_c/\gamma_{sph}$ gives a good representation of $\sigma_c/\sigma_{sph}$ for the frequencies where the concealment of the cloaking sphere

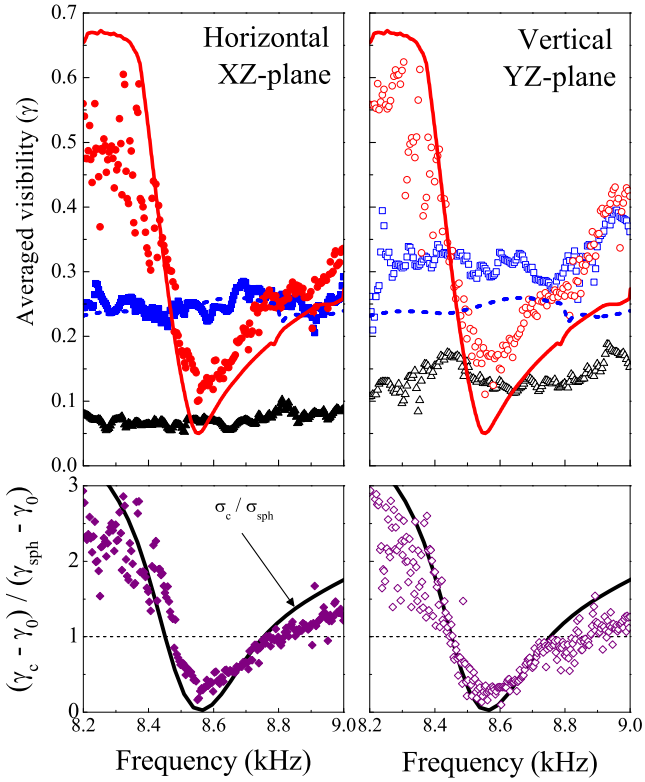


Figure 14.7: Upper panels: Averaged visibility $\gamma$ obtained from experimental data (symbols) and simulations (lines) as a function of the frequency. Results of the free space, bare sphere and cloaked sphere are represented with black triangles, blue squares and red circles, respectively. Lower panels: Frequency response of ratio between the scattering cross section of the sphere with and without cloak (lines). It is compared to the ratio between the cloak visibility $\gamma_c$ and the bare sphere $\gamma_{sph}$. Both parameters are shifted by the reference visibility of the free space $\gamma_0$ for proper comparison. Left and right panels show data of the horizontal ($XZ$) and vertical ($YZ$) planes, respectively.

occurs. These panels allow the evaluation of the cloaking performance and reveals that a 90% of maximum reduction of the sphere cross section is experimentally obtained.

The real part of the pressure field at 8.55 kHz is shown in Fig. 14.8. The left panels represent the field acquired on the horizontal plane while the right maps correspond to the vertical plane. The spectra taken in free space present some wiggling in the wave fronts that is originated from the aforementioned unwanted reflections in the equipment of the experimental setup. The pressure field measured with a bare sphere shows the shadowing by the diffracted sound, which is substantially smaller than that observed in a cylinder (see Fig. 13.7). Finally, it is observed in Fig. 14.8 that the cloak reconstructs the plane wavefronts but with the limitations already observed in the free space measure. It is important to remark that all the maps are represented with the same color scale, which means that no appreciable losses occur in the designed cloak.

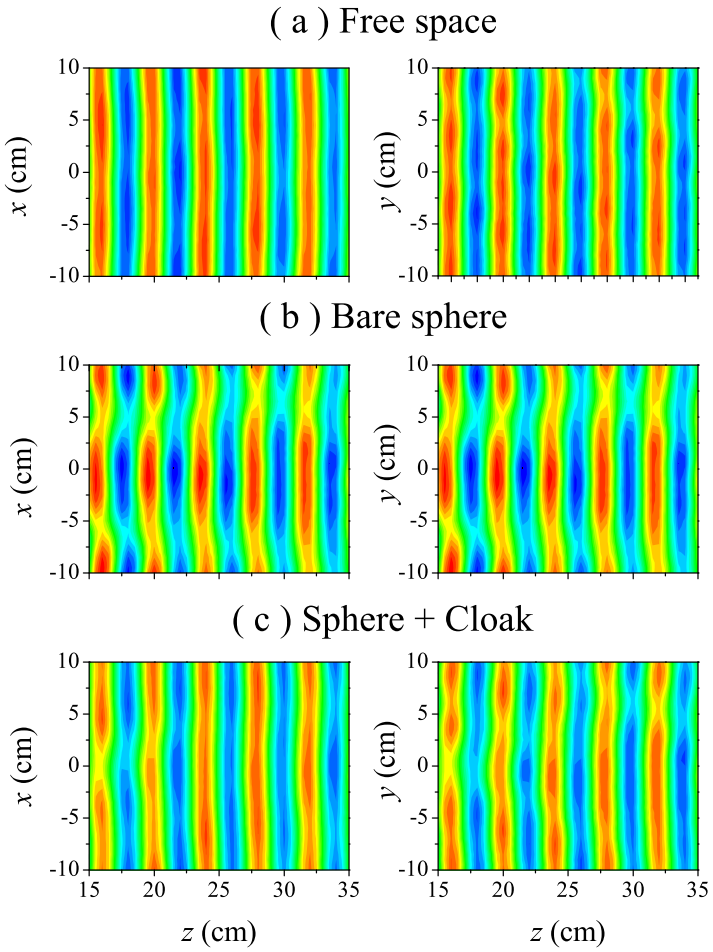


Figure 14.8: Maps on the left (right) represent the real part of the pressure measured at 8.55 kHz on the horizontal (vertical) plane for the cases of free space (a), bare sphere (b) and sphere surrounded by the cloak (c). The position of the scanned area relative to the sample is depicted in Fig. 14.2 as a rectangle defined by dashed lines.

# Concluding remarks

# Conclusions

This work reports the design of acoustic devices based on arrangements of scattering units. First, the use of sonic crystals as noise barriers for traffic noise control is considered. Although barriers based on rigid cylinders were initially proposed, these structures have proved to be inefficient since the acoustic band gaps are unable to attenuate a broadband and diffuse noise profile, as is the case of traffic noise. Because of this, the inclusion of absorbing materials in the scattering units is proposed. In a first step, barriers composed of cylinders containing a porous material have been analysed. A theoretical model based on the multiple scattering method and a microstructural approach that treats the porous material as an equivalent fluid is derived. Numerical calculations show a good agreement with experiments performed in different samples containing rubber crumb. It is found a remarkable improvement in the isolation characteristics of the structures, showing higher attenuation levels and bandwidths than those barriers made only with rigid cylinders.

In the next step, a more efficient absorber has been included in the design. Microperforated plates were considered in an effort to improve the previous results. A theoretical approach to describe scattering units based on cylindrical perforated shells has been developed. Experimental data as well as finite element simulations support this theoretical model which, in turn, has been able to predict the presence of Wood anomalies in lattices of shells with large perforations. The attenuation levels observed in the experimental samples greatly exceed those found in cylinders with rubber crumb.

An optimization procedure has been applied to obtain the geometric dimensions of noise barriers maximizing the attenuation of traffic noise. The performance of the barriers is measured through the $DL_R$ parameter defined in the European normative [EN 97]. An approach to calculate the transmission properties of sonic crystals under acoustic diffuse fields is provided. In addition, the presence of a second parallel barrier is also considered and in order to account for realistic schemes. When multiple reflections between two parallel barriers occurs, it is shown that only absorption mechanisms improve the attenuation of the barriers while reflectance is not effective. Values of $DL_R$ up to 18 dB and 24 dB are obtained when optimizing a single barrier

with a high filling fraction of cylinders made with rubber crumb and microperforated plates, respectively. It is worth noting that the developed models and tools are not restricted to traffic noise, but they are applicable to any source of noise through an appropriate definition of the objective function in the optimization procedure.

The development of acoustic cloaks has been the second goal of this PhD work. All the proposals are intended to work with airborne sound and are built with rigid materials. A reduced cloak designed through the theory of transformation acoustics is first shown. The temperature of the surrounding air is used as the physical mechanism providing sound speeds higher than that of the background. The cloak is composed of concentric layers of cylinders whose surfaces are heated or cooled to specific temperatures. Numerical calculations and finite element simulations of a cloak having 2646 cylinders distributed in 20 layers support the performance of the designed device. However some layers require extreme values of temperature, making the proposal hardly realizable in practice. In any case and apart from cloaking, the control of the temperature profiles result in an interesting tool for the design of acoustic metamaterials.

Acoustic cloaks based on scattering cancellation have been also considered. A 2D cloak composed of 120 cylinders surrounding a central object has been developed through this technique. The positions of the scatterers are calculated through the combination of two types of algorithms: genetic algorithms and simulated annealing. The resulting structure is able to conceal a cylinder from sound waves with a specific wavelength and coming from a given direction. This fact was experimentally demonstrated with a 22.5 cm-diameter cylinder in a 2D waveguide. It was been shown that this approach can be extended to the third dimension. With this purpose a cloak based on a distribution of 60 tori surrounding a rigid sphere has been implemented. The major radii and positions of the tori are calculated with a optimization procedure similar to that used for the 2D case. The performance of the device was demonstrated through an experimental characterization with a sphere with 4 cm of radius surrounded by the designed cloak.

# Future work

The study about noise control presented in this work can be extended to account to more effects than may reduce the performance of the barriers. Air flow or nonlinearities have been disregarded in the analysis of microperforated shells and it would be interesting to assess their contribution to the attenuation properties of the barriers. Diffraction by the border of the cylinders can also be taken into account. In addition, the optimization procedure can be modified with new improvements. For example, the cost of the materials can be included in the calculations. This would avoid the convergence to expensive solutions whose attenuation is close to a cheaper choice. In addition it would allow setting a maximum cost per meter for the resulting barrier as a design constraint. As concluded in Section 9.3, the parameters of the perforations strongly influence the attenuation spectrum of the barriers. The optimization of these parameters could be introduced in the optimization tool, although this requires fabrication processes capable of drilling holes with variable dimensions. Finally, new topologies can be considered for the scattering units. An interesting example consists of partitioning the interior of a microperforated shell in different sections. Thus, the advantages reported by Toyoda and Takahashi in microperforated panels with subdivided air cavities can be here achieved [TT08].

With regard to acoustic cloaking, the future issues to solve are related to the frequency and angular responses of the devices. The practical implementation of broadband and omnidirectional devices is a topic of intense research. Higher bandwidths can be obtained through multi-objective optimizations where the fitness function is averaged along a given frequency range. The bandwidths usually obtained from the optimization procedure used in this work are quite narrow, and care should be taken with results showing comb-like spectra instead of continuous profiles. The omnidirectional behavior should be achieved by arranging the scattering elements uniformly in all directions. In any case more complex scatterers than those employed in this work should be considered to improve the convergence towards satisfactory solutions. Inspired by the hybrid cloak reported by Martin and coworkers [MO12], the two developed techniques (scattering cancellation and temperature control) can be combined. Extreme temperature profiles are

only required in those layers close to the central object and therefore they can implemented with a scattering cancellation shell. The approaches shown in this work can be also applied to underwater acoustics. In this case, the elastic parameters of the materials of the the scattering units must be considered. This provides more degree of freedom and can be taken into advance to achieve omnidirectional and/or broadband acoustic cloaks.

# Appendix

# Appendix A

# Calculation of T matrix through finite element method

## A.1 Introduction

As shown in Chapter 2, the theoretical expression of the T matrix of a given scatterer is theoretically obtained by applying boundary conditions at each interface between two media. This procedure is relatively simple to perform in cylinders with circular and invariant section made with isotropic fluids. However when considering more complicated schemes the deduction of the T matrix becomes complex and it is useful to verify the theoretically derived expressions with an alternative tool. In this sense the finite element method (FEM) proves to be a powerful tool since it is capable of simulating complex structures. In this appendix, the FEM will be employed to compute the T matrix of a generic cylinder.

As shown in Section 2.2, the incident pressure field can be expressed as

$$P_i = \sum_{q=-\infty}^{\infty} A_q^0 J_q(k_0 r) e^{iq\theta}, \tag{A.1.1}$$

and the scattered field as

$$P_s = \sum_{q=-\infty}^{\infty} A_q H_q(k_0 r) e^{iq\theta}. \tag{A.1.2}$$

If the scatterer is supposed to have circular section, its T matrix becomes

diagonal. Thus the diagonal elements are defined by the relation

$$T_q = \frac{A_q}{A_q^0}. \tag{A.1.3}$$

By applying a cylindrical incident field for a given order $q$ with the form $P_{i,q} = J_q(k_0 r)e^{iq\theta}$ the scattered field becomes $P_{s,q} = T_q H_q(k_0 r)e^{iq\theta}$ since $A_q^0 = 1$. Therefore the T matrix can be directly extracted from the scattered field obtained by the simulation as

$$T_q = \frac{P_{s,q}}{H_q(k_0 r)e^{iq\theta}}. \tag{A.1.4}$$

Although a circular section is here assumed, it is worth to note that this condition can be relaxed. The calculations can be extended to scatterers with a section circular on average, i.e., with a section having subwavelength structures whose effects can be homogenized at low enough frequencies. This is the case of the perforated cylinder computed in Section 7.3. The presented method has been also employed in the verification of the expressions developed for 3D scatterers embedded in a waveguide [GCGST$^+$12,GSGCTSD13].

## A.2 Procedure

Consider an unknown scatterer with external radius $R$. It should be properly modeled on a FEM environment according to its structure and material properties. A concentric cylindrical shell with external radius $R_{ext}$ should be included to model the background medium. A scheme of the simulations domains is depicted in Figure A.1. The impinging wave $P_{i,q}$ is configured at $R_{ext}$ in either a circumference (in 2D simulations) or a cylindrical surface (in 3D simulations). It is important to mesh adequately this zone, as well as each interface between two media, in order to obtain reliable results. When the geometry and acoustic parameters of the system are described, a frequency sweep is performed. At each frequency the elements of the T matrix are obtained from Eq. (A.1.4) for the different orders $q$ considered. Any point of the background shell can be used to compute the T matrix, although it is recommended to extract the data from $r = R_{ext}$ because of the better meshing of this boundary and the possible presence of evanescent modes coming from subwavelength elements in the surface of the scatterer. Moreover multiple points can be selected and averaged.

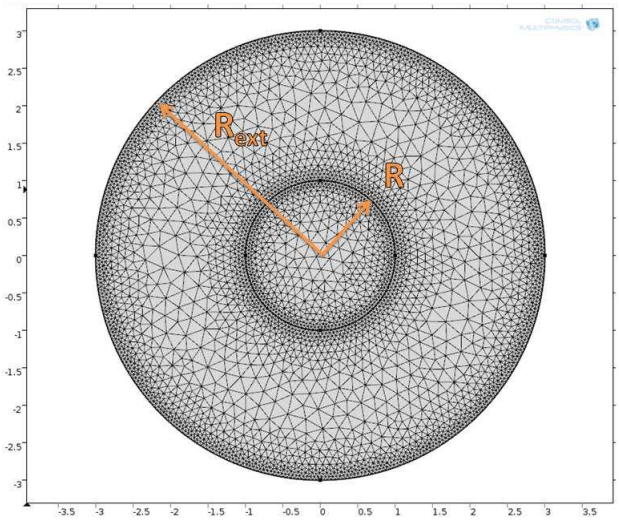


Figure A.1: Scheme of a simulation intended to compute the T matrix of a scatterer of radius $R$. The shell defined between radii $R$ and $R_{ext}$ contains the background medium.

## A.3 Example

A test of the method presented has been carried out with a rigid cylinder, which is a simple scatterer whose behavior is well-known. The expression of its T matrix can be found in Eq. (2.2.16). The radius of the simulated cylinder is $R = 4$ cm and the shell modeling the background has an external radius $R_{ext} = 8$ cm. A comparison between the theoretical and simulated data is shown in Fig. A.2 for $q = 0, 1, 2$. It is noticeable that both cases are practically overlapped, thus giving support to the developed procedure. The slight difference between the curves increases with the frequency due to the increasing distance between the mesh elements relative to the wavelength. Obviously the problem is fixed by adding more elements to the mesh, although the computational complexity of the problem will be higher. It is found that the accuracy of the method depends strongly on the density of elements, especially at the boundaries.

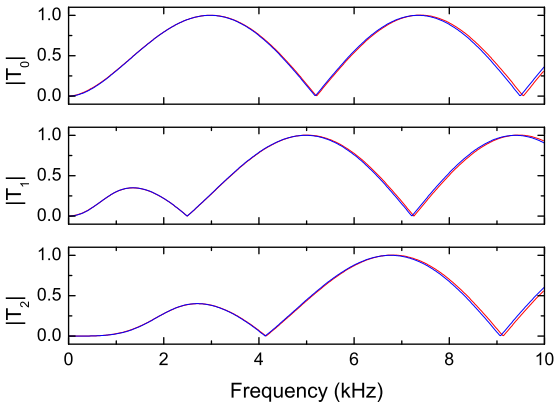


Figure A.2: Amplitude of the T matrix ofa rigid cylinder with radius 4 cm embedded in a background media with radius 8 cm for the orders $q = 0, 1, 2$. Blue lines correspond to theoretical calculations through Eq. (2.2.16) while red lines are the data extracted from the finite element simulations.

# Appendix B

# Publications

## B.1 Articles directly related with this PhD work

1. J. Sánchez-Dehesa, V. M. García-Chocano, D. Torrent, F. Cervera, S. Cabrera and F. Simón, *Noise control by sonic crystal barriers made of recycled materials*, J. Acoust. Soc. Am. 129, pp. 1173-1183, 2011.

2. V. M. García-Chocano, L. Sanchis, A. Díaz-Rubio, J. Martínez-Pastor, F. Cervera, R. Llopis-Pontiveros and J. Sánchez-Dehesa, *Acoustic cloak for airborne sound by inverse design*, Appl. Phys. Lett. 99, 074102, 2011.

    - Work highlighted in Physics New Highlights (AIP, August 2011).
    - Work reviewed in national newspapers and international scientific magazines.

3. V. M. García-Chocano and J. Sánchez-Dehesa, *Broadband sound absorption by lattices of microperforated cylindrical shells*, Appl. Phys. Lett. 101, 184101, 2012.

4. V. M. García-Chocano, D. Torrent and J. Sánchez-Dehesa, *Reduced acoustic cloaks based on temperature gradients*, Appl. Phys. Lett. 101, 084103, 2012.

5. V. M. García-Chocano and J. Sánchez-Dehesa, *Optimum control of broadband noise by arrays of cylindrical units made of a recycled material*, Appl. Acoust. 74, pp. 58-62, 2013.

6. L. Sanchis, V. M. García-Chocano, R. Llopis-Pontiveros, A. Climente, J. Martínez-Pastor, F. Cervera and J. Sánchez-Dehesa, *Three-dimensional axisymmetric cloak based on the cancellation of acoustic scattering from a sphere*, Phys. Rev. Lett. 110, 124301, 2013.

   - Selected as journal cover.
   - Work highlighted in Science Editor's Choice (Science 340, p. 121, 2013).
   - Work reviewed in national newspapers and international scientific magazines.

7. V. M. García-Chocano and J. Sánchez-Dehesa, *Anomalous sound absorption in lattices of cylindrical perforated shells*, Appl. Phys. Lett. 106, 124104, 2015.

## B.2 Articles in related topics

1. T. Elnady, A. Elsabbagh, W. Akl, O. Mohamady, V. M. García-Chocano, D. Torrent, F. Cervera and J. Sánchez-Dehesa, *Quenching of acoustic bandgaps by flow noise*, Appl. Phys. Lett. 94, 134104, 2009.

2. V. M. García-Chocano, T. López-Ríos, A. Krokhin and J. Sánchez-Dehesa, *Resonant excitation of coupled Rayleigh waves in a short and narrow fluid channel clad between two identical metal plates*, AIP Adv. 1, 041501, 2011.

3. V. M. García-Chocano, R. Graciá-Salgado, D. Torrent, F. Cervera and J. Sánchez-Dehesa, *Quasi-two-dimensional acoustic metamaterial with negative bulk modulus*, Phys. Rev. B 85, 184102, 2012.

4. V. M. García-Chocano, Nagaraj, T. López-Ríos, L. Gumen, J. Sánchez-Dehesa and A. Krokhin, *Resonant coupling of Rayleigh waves through a*

*narrow fluid channel causing extraordinary low acoustic transmission*, J. Acoust. Soc. Am. 132, pp. 2807-2815, 2012.

5. R. Graciá-Salgado, V. M. García-Chocano, D. Torrent and J. Sánchez-Dehesa, *Negative mass density and $\rho$-near-zero quasi-two-dimensional metamaterials: Design and applications*, Phys. Rev. B 88, 224305, 2013.

6. V. M. García-Chocano, J. Christensen and J. Sánchez-Dehesa, *Negative Refraction and Energy Funneling by Hyperbolic Materials: An Experimental Demonstration in Acoustics*, Phys. Rev. Lett. 112, 144301, 2014.

    - Work highlighted in Advances in Engineering.

7. M. D. Guild, V. M. García-Chocano, W. Kan and J. Sánchez-Dehesa, *Enhanced inertia from lossy effective fluids using multi-scale sonic crystals*, AIP Adv. 4, 124302, 2014.

8. M. D. Guild, V. M. García-Chocano, W. Kan and J. Sánchez-Dehesa, *Acoustic metamaterial absorbers based on multilayered sonic crystals*, J. Appl. Phys. 117, 114902, 2015.

9. A. Bozhko, V. M. García-Chocano, J. Sánchez-Dehesa and A. Krokhin, *Redirection of sound in straight fluid channel with elastic boundaries*, Phys. Rev. B 91, 094303, 2015.

10. W. Kan, V. M. García-Chocano, F. Cervera, B. Liang, X. Zou, L. Yin, J. Cheng and J. Sánchez-Dehesa, *Broadband acoustic cloaking within an arbitrary hard cavity*, Phys. Rev. Appl. 3, 064019, 2015.

## B.3 International Meetings and Conferences

1. J. Sánchez-Dehesa, V. M. García-Chocano, D. Torrent, F. Cervera and S. Cabrera, *Noise barriers based on recycled materials*, 157th Meeting of the Acoustical Society of America, Portland (U.S.A.), 2009. *

2. J. Sánchez-Dehesa, V. M. García-Chocano, D. Torrent, F. Cervera, S. Cabrera and F. Simón, *Noise attenuation by two-dimensional sonic crystals made of rubber crumb*, 159th Meeting of the Acoustical Society of America, Baltimore (U.S.A.), 2010. *

3. V. M. García-Chocano, J. Sánchez-Dehesa, D. Torrent, F. Cervera and S. Cabrera, *Noise control by absorptive sonic crystals*, 17th International Congress on Sound and Vibration, Cairo (Egipt), 2010. *

4. J. Sánchez-Dehesa, V. M. García-Chocano, D. Torrent, F. Cervera and S. Cabrera, *Noise attenuation by phononic crystals made of recycled materials*, 160th Meeting of the Acoustical Society of America, Cancun (Mexico), 2010. (**Invited Talk**). *

5. A. Krokhin, V. M. Garcá-Chocano, J. Sánchez-Dehesa, T. López-Ríos, *Narrow fluid channel as a metamaterial sound absorber*, 1st International Conference on Phononic Crystals, Metamaterials and Optomechanics, Santa Fe (Mexico), 2011.

6. V. M. García-Chocano and J. Sánchez-Dehesa, *Attenuation of broadband noise by sonic crystal barriers made of absorptive materials*, 4th Young Scientific Meeting on Metamaterials, Valencia (Spain), 2011. *

7. V. M. García-Chocano, S. Cabrera and J. Sánchez-Dehesa, *Noise attenuation by sonic crystal barriers made of microperforated units*, 163th Meeting of the Acoustical Society of America, Hong Kong (China), 2012. *

8. J. Sánchez-Dehesa, V. M. García-Chocano, R. Graciá-Salgado, F. Cervera and D. Torrent, *Acoustic metamaterials with negative parameters: a multiple scattering approach with examples*, 163th Meeting of the Acoustical Society of America, Hong Kong (China), 2012. (**Invited Talk**).

9. V. M. García-Chocano, R. Graciá-Salgado, F. Cervera, D. Torrent andJ. Sánchez-Dehesa, *A quasi two-dimensional acoustic metamaterial with negative bulk modulus*, 3rd International Conference on Metamaterials, Photonic Crystals and Plasmonics, Paris (France), 2012. (**Invited Talk**).

10. J. Sánchez-Dehesa, V. M. García-Chocano and D. Torrent, *Acoustic and elastic metamaterials*, 6th International Congress on Advanced Electromagnetic Materials in Microwaves and Optics, San Petersburgo (Rusia), 2012. *

11. J. Sánchez-Dehesa, V. M. García-Chocano and D. Torrent, *Reduced acoustic cloack based on temperature control*, 6th International Congress on Advanced Electromagnetic Materials in Microwaves and Optics, San Petersburgo (Rusia), 2012. *

12. J. Sánchez-Dehesa, V. M. García-Chocano, A. Climente, F. Cervera, L. Sanchis, R. Llopis-Pontiveros and J. Martínez-Pastor, *Experimental demonstration of a three-dimensional acoustic cloak based on a cancelation effect*, 165th Meeting of the Acoustical Society of America, Montreal (Canada), 2013. *

13. V. M. García-Chocano, R. Graciá-Salgado, D. Torrent and J. Sánchez-Dehesa, *Negative and density-near-zero acoustic metamaterials based on quasi-two-dimensional phononic crystals*, 165th Meeting of the Acoustical Society of America, Montreal (Canada), 2013.

14. J. Sánchez-Dehesa, F. Cervera, V. M. García-Chocano, R. Graciá-Salgado and D. Torrent, *Advances in acoustic cloaking and metamaterials with negative parameters*, 2nd International Conference on Phononic Crystals/Metamaterials, Sharm El-Sheikh (Egypt), 2013. *

15. F. Cervera, V. M. García-Chocano, A. Climente, J. Sánchez-Dehesa, V. Gómez-Lozano, L. Sanchis, R. Llopis-Pontiveros and J. Martínez-Pastor, *Demostración experimental de un cloak 3D unidireccional basado en la cancelación del campo acústico difractado por una esfera*, XXXIV Reunión Bienal de la Real Sociedad Española de Física, Valencia (Spain), 2013. *

16. V. M. García-Chocano, S. Cabrera, J. Sánchez-Dehesa, *Atenuación de ruido de banda ancha mediante barreras acústicas basadas en cristales sónicos*, XXXIV Reunión Bienal de la Real Sociedad Española de Física, Valencia (Spain), 2013. *

17. J. Sánchez-Dehesa, V. M. García-Chocano, D. Torrent, A. Díaz-Rubio, A. Climente, F. Cervera, *Acoustic cloaks for airborne sound*, International Symposium on the Theory and Application of Artificial Periodic Structures, Changsha (China), 2013. *

18. J. Sánchez-Dehesa, D. Torrent and V. M. García-Chocano, *Acoustic cloaks for airborne sound: Experimental realizations in two- and three-dimensions*, Special Topics on Transport Theory: Electrons, Waves and Diffusion in Confined Systems, Mexico City (Mexico), 2013. *

19. V. M. García-Chocano, F. Cervera, A. Díaz-Rubio, A. Climente, D. Torrent and J. Sánchez-Dehesa, *Acoustic cloaking for airborne sound based on inclusions of rigid scatterers*, 166th Meeting of the Acoustical Society of America, San Francisco (U.S.A.), 2013. (**Invited Talk**). *

20. J. Sánchez-Dehesa, V. M. García-Chocano and M. D. Guild, *Recent results on sonic crystals for sound guiding and acoustic absorption*, 168th Meeting of the Acoustical Society of America, Indianapolis (U.S.A.), 2014. (**Invited Talk**).

21. M. D. Guild, V. M. García-Chocano, W. Kan and J. Sánchez-Dehesa, *Acoustic metamaterial absorbers based on multi-scale sonic crystals*, 168th Meeting of the Acoustical Society of America, Indianapolis (U.S.A.), 2014. (**Invited Talk**).

22. J. Sánchez-Dehesa, V. M. García-Chocano, W. Kan and M. D. Guild, *Recent results on hyperbolic materials and sonic crystals*, 8th International Congress on Advanced Electromagnetic Materials in Microwaves and Optics, Copenhagen (Denmark), 2014. (**Invited Talk**).

23. D. Torrent, V. M. García-Chocano, R. Graciá-Salgado, F. Cervera and J. Sánchez-Dehesa *Quasi-two-dimensional acoustic metamaterials*, Photonic and Phononic Properties of Engineered Nanostructures V, San Francisco (U.S.A.), 2015. (**Invited Talk**).

24. V. M. García-Chocano and J. Sánchez-Dehesa *Absorption enhancement by lattice of perforated shells*, VI Taller sobre Metamateriales, Cristales Fotónicos, Cristales Fonónicos y Estructuras Plasmónicas, San Miguel de Allende (Mexico), 2015. *

25. V. M. García-Chocano, F. Cervera, S. Cabrera and J. Sánchez-Dehesa *Acoustic barriers based on lattices of absorptive cylinders*, Noise and Vibration - Emerging Technologies, Dubrovnik (Croatia), 2015. *

26. J. Sánchez-Dehesa and V. M. García-Chocano *Sound redirection and absorbing properties of lattices of perforated shells*, International Congress on Ultrasonics, Metz (France), 2015. *

27. V. M. García-Chocano and J. Sánchez-Dehesa *Sound propagation through lattices of perforated shells*, 3rd International Conference on Phononic Crystals, Metamaterials, Phonon Transport and Phonon Coupling, Paris (France), 2015. *

# Bibliography


[AA93] J. F. Allard and N. Atalla. *Propagation of sound in porous media*. Elsevier Applied Science, London, 1993.

[AÅ11] S. Allam and M. Åbom. A new type of muffler based on microperforated tubes. *J. Vib. Acoust.*, 133:031005, 2011.

[AC92] J. F. Allard and Y. Champoux. New empirical equations for sound propagation in rigid frame fibrous materials. *J. Acoust. Soc. Am.*, 91:3346–3353, 1992.

[ADN+90] J. F. Allard, C. Depollier, J. Nicolas, W. Lauriks, and A. Cops. Proprietés acoustiques des matériaux saturés d'air et théorie de biot. *J. Acoust.*, 3:29–38, 1990.

[AE05] A. Alù and N. Engheta. Achieving transparency with plasmonic and metamaterial coatings. *Phys. Rev. E*, 72:016623, 2005.

[AE08] A. Alù and N. Engheta. Plasmonic and metamaterial cloaking: physical mechanisms and potentials. *J. Opt. A*, 10:093002, 2008.

[ALK88] J. D. Achenbach, Y. C. Lu, and M. Kitahara. 3D reflection and transmission of sound by an array of rods. *J. Sound Vib.*, 125:463–476, 1988.

[AM76] N.W. Ashcroft and N.D. Mermin. *Solid State Physics*, section 9, pages 151–211. Saunders, 1976.

[AP07] F. Asdrubali and G. Pispola. Properties of transparent sound-absorbing panels for use in noise barriers. *J. Acoust. Soc. Am.*, 121:214–221, 2007.

[Att83] K. Attenborough. Acoustical characteristics of rigid fibrous absorbents and granular materials. *J. Acoust. Soc. Am.*, 73:785–799, 1983.

[BAOSD03] J. Bravo-Abad, T. Ochiai, and J. Sánchez-Dehesa. Anomalous refractive properties of a two-dimensional photonic band-gap prism. *Phys. Rev. B*, 67:115116, 2003.

[BDJ07] M. Baulac, J. Defrance, and P. Jean. Optimization of multiple edge barriers with genetic algorithms coupled with a nelder-mead local search. *J. Sound Vib.*, 300:71–87, 2007.

[BDJ08] M. Baulac, J. Defrance, and P. Jean. Optimisation with genetic algorithm of the acoustic performance of T-shaped noise barriers with a reactive top surface. *Appl. Acoustics*, 69:332–342, 2008.

[Ber86] L. L. Beranek. *Acoustics*. Acoustical Society of America, New York, 1986.

[Bio56a] M. A. Biot. Theory of propagation of elastic waves in a fluid-saturated porous solid. I. low frequency range. *J. Acoust. Soc. Am.*, 28:168–178, 1956.

[Bio56b] M. A. Biot. Theory of propagation of elastic waves in a fluid-saturated porous solid. II. higher frequency range. *J. Acoust. Soc. Am.*, 28:179–191, 1956.

[BME02] N. K. Batra, P. Matic, and R. K. Everett. Sonic crystal composites for selective noise reduction. *IEEE Ultrasonics Symposium*, pages 547–550, 2002.

[Bre80] L. M. Brekhovskikh. *Waves in layered media*, section 1.3, pages 15–21. Saunders, 1980.

[Bro80] R. J. S. Brown. Connection between formation factor for electrical resistivity and fluid-solid coupling factor in Biot's equations for acoustic waves in fluid-filled media. *Geophysics*, 45:1269–1275, 1980.

[CB80a] J. Y. Chung and D. A. Blaser. Transfer function method of measuring in-duct acoustic properties. I. theory. *J. Acoust. Soc. Am.*, 68:907–913, 1980.

[CB80b] J. Y. Chung and D. A. Blaser. Transfer function method of measuring in-duct acoustic properties. II. experiment. *J. Acoust. Soc. Am.*, 68:914–921, 1980.

[CHCW95] D. H. Crombie, D. C. Hothersall, and S. N. Chandler-Wilde. Multiple-edge noise barriers. *J. Sound Vib.*, 44:353–367, 1995.

[CL90] D. C. Cullen and C. R. Lowe. A direct surface plasmon-polariton immunosensor: preliminary investigation of the non-specific adsorption of serum components to the sensor surface. *Sens. Actuators B*, 1:576–579, 1990.

[Cra26] I. B. Crandall. *Theory of vibration system and sound*, pages 229–241. D. Van Nostrand, New York, 1926.

[CS92] Y. Champoux and M. R. Stinson. On acoustical models for sound propagation in rigid frame porous materials and the influence of shape factors. *J. Acoust. Soc. Am.*, 92:1120–1131, 1992.

[CS07] S. A. Cummer and D. Schurig. One path to acoustic cloaking. *New J. of Phys.*, 9:45, 2007.

[CSA12] P. Y. Chen, J. Soric, and A. Alù. Invisibility and cloaking based on scattering cancellation. *Adv. Opt. Mat.*, 24:281–304, 2012.

[CSDR+99] D. Caballero, J. Sánchez-Dehesa, C. Rubio, R. Martínez-Sala, J. V. Sánchez-Perez, F. Meseguer, and J. Llinares.

Large two-dimensional sonic band gaps. *Phys. Rev. E*, 60:R6316–R6319, 1999.

[CSSP+01] F. Cervera, L. Sanchis, J. V. Sánchez-Perez, R. Martínez-Sala, C. Rubio, F. Meseguer, C. Lopez, D. Caballero, and J. Sánchez-Dehesa. Refractive acoustic devices for airborne sound. *Phys. Rev. Lett.*, 88:023902, 2001.

[CY01] Y. Chen and Z. Ye. Acoustic attenuation by two-dimensional arrays of rigid cylinders. *Phys. Rev. Lett.*, 87:184301, 2001.

[DB70] M. E. Delany and E. N. Bazley. Acoustic properties of fibrous absorbent materials. *Appl. Acoustics*, 3:105–116, 1970.

[DDBL04] N. F. Declercq, J. Degrieck, R. Briers, and O. Leroy. Theory of the backward beam displacement on periodically corrugated surfaces and its relation to leaky Scholte-Stoneley waves. *J. Appl. Phys.*, 96:6869–6877, 2004.

[DDBL05] N. F. Declercq, J. Degrieck, R. Briers, and O. Leroy. Diffraction of homogeneous and inhomogeneous plane waves on a doubly corrugated liquid/solid interface. *Ultrasonics*, 43:605–618, 2005.

[Dow92] J. P. Dowling. Sonic band structure in fluids with periodicity density variations. *J. Acoust. Soc. Am.*, 91:2539–2543, 1992.

[DPL03] T. Dupont, G. Pavic, and B. Laulagnet. Acoustic properties of lightweight micro-perforated plate systems. *Acta Acustica United with Acustica*, 89:201–212, 2003.

[Duh06] D. Duhamel. Shape optimization of noise barriers using genetic algorithms. *J. Sound Vib.*, 297:432–443, 2006.

[EB03] I. Ekici and H. Bougdah. Review of research on environmental noise barriers. *Build. Acoust.*, 10:289–323, 2003.

[ECU+08] H. Estada, P. Candelas, A. Uris, F. Belmar, F. J. García de Abajo, and F. Meseguer. Extraordinary sound screening in perforated plates. *Phys. Rev. Lett.*, 101:084302, 2008.

[EdAC+09] H. Estrada, F. J. García de Abajo, P. Candelas, A. Uris, F. Belmar, and F. Meseguer. Angle-dependent ultrasonic transmission through plates with subwavelength hole arrays. *Phys. Rev. Lett.*, 102:144301, 2009.

[Emb96] T. F. W. Embleton. Tutorial on sound propagation outdoors. *J. Acoust. Soc. Am.*, 100:31–48, 1996.

[EN 94] EN 29053. *Acoustics. Materials for acoustics applications. Flow resistivity determination.* European Commitee for Standardization, Brussels, Belgium, 1994.

[EN 97] EN 1793. *Road traffic noise reduction devices. Test method for determining the acoustic performance - Part 2: Intrinsic characteristics of airborne sound insulation.* European Commitee for Standardization, Brussels, Belgium, 1997.

[Eur13] European Tyre Recycling Association. *Introduction to tyre recycling*, 2013.

[Eur14] European Environment Agency. *Noise in Europe*, 2014.

[FA14] R. Fleury and A. Alù. Cloaking and invisibility: A review. *Forum for Electromagnetic Research Method and Applications Technologies (FERMAT)*, 1:1–24, 2014.

[Fan41] U. Fano. The theory of anomalous diffraction gratings and of quasi-stationary waves on metallic surfaces (Sommerfeld's waves). *J. Opt. Soc. Am.*, 31:213–222, 1941.

[FEGM08] M. Farhat, S. Enoch, S. Guenneau, and A. B. Movchan. Broadband cylindrical acoustic cloak for linear surface waves in a fluid. *Phys. Rev. Lett.*, 101:134501, 2008.

[FGE09] M. Farhat, S. Guenneau, and S. Enoch. Broadband cylindrical acoustic cloak for linear surface waves in a fluid. *Phys. Rev. Lett.*, 103:024301, 2009.

[FXX+06] N. Fang, D. Xi, J. Xu, M. Ambati, W. Srituravanich, C. Sun, and X. Zhang. Ultrasonic metamaterials with negative modulus. *Nat. Mater.*, 5:452–456, 2006.

[FZ97a] H. Fuchs and X. Zha. Sound absorbing glass building component or transparent synthetic glass building component. US Patent 5700527, 1997.

[FZ97b] H. V. Fuchs and X. Zha. Acrylic-glass sound absorbers in the plenum of the deutscher bundestag. *Appl. Acoustics*, 51:211–217, 1997.

[GAÅ08] Y. Guo, S. Allam, and M. Åbom. Micro-perforated plates for vehicle applications. *37th International Congress and Exposition on Noise Control Engineering*, 2008.

[GAH11] M. D. Guild, A. Alù, and M. R. Haberman. Cancellation of acoustic scattering from an elastic sphere. *J. Acoust. Soc. Am.*, 129:1355–1365, 2011.

[GAH14] M. D. Guild, A. Alù, and M. R. Haberman. Cloaking of an acoustic sensor using scattering cancellation. *Appl. Phys. Lett.*, 105:023510, 2014.

[GCGST+12] V. M. García-Chocano, R. Graciá-Salgado, D. Torrent, F. Cervera, and J. Sánchez-Dehesa. Quasi-two-dimensional acoustic metamaterial with negative bulk modulus. *Phys. Rev. B*, 85:184102, 2012.

[GHA12] M. D. Guild, M. R. Haberman, and A. Alù. Plasmonic-type acoustic cloak made of a bilaminate shell. *Phys. Rev. B*, 86:104302, 2012.

[GMV+03] C. Goffaux, F. Maseri, J. O. Vasseur, B. Djafari-Rouhani, and P. Lambin. Measurements and calculations of the sound attenuation by a phononic band gap structure suitable for an insulating partition application. *Appl. Phys. Lett.*, 83:281–283, 2003.

[Gol89] D. E. Goldberg. *Genetic Algorithms in Search, Optimization and Machine Learning*. Addison Wesley, Boston, 1989.

[GSGCTSD13] R. Graciá-Salgado, V. M. García-Chocano, D. Torrent, and J. Sánchez-Dehesa. Negative mass density and density-near-zero quasi-two-dimensional metamaterials: Design and applications. *Phys. Rev. B*, 88:224305, 2013.

[GY03] B.C. Gupta and Z. Ye. Theoretical analysis of the focusing of acoustic waves by twodimensional sonic crystals. *Phys. Rev. E*, 67:036603, 2003.

[HCSD05] A. Håkansson, F. Cervera, and J. Sánchez-Dehesa. Sound focusing by flat acoustic lenses without negative refraction. *Appl. Phys. Lett.*, 86:054102, 2005.

[HCWH91] D. C. Hothersall, S. N. Chandler-Wilde, and M. N. Hajmirzae. Efficiency of single noise barriers. *J. Sound and Vib.*, 146:302–322, 1991.

[HCY+03] K. M. Ho, C. K. Cheng, Z. Yang, X. X. Zhang, and P. Sheng. Broadband locally resonant sonic chields. *Appl. Phys. Lett.*, 83:5566–5568, 2003.

[HGNB+08] J. M. Herrero, S. García-Nieto, X. Blasco, V. Romero-García, J. V. Sánchez-Pérez, and L. M. García-Raffi. Optimization of sonic crystal attenuation properties by ev-MOGA multi-objective evolutionary algorithm. *Struct Multidisc Optim.*, 39:203–215, 2008.

[HJPR85] D. A. Hutchins, H. W. Jones, B. Paterson, and L. T. Russel. Studies of parallel barrier performance by acoustical modeling. *J. Acoust. Soc. Am.*, 77:536–546, 1985.

[HM76] M. C. Hutley and D. Maystre. The total absorption of light by a diffraction grating. *Opt. Comm.*, 19:431–436, 1976.

[HO65] A. Hessel and A. A. Oliner. A new theory of Wood's anomalies on optical gratings. *Appl. Opt.*, 4:1275–1297, 1965.

[HSDC06] A. Håkansson, J. Sánchez-Dehesa, and F. Cervera. Experimental realization of sonic demultiplexing devices based on inverse designed scattering acoustic elements. *Appl. Phys. Lett.*, 88:163506, 2006.

[HSDS04] A. Håkansson, J. Sánchez-Dehesa, and L. Sanchis. Acoustic lens design by genetic algorithms. *Phys. Rev. B*, 70:214302, 2004.

[HSN+04] N. Horiuchi, Y. Segawa, T. Nozokido, K. Mizuno, and H. Miyazaki. Isotropic photonic gaps in a circular photonic crystal. *Opt. Lett.*, 29:1084–1086, 2004.

[Hur80] C. J. Hurst. Sound transmission between absorbing parallel planes. *J. Acoust. Soc. Am.*, 67:206–213, 1980.

[II67] U. Ingard and H. Ising. Acoustic nonlinearity of an orifice. *J. Acoust. Soc. Am.*, 42:6–17, 1967.

[Ing53] U. Ingard. On the theory and design of acoustic resonators. *J. Acoust. Soc. Am.*, 25:1037–1061, 1953.

[ISO96] ISO 9613. *Acoustics. Attenuation of sound during propagation outdoors - Part 2.* International Organisation for Standardisation, Geneva, Switzerland, 1996.

[ISO10] ISO 10140. *Acoustics. Laboratory measurement of sound insulation of building elements - Part 2: Measurement of airborne sound insulation.* International Organisation for Standardisation, Geneva, Switzerland, 2010.

[JAAR83] A. Jungman, L. Adler, J. D. Achenbach, and R. Roberts. Reflection from a boundary with periodic roughness: Theory and experiment. *J. Acoust. Soc. Am.*, 74:1025–1032, 1983.

[JAQ82] A. Jungman, L. Adler, and G. Quentin. Ultrasonic anomalies in the spectrum of acoustic waves diffracted by periodic interfaces. *J. Appl. Phys.*, 53:4673–4680, 1982.

[JKD87] D. L. Johnson, J. Koplik, and Dashen. Theory of dynamic permeability and tortuosity in fluid saturated porous media. *J. Fluid Mech.*, 176:379–402, 1987.

[KB05] J. Kang and M. W. Brocklesby. Feasibility of applying micro-perforated absorbers in acoustic window systems. *Appl. Acoustics*, 66:669–689, 2005.

[KCBL04] A. Khelif, A. Choujaa, S. Benchabane, and V. Laude. Guiding and filtering acoustic waves in a two-dimensional phononic crystal. *IEEE Ultrasonics Symposium*, pages 654–567, 2004.

[KF98] A. Karageorghis and G. Fairweather. The method of fundamental solutions for axisymmetric acoustic scattering and radiation problems. *J. Acoust. Soc. Am.*, 104:3212–3218, 1998.

[KIKK00] H. J. Kang, J. G. Ih, J. S. Kim, and H. S. Kim. Prediction of sound transmission loss through multilayered panels by using Gaussian distribution of directional incident energy. *J. Acoust. Soc. Am.*, 107:1413–1420, 2000.

[KIKK02] H. J. Kang, J. G. Ih, H. S. Kim, and J. S. Kim. An experimental investigation on the directional distribution of incident energy for the prediction of sound transmission loss. *Appl. Acoustics*, 63:283–294, 2002.

[Kir68] G. Kirchhoff. Ueber den einflufs der warmeleitung in einem gase auf die schallbewegung. *Ann. Phys. Chem.*, 134:177–193, 1968.

[KJ57] C. W. Kosten and J. H. Jansen. Acoustic properties of flexible and porous materials. *Acustica*, 7:372–378, 1957.

[KJV83] S. Kirkpatrick, C. D. Gelatt Jr., and M. P. Vecchi. Optimization by simulated annealing. *Science*, 220:671–680, 1983.

[Kur74] Ulrich J. Kurze. Noise reduction by barriers. *J. Acoust. Soc. Am.*, 55:504–518, 1974.

[Kus97] M. S. Kushwaha. Stop-bands for periodic metallic rods: Sculptures that can filter the noise. *Appl. Phys. Lett.*, 70:3218–3220, 1997.

[Kut09] H. Kuttruff. *Room acoustics*, section 2.5, pages 52–55. Spon Press, fifth edition, 2009.

[LC04] J. Li and C. T. Chan. Double-negative acoustic metamaterial. *Phys. Rev. E*, 70:055602, 2004.

[LCZC09] Y. Lai, H. Chen, Z. Q. Zhang, and C. T. Chan. Complementary media invisibility cloak that cloaks objects at a distance outside the cloaking shell. *Phys. Rev. Lett.*, 102:093901, 2009.

[Leo06] U. Leonhardt. Optical conformal mapping. *Science*, 312:1777–1780, 2006.

[LHHD95] P. Langlet, A. C. Hladky-Hennion, and J. N. Decarpigny. Analysis of the propagation of plane acoustic waves in passive periodic materials using the finite element method. *J. Acoust. Soc. Am.*, 98:2792–2800, 1995.

[LJM+09] R. Liu, C. Ji, J. J. Mock, J. Y. Chin, T. J. Cui, and D. R. Smith. Broadband ground-plane cloak. *Science*, 323:366–369, 2009.

[LP97] E. G. Loewen and E. Popov. *Diffraction gratings and applications*. Marcel Dekker, New York, USA, 1997.

[LP08] J. Li and J. B. Pendry. Hiding under the carpet: A new strategy for cloaking. *Phys. Rev. Lett.*, 101:203901, 2008.

[LT07] C. M. Linton and I. Thompson. Resonant effects in scattering by periodic arrays. *Wave Motion*, 44:165–175, 2007.

[LZM+00] Z. Liu, X. Zhang, Y. Mao, Y. Y. Zhu, Z. Yang, C. T. Chan, and P. Sheng. Locally resonant sonic materials. *Science*, 289:1734–1736, 2000.

[Maa75] D. Y. Maa. Theory and design of microperforated panel sound.absorbing constructions. *Scientia Sinica*, 18:55–71, 1975.

[Maa87] D. Y. Maa. Microperforated-panel wideband absorbers. *Noise Cont. Eng. J.*, 19:77–84, 1987.

[Maa98] D. Y. Maa. Potential of microperforated panel absorber. *J. Acoust. Soc. Am.*, 104:2861–2866, 1998.

[Maa00] D. Y. Maa. Theory of microslit absorbers. *Acta Acustica*, 25:481–485, 2000.

[Mel73] T. H. Melling. The acoustic impedance of perforates at medium and high sound pressure levels. *J. Sound Vib.*, 29:1–65, 1973.

[MFM+14] A. Maurel, S. Félix, J. F. Mercier, A. Ourir, and Z. E. Djeffal. Wood's anomalies for arrays of dielectric scatterers. *J. Europ. Soc. Rap. Public.*, 9:14001, 2014.

[MHDL12] R. P. Moiseyenko, S. Herbison, N. Declerq, and V. Laude. Phononic crystal diffraction gratings. *J. Appl. Phys.*, 111:034907, 2012.

[MI68] P. M. Morse and K. U Ingard. *Theoretical acoustics*. Mc Graw Hill, New York, 1968.

[MI01] T. Miyashita and C. Inoue. Numerical investigations of transmission and waveguide properties of sonic crystals by finite-difference time-domain method. *Jpn. J. Appl. Phys.*, 40:3488–3492, 2001.

[Mik90] Y. Miki. Acoustical properties of porous materials - modifications of delany-bazley laws. *J. Acoust. Soc. Jpn.*, 11:19–28, 1990.

[MN77] D. Maystre and M. Nevière. Sur une méthode d'étude théorique quantitative des anomalies de Wood des réseaux

de diffraction: application aux anomalies de plasmons. *J. Opt. (Paris)*, 8:165–174, 1977.

[MNL+89] K. Mampaert, P. B. Nagy, O. Leroy, L. Adler, A. Jungman, and G. Quentin. On the origin of the anomalies in the reflected ultrasonic spectra from periodic surfaces. *J. Acoust. Soc. Am.*, 86:429–431, 1989.

[MO80] D.N. May and N.M. Osman. Highway noise barriers: new shapes. *J. Sound Vib.*, 55:73–101, 1980.

[MO12] T. P. Martin and G. J. Orris. Hybrid intertial method for broadband scattering reduction. *Appl. Phys. Lett.*, 100:033506, 2012.

[MP76] D. Maystre and R. Petit. Brewster incidence for metallic gratings. *Opt. Comm.*, 17:196–200, 1976.

[MV04] H. M. Miedema and H. Vos. Noise annoyance from stationary sources: Relationships with exposure metric dayeveningnight level (denl) and their confidence intervals. *J. Acoust. Soc. Am.*, 116:334–343, 2004.

[NM65] J. A. Nelder and R. Mead. A simplex method for function minimization. *Computer Journal*, 7:308–313, 1965.

[Nor09] A. N. Norris. Acoustic metafluids. *J. Acoust. Soc. Am.*, 125:839–849, 2009.

[PCS06a] J. Pfretzschner, P. Cobo, and F. Simón. Insertion units which are microperforated for use as sound absorbers. Patent WO 2006/021605 A1, 2006.

[PCS+06b] J. Pfretzschner, P. Cobo, F. Simón, M. Cuesta, and A. Fernández. Microperforated insertion units: An alternative strategy to design microperforated panels. *Appl. Acoustics*, 67:62–73, 2006.

[PHRS99] J. B. Pendry, A. J. Holden, D. J. Robbins, and W. J. Stewart. Magnetism from conductors and enhanced nonlinear phenomena. *IEEE Trans. on Microwave Theory and Techniques*, 47:2075–2084, 1999.

[PL08] J. B. Pendry and J. Li. An acoustic metafluid: realizing a broadband acoustic cloak. *New J. of Phys.*, 10:115032, 2008.

[PPL+11] C. M. Park, J. J. Park, S. H. Lee, Y. M. Seo, C. K. Kim, and S. H. Lee. Amplification of acoustic evanescent waves using metamaterial slabs. *Phys. Rev. Lett.*, 107:194301, 2011.

[PR99] J. Pfretzschner and R. M. Rodríguez. Acoustic properties of rubber crumbs. *Polymer Testing*, 18:81–92, 1999.

[PSMC95] J. Pfretzschner, F. Simón, A. Moreno, and C. Colina. Sound absorbing wall with refuse vulcanised rubber, 1995. Patent application no.9502536.

[PSS06] J. B. Pendry, D. Schurig, and D. R. Smith. Controlling electromagnetic fields. *Science*, 312:1780–1782, 2006.

[PZC11] B. I. Popa, L. Zigoneanu, and S. A. Cummer. Experimental acoustic ground cloak in air. *Phys. Rev. Lett.*, 106:253901, 2011.

[RACH68] R. H. Ritchie, E. T. Arakawa, J. J. Cowan, and R. N. Hamm. Surface-plasmon resonance effect in grating diffraction. *Phys. Rev. Lett.*, 22:1530–1533, 1968.

[Ray07] J. W. Strutt Lord Rayleigh. Note on the remarkable case of diffraction spectra described by prof. Wood. *Proc. R. Soc. Lond.*, 79:399–416, 1907.

[Ray45] J. W. Strutt Lord Rayleigh. *Theory of sound*, chapter 19. Dover Publications, New York, second edition, 1945.

[RCSP+99] C. Rubio, D. Caballero, J. V. Sánchez-Perez, R. Martínez-Sala, J. Sánchez-Dehesa, F. Meseguer, and F. Cervera. The

existence of full gaps and deaf bands in two-dimensional sonic crystals. *J. Lightwave Tech.*, 17:2202–2207, 1999.

[RFA71] E. J. Rice, C. E. Feiler, and L. W. Acker. Acoustic aerodynamic performance of a 6-foot-diameter fan for turbofan engines. Technical report, NASA Technical Note D-6178, 1971.

[RGSPGR+08] V. Romero-García, J. V. Sánchez-Prez, L. M. García-Raffi, J. M. Herrero, S. García-Nieto, and X. Blasco. High optimization process for increasing the attenuation properties of acoustic metamaterials by means of the creation of defects. *Appl. Phys. Lett.*, 93:223502, 2008.

[RGSPGR+09] V. Romero-García, J. V. Sánchez-Pérez, L. M. García-Raffi, J. M. Herrero, S. García-Nieto, and X. Blasco. Hole distribution in phononic crystals: Design and optimization. *J. Acoust. Soc. Am.*, 125:3774–3783, 2009.

[Ric71] E. J. Rice. A model for the acoustic impedance of a perforated plate liner with multiple frequency excitation. Technical report, NASA Technical Memorandum X-67950, 1971.

[RKM+12] D. Rainwater, A. Kerkhoff, K. Melin, J. C. Soric, G. Moreno, and A. Alù. Experimental verification of three-dimensional plasmonic cloaking in free-space. *New J. of Phys.*, 14:013054, 2012.

[SB00] B. H. Song and J. S. Bolton. A transfer-matrix approach for estimating the characteristic impedance and wave numbers of limp and rigid porous materials. *J. Acoust. Soc. Am.*, 107:1131–1152, 2000.

[SC92] M. R. Stinson and Y. Champoux. Propagation of sound and the assignment of shape factors in model porous material having simple pore geometries. *J. Acoust. Soc. Am.*, 92:685–695, 1992.

[SCSD+01] L. Sanchis, F. Cervera, J. Sánchez-Dehesa, J. V. Sánchez-Pérez, C. Rubio, and R. Martínez-Sala. Reflectance properties of two-dimensional sonic band-gap crystals. *J. Acoust. Soc. Am.*, 109:2598–2605, 2001.

[SE96] M. M. Sigalas and E. N. Economou. Attenuation of multiple-scattered sound. *Europhys. Lett.*, 36:241–246, 1996.

[SG72] P. G. Smith and R. A. Greenkorn. Theory of acoustical wave propagation in porous media. *J. Acoust. Soc. Am.*, 52:247–253, 1972.

[SG00] M. M. Sigalas and N. García. Importance of coupling between longitudinal and transverse components for the creation of acoustic band gaps: The aluminum in mercury case. *Appl. Phys. Lett.*, 76:2307–2309, 2000.

[SHCSD03] L. Sanchis, A. Håkansson, F. Cervera, and J. Sánchez-Dehesa. Acoustic interferometers based on two-dimensional arrays of rigid cylinders in air. *Phys. Rev. B*, 67:035422, 2003.

[SHLZ+04] L. Sanchis, A. Håkansson, D. López-Zanón, J. Bravo-Abab, and J. Sánchez-Dehesa. Integrated optical devices design by genetic algorithm. *Appl. Phys. Lett.*, 84:4460–4462, 2004.

[Siv35] L. J. Sivian. Acoustic impedance of small orifices. *J. Acoust. Soc. Am.*, 7:94–101, 1935.

[SMJ+06] D. Schurig, J. J. Mock, B. J. Justice, S. A. Cummer, J. B. Pendry, A. F. Starr, and D. R. Smith. Metamaterial electromagnetic cloak at microwave frequencies. *Science*, 314:977–980, 2006.

[SMK06] K. Sakagami, M. Morimoto, and W. Koike. A numerical study of double-leaf microperforated panel absorbers. *Appl. Acoustics*, 67:609–619, 2006.

[SMY05] K. Sakagami, M. Morimoto, and M. Yairi. A note on the effect of vibration of a microperforated panel on its sound

absorption characteristics. *Acoust. Sci. Tech.*, 26:204–207, 2005.

[SPCMS+98] J. V. Sánchez-Pérez, D. Caballero, R. Martínez-Sala, C. Rubio, J. Sánchez-Dehesa, F. Meseguer, J. Llinares, and F. Galvez. Sound attenuation by a two-dimensional array of rigid cylinders. *Phys. Rev. Lett.*, 80:5325–5328, 1998.

[SPRMS+02] J. V. Sánchez-Perez, C. Rubio, R. Martínez-Sala, R. Sánchez-Grandia, and V. Gómez. Acoustic barriers based on periodic arrays of scatterers. *Appl. Phys. Lett.*, 81:5240–5242, 2002.

[SS85] M. R. Stinson and E. A. G. Shaw. Acoustic impedance of small, circular orifices in thin plates. *J. Acoust. Soc. Am.*, 77:2039–2042, 1985.

[SSRS86] A. F. Seybert, B. Soenarko, F. J. Rizzo, and D. J. Shippy. A special integral equation formulation for acoustic radiation and scattering for axisymmetric bodies and boundary conditions. *J. Acoust. Soc. Am.*, 80:1241–1247, 1986.

[Ste01] C. Steele. A critical review of some traffic noise prediction models. *Appl. Acoustics*, 62:271–287, 2001.

[SW11] C. M. Soukoulis and M. Wegener. Past achievements and future challenges in the development of three-dimensional photonic metamaterials. *Nature Photonics*, 5:523530, 2011.

[SWW12] N. Stenger, M. Wilhelm, and M. Wegener. Experiments on elastic cloaking in thin plates. *Phys. Rev. Lett.*, 108:014301, 2012.

[TdAB+08] T. V. Teperik, F. J. García de Abajo, A. G. Borisov, M. Abdelsalam, P. N. Bartlett, Y. Sugawara, and J. J. Baumberg. Omnidirectional absorption in nanostructured metal surfaces. *Nat. Photonics*, 2:299–301, 2008.

[THCSD06] D. Torrent, A. Håkansson, F. Cervera, and J. Sánchez-Dehesa. Homogenization of two-dimensional clusters of rigid rods in air. *Phys. Rev. Lett.*, 96:204302, 2006.

[TSD08a] D. Torrent and J. Sánchez-Dehesa. Acoustic cloaking in two dimensions: a feasible approach. *New J. of Phys.*, 10:063015, 2008.

[TSD08b] D. Torrent and J. Sánchez-Dehesa. Anisotropic mass density by two-dimensional acoustic metamaterials. *New J. of Phys.*, 10:023004, 2008.

[TT08] M. Toyoda and D. Takahashi. Sound transmission through a microperforated-panel structure with subdivided air cavities. *J. Acoust. Soc. Am.*, 124:3594–3603, 2008.

[UAL06] O. Umnova, K. Attenborough, and C. M. Linton. Effect of porous covering on sound attenuation by periodic arrays of cylinders. *J. Acoust. Soc. Am.*, 119:278–284, 2006.

[Wat96] G. R. Watts. Acoustic performance of parallel traffic noise barriers. *Appl. Acoustics*, 47:95–119, 1996.

[WE85] G. S. K. Wong and T. F. W. Embleton. Variation of the speed of sound in air with humidity and temperature. *J. Acoust. Soc. Am.*, 77:1710–1712, 1985.

[WM93] S. S. Wang and R. Magnusson. Theory and applications of guided-mode resonance filters. *Appl. Opt.*, 32:2606–2613, 1993.

[Woo02] R. W. Wood. On a remarkable case of uneven distribution of light in a diffraction grating spectrum. *Philos. Mag.*, 4:396–402, 1902.

[Wor09] World Health Organization. *Night noise guidelines for Europe*, 2009.

[Wor11] World Health Organization. *Burden of disease from environmental noise*, 2011.

[ZK49] C. Zwikker and C. W. Kosten. *Sound absorbing material*. Elsevier, Amsterdan, 1949.

[ZLK+11] X. Zhu, B. Liang, W. Kan, X. Zou, and J. Cheng. Acoustic cloaking by a superlens with single negative materials. *Phys. Rev. Lett.*, 106:014301, 2011.

[ZPC14] L. Zigoneanu, B. I. Popa, and S. A. Cummer. Three-dimensional broadband omnidirectional acoustic ground cloak. *Nat. Mat.*, 13:352–355, 2014.

[ZXF11] S. Zhang, C. Xia, and N. Fang. Broadband acoustic cloak for ultrasound waves. *Phys. Rev. Lett.*, 106:024301, 2011.